Transport, Stirring and Mixing in Two-Dimensional Vortex Flows

Thesis by
Inki A. Min

In Partial Fulfillment of the Requirements
for the Degree of
Doctor of Philosophy

California Institute of Technology
Pasadena, California

1995
(Submitted 27 October 1994)

Acknowledgments

I thank my advisor, Professor Anthony Leonard, for his guidance and support in developing this thesis. He patiently saw me through every phase with an open and encouraging style that made the process exciting and enjoyable. I also thank the members of my committee, Professors P. Dimotakis, D. Pullin, A. Roshko and S. Wiggins for their suggestions and criticisms which resulted in numerous improvements to the thesis. Professor Dimotakis especially provided many ideas that were incorporated into this thesis.

I would also like to acknowledge contributions by Darin Beigie and Igor Mezić. Darin explained many aspects of his work and sparked ideas for my own research. The work in Chapter two was developed with Igor, with whom I have enjoyed many hours of beneficial discussions. These interactions as well as with other fellow students have been an important part of my graduate experience.

I thank The Aerospace Corporation for their generous support in the form of the Corporate Fellowship and the Advanced Study Grant. On a more personal level, I have been lucky enough to have Tom Trafton and David Kim as mentors and friends who have enthusiastically encouraged my academic endeavors.

I would like to express my appreciation to my wife Ke Sook for her love, support and understanding during my studies. She was a constant friend and a cheerful study partner. And lastly, this thesis is dedicated to my parents for always putting my future ahead of their present concerns.

Abstract

To understand the basic contribution of vortex motion in the transport and mixing of passive fluid, we study a system of N discrete vortices. With variation of N and δ (a vorticity distribution parameter), we are able to experiment with a range of vortex dynamics sufficient to capture many of the features of two-dimensional turbulence in their elementary form - such as vortex merging (inverse cascade of energy), filamentation (enstrophy cascade), etc. With this model the mixing of the fluid is numerically studied via stretch statistics and the spatial distribution of a non-diffusive scalar interface. The spectrum of spatial distribution of scalars as a result of the stirring motion of the N vortices is particularly important in view of the recent (as well as historical) interest in the characterization of the scalar distribution in turbulence. We also examine the velocity field statistics and the Lagrangian motion of fluid particles. It is also instructive to look at the kinematic causes behind the types of statistics that are obtained for the velocity structure functions. A 'building block' approach to understanding these effects in turbulence may lie in building up from a collection of discrete vortices, as done in this thesis, to adding vortices of different scales and the three-dimensional effects. It is in the context of these wider issues that we study the N-vortex problem.

In the final part of this thesis we investigate the two-dimensional mixing produced by large scale vortical structures during the evolution of a spatially developing

mixing layer. Although the advent of three-dimensionality and fully developed turbulence are essential features of mixing layers, it is still dominated by the large scale two-dimensional structures and its effect on the mixing is illustrated here.

Contents

List of Figures

Chapter 1

Introduction

1.1 General introduction and motivation

The central theme of this thesis is the role played by vorticity in the stirring and mixing of a passive scalar in an incompressible fluid. Because of its complexity turbulent flow is often assumed to be homogeneous, isotropic and random. Although this helps greatly in analyzing the problem, it is not always a good representation of the physical problem at hand. Our approach consists of treating vorticity as the primary dynamic agent. By varying the vorticity distribution, we believe that we can simulate the different regimes of laminar and turbulent flows. We emphasize the common mechanism of vortex-stirring, whether this occurs in the Stokes flow regime or in the infinite Reynolds number limit of Euler flows. When the stirring problem is viewed with this in mind, spatial distribution of scalars can look similar for vastly different flow regimes when examined at the proper scales (see for example Dahm et al. [29], Brachet et al. [18], Dimotakis et al. [32], and Ottino [92] where the pictures of isoscalar lines in experimental turbulent jets, isovorticity lines in numerical simulations of two-dimensional turbulence, and scalar distributions in

two-dimensional, non-turbulent, chaotic flows show distinct similarities).

The physical flows that motivate our concern for the fluid mixing and vortex motion are turbulent shear layers and planetary atmospheric flows that are dominated by large scale two-dimensional vortices. We use the N-vortex system in two-dimensions, as well as the vortex sheet model and a new kinematic map to study the issues of transport, stirring and mixing.

Recent numerical studies by McWilliams [78] and Babiano et al. [10, 1] have shown the similarity between the coherent structures occurring in two-dimensional turbulence and the discrete vortex models. These coherent structures appear to be a consequence of the energy cascade in two-dimensions in which the vorticity tends towards the larger scales through mergings, and can be modeled by a single vortex blob. This type of evidence is important for showing the relevance and validity of representing two-dimensional turbulence through the interaction of discrete vortices. Maximum entropy analyses of two-dimensional vortex systems (see [105] for example) have also resulted in vorticity distributions similar to the vortex blobs to be discussed in the next section.

1.2 Equations of motion, vortex configurations

1.2.1 Equations of motion

The role of vorticity in shaping the flow is clear from the vorticity form of the Navier-Stokes equation. For two-dimensional, inviscid flow, this equation for the dynamics of vorticity appears especially simple, viz,

$$\frac{D\omega}{Dt} = \frac{\partial \omega}{\partial t} + \mathbf{u} \cdot \nabla \omega = 0 \tag{1.1}$$

The solution to this equation is of course, not so easily available for arbitrary vorticity distributions. The same is true for determining the motion of passive fluid particles

$$\frac{D\mathbf{x}}{Dt} = \mathbf{u}(\mathbf{x}, t). \tag{1.2}$$

Vortex method of flow computation involves keeping track of the vorticity ω (see [68] or [69] for the more general three-dimensional case). The calculation of velocity is done by the Biot-Savart law, which for two-dimensions is

$$\mathbf{u}(\mathbf{x}, t) = \frac{d\mathbf{x}}{dt}(\mathbf{x}, t) = -\frac{1}{2\pi}\int \frac{(\mathbf{x} - \mathbf{x}') \times \omega(\mathbf{x}', t)}{|\mathbf{x} - \mathbf{x}'|^2} d\mathbf{x}' + \nabla\phi. \tag{1.3}$$

This is the solution to the Poisson equation describing the relationship between the velocity $\mathbf{u}$ and the vorticity ω

$$\nabla^2\mathbf{u} = -\nabla \times \omega. \tag{1.4}$$

The boundary conditions for our problem (infinite with no solid boundaries and no flow at infinity) dictates that $\nabla\phi = 0$. In two dimensions the vorticity is $\omega = \omega\hat{\mathbf{e}}_z$ and for the point vortex case the scalar field ω is represented by

$$\omega(\mathbf{x}, t) = \sum_{i=1}^{N} \Gamma_i \delta[\mathbf{x} - \mathbf{x}_i(t)] \tag{1.5}$$

where δ is the Dirac delta function, and Γ_i is the strength of the ith vortex. This gives a system of $2N$ nonlinear ODEs for the positions of the N vortices:

$$\frac{d\mathbf{x}_i}{dt} = -\frac{1}{2\pi} \sum_{j=1, j\neq i}^{N} \frac{\Gamma_j(\mathbf{x}_i - \mathbf{x}_j) \times \hat{\mathbf{e}}_z}{|\mathbf{x}_i - \mathbf{x}_j|^2}. \tag{1.6}$$

Because of the singularity at the core of the vortices, vortex blob methods are often used to simulate vortical flows. There are several ways to de-singularize the vorticity [68], but we use the simple algebraic core method with the parameter δ.

The vorticity distribution is now given by

$$\omega(\mathbf{x},t) = \frac{1}{\pi}\sum_{i=1}^{N} \frac{\Gamma_i \delta^2}{\left(\delta^2 + |\mathbf{x}-\mathbf{x}_i|^2\right)^2} \tag{1.7}$$

and the velocity of each vortex blob evaluated at the center is

$$\frac{d\mathbf{x}_i}{dt} = -\frac{1}{2\pi}\sum_{j=1, j\neq i}^{N} \frac{\Gamma_j(\mathbf{x}_i-\mathbf{x}_j)\times\hat{\mathbf{e}}_z}{|\mathbf{x}_i-\mathbf{x}_j|^2+\delta^2}. \tag{1.8}$$

For passive fluid particle motion we must integrate

$$\frac{d\mathbf{x}}{dt} = -\frac{1}{2\pi}\sum_{i=1}^{N} \frac{\Gamma_j(\mathbf{x}-\mathbf{x}_i)\times\hat{\mathbf{e}}_z}{|\mathbf{x}-\mathbf{x}_i|^2+\delta^2} \tag{1.9}$$

also for each particle. The parameter δ can then be conveniently used to vary the vorticity distribution from isolated point vortices ($\delta = 0$) to vortices having significant overlap ($\delta =$ large). Along with the parameter N, this allows us to explore the consequences of different vorticity distributions in terms of the velocity statistics and transport of scalars. Figures 1.1,1.2, 1.3,and 1.4 illustrates the different types of vorticity distribution that can be achieved with the parameters δ and N.

There are four known invariants for the vortex system [68],

$$x\text{-linear impulse} \quad I_x = \sum_{i=1}^{N} \Gamma_i x_i = \text{const.}, \tag{1.10}$$

$$y\text{-linear impulse} \quad I_y = \sum_{i=1}^{N} \Gamma_i y_i = \text{const.}, \tag{1.11}$$

$$\text{angular impulse} \quad I_{r^2} = L^2 = \sum_{i=1}^{N} \Gamma_i r_i^2 = \text{const.}, \tag{1.12}$$

and

$$\text{energy} \quad I_E = H = -\frac{1}{4\pi}\sum_{i\neq j}^{N}\sum_{j\neq i}^{N} \Gamma_i\Gamma_j \log|\mathbf{r}_i-\mathbf{r}_j| = \text{const.} \tag{1.13}$$

Solutions of the vortex motion must observe the invariance of these quantities.

In chapters 2, 3, and 4 of this thesis, we use the discrete vortex system described here to study the effects on the transport of passive fluid particles.

1.2.2 Hamiltonian vortex mechanics

It is sometimes instructive to view the discrete vortex system in two-dimensions as an N-degree-of-freedom Hamiltonian system. This allows one the use of existing tools and theorems of dynamical systems to gain additional insights into the problem. See Aref [2, 6, 4] for detailed exposition on this topic and Wiggins [116, 115] or Lichtenberg and Lieberman [74] for a broader background on dynamical systems. The interaction energy H serves as the Hamiltonian function, with the conjugate variables $\Gamma_i x_i$ and y_i.

$$H(x,y) = -\frac{1}{4\pi} \sum_{i \neq j}^{N} \sum_{j \neq i}^{N} \Gamma_i \Gamma_j \log \left[(x_i - x_j)^2 + (y_i - y_j)^2 \right] \tag{1.14}$$

$$\Gamma_i \dot{x}_i = -\frac{\partial H}{\partial y_i} \tag{1.15}$$

$$\Gamma_i \dot{y}_i = \frac{\partial H}{\partial x_i}. \tag{1.16}$$

The invariants of Eq. (1.10 - 1.13) serve as the integrals of motion, however, they are not in involution with each other (meaning their Poisson bracket with each other are not all zero $[I_x, I_y] \neq 0, [I_{r^2}, I_x] \neq 0, [I_{r^2}, I_y] \neq 0$). There are in fact only *three* quantities, H, I_{r^2}, and $I_x^2 + I_y^2$ that are in involution with each other ($[H, I_x^2 + I_y^2] = 0, [H, I_{r^2}] = 0, [I_{r^2}, I_x^2 + I_y^2] = 0$). Thus the vortex motion (Eq. (1.15,1.16) or Eq. (1.6)) for $N \leq 3$ is integrable. A vortex system with $N > 3$ can be non-integrable, or chaotic (although special initial positions and/or circulation values involving symmetry may produce an integrable system) [2, 6, 87]. As the

number of vortices N, increases, it becomes more difficult to make any statement about the ensuing dynamics, but it may be possible, in reverse, to add to the understanding of the behavior of large degree-of-freedom Hamiltonian systems by the numerical simulations we perform. An example might be a study of the statistical behavior of the fluctuations as N is varied. Another option for large N is to make use of the statistical mechanics approach of Lundgren and Pointin [75] as discussed in the next section.

The motion of a passive particle can always be viewed as the 'reduced' problem, where the particle can be represented by a vortex with vanishing circulation. The trajectory of a passive particle in an N-vortex system then can be chaotic for $N > 2$. A somewhat different point of view for the passive particle trajectory is to regard the streamfunction $\psi(x, y, t)$ as the Hamiltonian, so that the fate of the passive fluid is the subject of the dynamics of a one-degree-of-freedom system. In all but the simplest cases, however, the time dependence due to the motion of the vortices will be intractable and the benefits of this formulation are not so easily reaped. Perhaps notable exceptions are the recent studies of oscillating vortex pairs by Rom-Kedar et al. [102] and Beigie et al. [13], where a rich understanding of the fluid transport is obtained through the use of invariant manifolds, horseshoes, chaotic tangles, and KAM (Kolmogorov-Arnold-Moser) theorem. Beigie's [12] development of a technique for analyzing quasi-periodic and aperiodic flows represents a significant advancement in terms of making use of the Hamiltonian formalism for fluid flows.

1.2.3 Vortex configurations

For the most part, the N-vortex studies of Chapters 2, 3, and 4 are limited to vortices of the same sign and circulation Γ. The initial configurations are chosen such that they match the equilibrium state for the vortices as derived by Lundgren and Pointin [75]. The purpose of this is to obtain long term statistics (vortices of

different signs tend to pair up and move away).

Although we roughly sketch Lundgren and Pointin's [75] equilibrium statistics analysis of two-dimensional vortices below, it is recommended that the original article [75] and other related papers by Montgomery and Joyce [82] or Kraichnan and Montgomery [65] for example be consulted. The reduced probability density function $p_1(\mathbf{r}_1)$ can be defined through the expression

$$p_1(\mathbf{r}_1)d\mathbf{r}_1 = Prob.\{\mathbf{r}_1 \in d\mathbf{r}_1\} \tag{1.17}$$

and

$$\int p_1(\mathbf{r}_1)d\mathbf{r}_1 = 1 \tag{1.18}$$

where $\mathbf{r}_1$ is the position of a single vortex. It follows naturally then, that the average vorticity, is given by

$$\langle\omega(\mathbf{r})\rangle = \Gamma \;\; p_1(\mathbf{r}) \; . \tag{1.19}$$

An equilibrium configuration based on a closure approximation for the one point distribution is then proposed, which produces an integral equation for $p_1(\mathbf{r}_1)$ that has the following Gaussian distribution as a solution for the parameter choice $\lambda = 0$, (where λ is proportional to the inverse temperature, related to the energy H of the system)

$$p_1(\mathbf{r}) = \frac{1}{\pi L^2} e^{-((\mathbf{r}-I_x\hat{\mathbf{e}}_x-I_y\hat{\mathbf{e}}_y)/L)^2}. \tag{1.20}$$

Since we will be dealing mostly with vortex distributions that are symmetric about the origin (in the mean), we will represent the one point distribution $p_1(\mathbf{r}_1)$ by $p_1(r)$.

The initial vortex positions chosen for the numerical simulations are such that the invariants of motion are specified as follows (see Eq. (1.10 - 1.13)):

$$I_x = 0 \tag{1.21}$$

$$I_y = 0 \tag{1.22}$$

$$I_{r^2} = L^2 = 1 \tag{1.23}$$

$$I_E = H = -.00461. \tag{1.24}$$

This choice of the value for H (energy) corresponds to Lundgren and Pointin's [75] $\lambda = 0$ state with $p_1(r)$ given by e^{-r^2}/π. Since there are an infinite number of possible configurations for a fixed H, we randomly generate large numbers of initial configurations and pick one that is sufficiently close to the desired H. The H values for the system can be 'tweaked' by moving adjacent vortices closer to or farther away from each other (since the interaction energy is a function of the inter-vortex distances).

The two conditions, $I_{r^2} = L^2 = 1$ and $\Gamma = \sum_{i=1}^{N} \Gamma_i = 1$ together set the length scale and the time scale for the N-vortex system ($[I_{r^2}] = l^4/t$ and $[\Gamma] = l^2/t$). All the other parameters $\delta, x, y, t, u, v, , \omega, H, \lambda$ are scaled with respect to the parameters $I_{r^2} = 1$ and $\Gamma = 1$.

In Chapter 5 we investigate stirring and mixing in a flow that is closer to an experimental one; namely the mixing layer, and so we will delay a description of the equations of motion for this flow until then.

1.3 Numerical method

The computations are performed using a fourth order Runge-Kutta integration scheme for the Lagrangian motion of the vortices and passive fluid particles. The time steps (Δt) are chosen such that the change in the invariant H (Eq.(1.13) is maintained to within 1% of the initial value. The other invariants (Eq.(1.10-1.12)) are satisfied to much higher levels of accuracy. While there have been numerical techniques developed (symplectic integrators, see [98] for example) specifically to take advantage of the Hamiltonian structure of systems such as ours, they were deemed computationally economic only for cases where extremely stringent require-

ments on the invariance of H were necessary.

1.3.1 Accuracy

Because of the chaotic nature of the vortex motion, error propagation during numerical computation is inevitable. This is a clear manifestation of the 'sensitive dependence on initial conditions', and there is no way around it. It is of course, helpful to maintain the known invariants of motion for vortex systems (see Eq. (1.10 - 1.13)). In the following we take the position that while the exact position of the vortices or passive fluid particles cannot be known, the overall properties remain the same and correct in the statistical sense.

The propagation of errors is best illustrated by the irreversibility of the computations. In Figure 1.5 we show the difference in position ($|\mathbf{x}_{forward}(t) - \mathbf{x}_{backward}(t)|$) between a particle integrated from $t = 0$ to $t = 200$ and a particle which is integrated back from the position at $t = 200$ to $t = 0$. (This is done for both passive particles and vortex particles.) The rate of error growth varies depending on the parameters N, δ, and dt, but the error growth is always large after a sufficient time span. Because the error is introduced from the limited number of digits used in the computer's memory, long time simulations will require an extraordinary amount of precision to maintain absolute fidelity.

1.3.2 Passive fluid tracking

For tracking of passive fluid particle trajectories, Lagrangian schemes have an inherent advantage in that the velocity at any point in the domain can be evaluated without having to interpolate from grid positions. A problem encountered in passive fluid tracking is that unlike the vortices, there are no invariants of motion that we can use to check the accuracy of the computation. This is especially important in

the motion around a vortex, since too large a time step can make the particle appear to "diffuse" out even when there is little or no radial velocity component. We treat this problem by checking that the distance travelled by a particle for each time step does not exceed some maximum value.

1.3.3 Line tracking

Line tracking is done similar to the particle tracking, except that particles are inserted to maintain a minimum distance between neighboring points. The stretching of lines are also measured from the distances between adjacent points on the line. The maximum distance maintained before insertion of new points is empirically determined depending on the run, but it was usually around a non-dimensional length value of .03.

1.4 Transport, stirring and mixing

Transport, stirring and mixing of fluid in chaotic flows have been a subject of focus in recent years [3, 92, 93, 71, 12, 102, 116]. In this thesis we address the transport and mixing associated with the dynamics of N vortices. We believe the study of the N-vortex system introduces the next level of complexity to the two-vortex systems mentioned in section 1.2.2. The long-term agenda of achieving a better understanding of the mixing mechanism involved in turbulent flows is implicit in this. Aref et al. [5] visually compared the scalar stirred by N vortices with the image produced from an experimental jet and commented on the similarity of the geometrical outline. Although the similarity may be purely superficial, we pursue this line of thought further — by measuring other aspects of the scalar transport, such as the line stretching, scalar spectra, and velocity statistics, he idea being that dissimilar flows share at the core a basic stirring mechanism. There are many

important issues such as diffusion and three-dimensionality that are not addressed in this thesis, but we consider this work to be a reasonable starting point for future investigations.

Mixing can be introduced by referring to it as the general notion of how different parts of the fluid become distributed. As simple as this sounds, there are some points that need to be clarified due to the many existing uses of the word mixing. Aref [7, 6] presents a detailed analysis of this problem, and we discuss some main points here. In fluid mechanics, *mixing* often refers only to molecular mixing that occurs through diffusion, and non-diffusive transport is termed *stirring*. In the study of the transport of scalars in non-diffusive systems, it is often the case that stirring of particles is reached to as small a scale as desired, essentially achieving mixing. This idea is expressed in the field of dynamical systems, where mixing is rigorously defined in the non-diffusive, stirring sense. It basically requires that a good "sharing" of the space down to the smallest scales is present as $t \to \infty$. Although the proper definition is a bit problematic in its use of the infinite time concept, it is this aspect of the scalar transport that we concentrate on in this thesis. Furthermore, in terms of the mixing properties and mechanisms (such as the stretching and folding), what we see in our N-vortex systems is similar to that observed in simple dynamical system models such as the Baker's map (see Chapters 3 and 5).

In Chapter 2 the velocity statistics associated with a vortex system is analyzed. We place a special emphasis on the role of the spatial distribution of the vorticity, and how it affects the statistics. The transport of passive particles is of course closely tied to these velocity statistics, and we examine these issues as well.

In Chapter 3 we deal with stretching, which is indirectly related to, but is crucial for mixing. This is done by examining the stretch statistics in a fluid that is stirred by N vortices. The spatial distribution of interfacial lines as they are stirred by the vortices, an important aspect of mixing, is studied in Chapter 4. Finally, in Chapter 5, we quantify the amount of mixing (including diffusion) that can be produced

in two-dimensional models of the shear layer. Although one could question the usefulness of studying a purely two-dimensional flow, its value lies precisely in the fact that numerical simulations can separate out the two and three dimensional effects — something that cannot be done in experiments. We also emphasize the elucidation of the mixing mechanism which appears to be ubiquitous in vortical flows; namely the rollup and pairing of vortical structures.

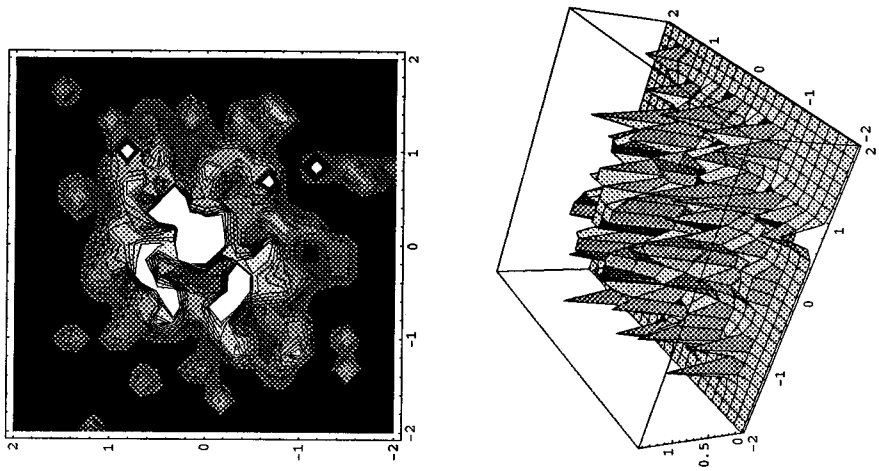

Figure 1.1: Vorticity distribution $\omega(x, y)$ for parameters $N = 150, \delta = .1$

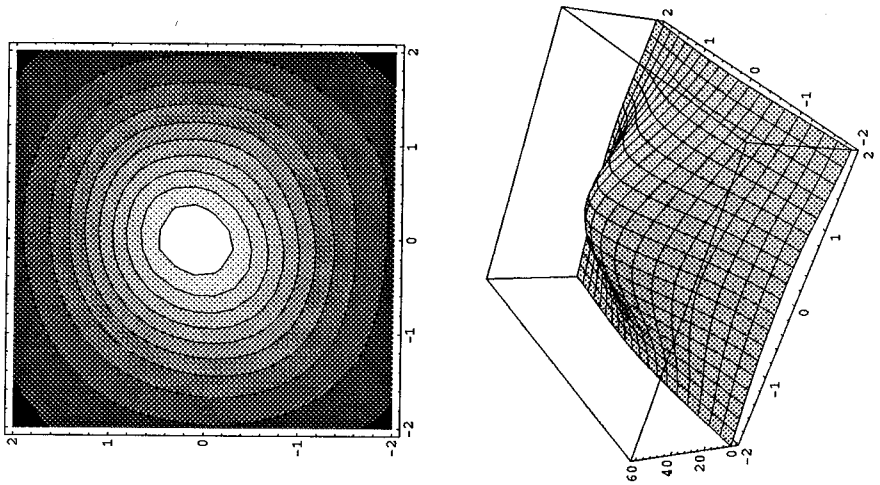

Figure 1.2: Vorticity distribution $\omega(x, y)$ for parameters $N = 150, \delta = 1.0$

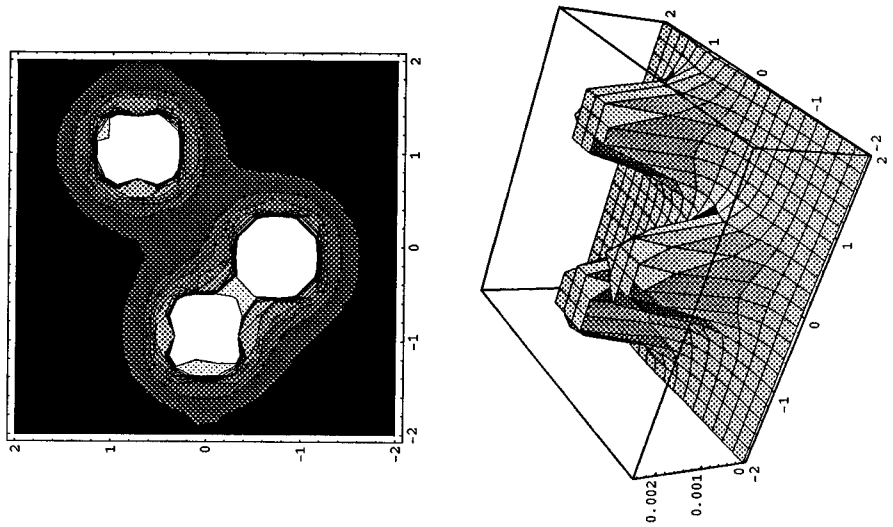

Figure 1.3: Vorticity distribution $\omega(x, y)$ for parameters $N = 3, \delta = .1$

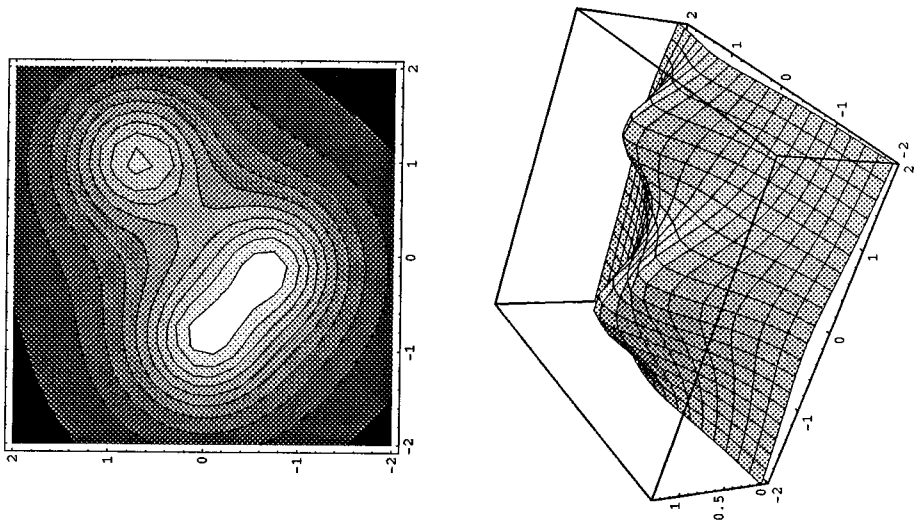

Figure 1.4: Vorticity distribution $\omega(x, y)$ for parameters $N = 3, \delta = 1.0$

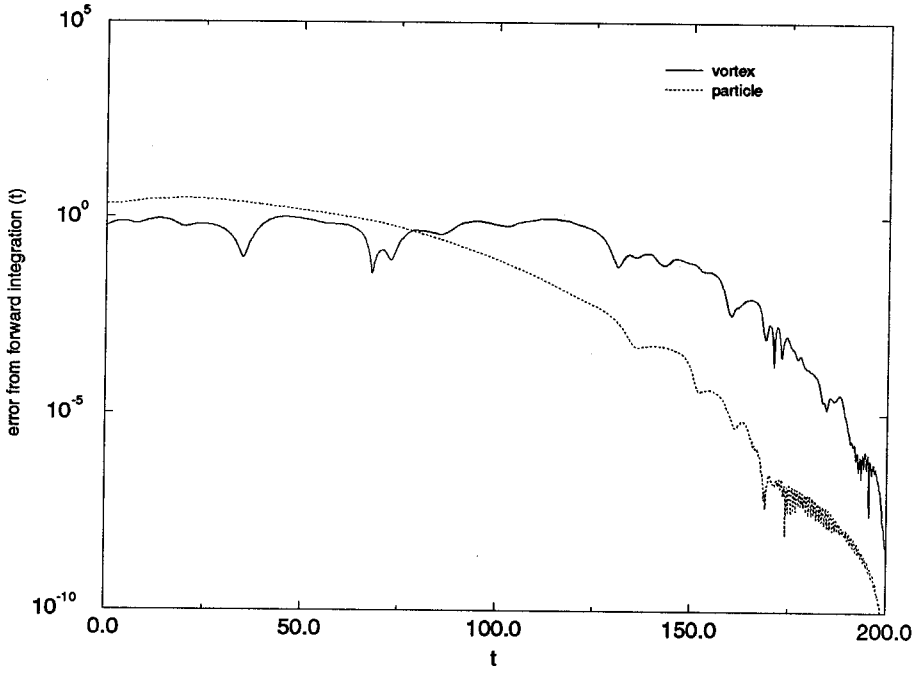

Figure 1.5: Error growth in vortex computations via comparison of $|\mathbf{x}_{forward}(t) - \mathbf{x}_{backward}(t)|$ vs. time

Chapter 2

Velocity Field Statistics of the N-vortex Problem

The work in this chapter was developed with Igor Mezić.

2.1 Introduction

One way to characterize a turbulent flow is through its velocity probability density function (PDF) $p(u;\mathbf{r})$. Normal or Gaussian statistics are usually considered to be an indicator of randomness of the flow, but it is an assumption that is often made *a priori*. Turbulence is often synonymous with random, homogeneous flows, but we believe it to be too narrow a focus. A good example is the planar mixing layer in which the large scale, mostly two-dimensional structures that are clearly not of a uniform distribution, dominate the flow. In this chapter we study the velocity statistics associated with a discrete, deterministic vortex system, and show how different statistics arise for different spatial arrangements of the vorticity.

In view of the increasing use of *vortex methods* [68, 69] of flow computation where

discrete, Lagrangian vortex elements are used to simulate turbulent flows, we hope to provide an understanding of the range of validity of these models for gathering statistics.

We have found an earlier work by Takayasu [108] who had taken a similar approach to the problem. We will discuss the similarities and disagreements with those results.

In section 2.2, a key idea in our analysis — that of the decomposition of the velocity field into the contributions of each of the N vortices, is described. The construction of the probability density functions (PDFs) for the velocity at a fixed location $\mathbf{r}$ due to a *single* vortex, $p_i(u_i;\mathbf{r})$ is then presented. The PDF associated with the velocity due to *all* the vortices, $p(u;\mathbf{r})$ follows from the use of limit distribution theorems. The same construction is used to analyze three-dimensional as well as velocity difference $p_\delta(\delta u(\mathbf{r};d\mathbf{r}))$ (structure function) statistics. In section 2.5, the numerical simulations with N-vortices are described, and the results are compared with the analytical predictions. The different statistical properties observed for various parameter values are discussed. A brief section on the Lagrangian statistics is then presented, and we close with a discussion of the implications for physically relevant flow problems.

2.2 The probability density of the velocity field

Consider the following decomposition of the two-dimensional point vortex velocity field:

$$u(\mathbf{r}) = -\frac{1}{2\pi}\sum_{i=1}^{N}\frac{\Gamma_i(y-y_i)}{|\mathbf{r}-\mathbf{r}_i|^2} = \sum_{i=1}^{N} u_i(\mathbf{r}) \tag{2.1}$$

$$v(\mathbf{r}) = \frac{1}{2\pi}\sum_{i=1}^{N}\frac{\Gamma_i(x-x_i)}{|\mathbf{r}-\mathbf{r}_i|^2} = \sum_{i=1}^{N} v_i(\mathbf{r}) \tag{2.2}$$

where the $\mathbf{r}_i$ are the vortex positions and $u_i(\mathbf{r})$ is that portion of the x component of velocity induced by the ith vortex:

$$u_i(\mathbf{r}) \equiv \frac{-\Gamma_i}{2\pi}\frac{(y-y_i)}{|\mathbf{r}-\mathbf{r}_i|^2} = -\frac{\Gamma i}{2\pi}\frac{\sin\theta_i}{\rho_i} \tag{2.3}$$

$$\rho_i \equiv |\mathbf{r}-\mathbf{r}_i| \tag{2.4}$$

$$\theta_i \equiv \tan^{-1}\left(\frac{y-y_i}{x-x_i}\right), \tag{2.5}$$

and similarly, the y component induced by vortex i is

$$v_i(\mathbf{r}) \equiv \frac{\Gamma i}{2\pi}\frac{(x-x_i)}{|\mathbf{r}-\mathbf{r}_i|^2} = \frac{\Gamma i}{2\pi}\frac{\cos\theta_i}{\rho_i}\ . \tag{2.6}$$

2.2.1 Probability density of velocity due to a single vortex

We will confine our analysis to the x-component of the velocity; the y-component results follow trivially. Let us define $p_i(u_i;\mathbf{r}|p_1(\mathbf{r}))$ as probability density of the x-component of the velocity due to a single vortex, measured at $\mathbf{r}$, i.e.,

$$p_i(u_i;\mathbf{r}|p_1(\mathbf{r})) = \lim_{\Delta u_i \to 0} \frac{Prob.\left\{u_i - \frac{\Delta u_i}{2} < u_i' < u_i + \frac{\Delta u_i}{2}\right\}}{\Delta u_i}. \tag{2.7}$$

This expresses the distribution of the velocity at $\mathbf{r}$ as the ith vortex moves about in its trajectory, and thus implies an average over the vortex location given by $p_1(r)$ (see section 1.2.3 of chapter 1); however, we are interested only in the high u_i tails of $p_i(u_i;\mathbf{r}|p_1(\mathbf{r}))$, for which we assume a locally uniform density of the vorticity. Therefore, for notational convenience we will henceforth denote $p_i(u_i;\mathbf{r}|p_1(\mathbf{r}))$ by $p_i(u_i;\mathbf{r})$. The probability density associated with the velocity due to *all* N vortices at $\mathbf{r}$ is denoted $p(u;\mathbf{r})$.

Now consider lines of constant $u_i = U$ near $\mathbf{r}$. (We drop the subscript with the understanding that we are dealing with the velocity contribution of a single vortex.)

Then these iso-U lines are given by

$$U \sim \frac{\sin\theta}{\rho} = \text{constant}. \tag{2.8}$$

It is clear that U is a monotonic function of ρ and that constant U lines close upon each other (see Figure 2.1). The probability of the vortex inducing a velocity greater than U is proportional to the area enclosed by the constant U curve i.e., $\mathcal{A} \sim P(u > U; \mathbf{r})$.

$$d\mathcal{A} = \rho^2 \cos\theta d\theta \tag{2.9}$$

and from Eq.(2.8)

$$d\theta = \frac{U}{\cos\theta}\ d\rho \tag{2.10}$$

and

$$\mathcal{A} = \int d\mathcal{A} = 2U \int_0^{1/U} \rho^2 d\rho \tag{2.11}$$

$$= \frac{2}{3}U^{-2} \tag{2.12}$$

$$\sim P(u > U; \mathbf{r}). \tag{2.13}$$

And since

$$P(u > U; \mathbf{r}) \sim \int_U^\infty p_i(u_i) du_i \tag{2.14}$$

it follows that

$$p_i(u_i; \mathbf{r}) \sim u_i^{-3} \quad \text{for large positive } u_i. \tag{2.15}$$

Similarly, for large, negative u_i

$$P(u < U; \mathbf{r}) \sim \int_{-\infty}^U p_i(u_i) du_i \tag{2.16}$$

and

$$p_i(u_i; \mathbf{r}) \sim -u_i^{-3}. \tag{2.17}$$

Since the probability distribution of the vortices is not necessarily uniform, this will

hold for sufficiently small regions around $\mathbf{r}$, which then correspond to the high u tail of the velocity distribution.

For the non-singular case, the velocity induced at $\mathbf{r}$ by a vortex at a distance $\rho = |\mathbf{r} - \mathbf{r}_i|$ is

$$u_i(r) = -\frac{\Gamma_i \rho \sin\theta}{2\pi(\rho^2 + \delta^2)} \tag{2.18}$$

and there is clearly a maximum bound to the value of u given by $u_{max} = \Gamma/(4\pi\delta)$ at $r = \delta$. So the finite core parameter δ acts as a cutoff such that $p_i(u_i; r)$ is zero for $u_i > u_{max}$. We will see later that this has significant consequences for the velocity statistics for the entire field.

The mean for the velocity contribution of each vortex is given by

$$\langle u_i(r) \rangle = \int u_i p_i(u_i; r) du_i, \tag{2.19}$$

which exists for both finite and zero δ for our vortex problem. The variance

$$\left\langle [u_i(r) - \langle u_i(r) \rangle]^2 \right\rangle = \int u_i^2 p_i(u_i; r) du_i \tag{2.20}$$

on the other hand, does not exist for the $\delta = 0$ case. Simply, this is because the integral in Eq. (2.20) diverges as the upper limit $\to \infty$ because of the u_i^{-3} power-law tail of $p_i(u_i)$. We can see however, that Eq. (2.20) converges for the de-singularized ($\delta \neq 0$) case because $p_i(u_i; r) = 0$ for $u_i > u_{max}$, and $p_i(u_i; r) = 0$ for $u_i < u_{min}$, where $u_{max} = \Gamma/4\pi\delta$ and $u_{min} = -\Gamma/4\pi\delta$. The existence of the variance is an important factor in the use of the central limit theorem to construct the PDF for the total velocity, $u(\mathbf{r})$, as shown in the next section.

2.2.2 Limit distributions: central limit theorem and stable distributions

In the study of sums of independent random variables of the form

$$X = \sum_{i=1}^{N} X_i \tag{2.21}$$

where X_i have a common distribution $p_i(X_i)$, the central limit theorem establishes the conditions under which X is asymptotically normally distributed. In its simplest form, the the central limit theorem states [41] that for a system with mean $E(X) = 0$ and variance $\sigma^2 = 1$, as $N \to \infty$ the distribution of the normalized sum

$$X_N^* = \frac{1}{N} \sum_{i=1}^{N} X_i \tag{2.22}$$

tends to the normal distribution with the density

$$p(X) = \frac{1}{\sqrt{2\pi}} e^{-X^2/2} \, . \tag{2.23}$$

As applied to our N-vortex problem, *if* the velocity contribution of each vortex $u_i(r)$ can be considered an *independent, identically distributed* random variable, then as $N \to \infty$, $p(u;r)$ approaches a normal distribution regardless of the shape of the individual density function $p_i(u_i)$, provided the mean and the variance exists. However, it was shown above that for the singular core ($\delta = 0$), a finite variance does not exist, and so when we compute $p(u;r)$, we expect a non-Gaussian distribution. On the other hand, we do expect a Gaussian $p(u;r)$ for the de-singularized case ($\delta \neq 0$) since the variance is finite. However, there are the important conditions of large N and identical $p_i(u_i)$ distributions that need to be satisfied. Deviation from Gaussian behavior is also expected even for large N, if the vortices are grouped in a small number of clusters, such that the the large scale dynamics are similar to a small N case.

For the singular case, it will be useful to bring up the topic of Lévy stable distributions which arise in the study of sums of identically distributed, independent, random variables. Essentially, these are $p_i(u_i)$ that have the same form as the distribution of the sum u, $p(u)$ [83, 41]. Such distributions can be found by considering the relationship between a probability density function $p(u)$ and its characteristic function $\phi(k)$:

$$\phi(k) = \langle e^{iku} \rangle = \int_{-\infty}^{\infty} e^{iku} p(u) du \tag{2.24}$$

$$p(u) = \frac{1}{2\pi} \int_{-\infty}^{\infty} e^{-iku} \phi(k) dk. \tag{2.25}$$

And defining

$$\phi_i(k) = \langle e^{iku_i} \rangle = \int_{-\infty}^{\infty} e^{iku_i} p_i(u_i) du_i, \tag{2.26}$$

it is seen that

$$\phi(k) = \prod_{i=1}^{N} \phi_i(k). \tag{2.27}$$

It is then clear that characteristic functions of the form

$$\phi_i(k) = e^{-a_i |k|^\alpha}, \quad 0 < \alpha \leq 2 \tag{2.28}$$

produce

$$\phi(k) = e^{-a|k|^\alpha}, \quad 0 < \alpha \leq 2 \tag{2.29}$$

where $a = \sum a_i$. These have been found to be the general form of the Lévy stable distributions. The conditions on the range of α is imposed by the fact that $\int p(u) du = 1$. The α's are known as the characteristic exponents, with $\alpha = 2$ being the Gaussian distribution and $\alpha = 1$ being the Cauchy distribution. In regard to the central limit theorem, for $\alpha \neq 2$, the distributions $p_i(u_i)$ associated with Eq. (2.28) do not have second moments (variance) and thus do not produce a normal distribution $p(u)$.

For large u and $0 < \alpha < 2$, Eq. (2.29) gives us the asymptotic form [83] for the

probability density function

$$p(u) \sim \frac{\Gamma(\alpha) \sin \frac{1}{2}\pi\alpha}{\pi |u|^{\alpha+1}} \quad 0 < \alpha < 2. \tag{2.30}$$

This has a power-law tail similar to that derived in section 2.2.1 for our N-vortex system, suggesting the possibility that the PDF of the velocities in the N-vortex system follows a Lévy stable distribution with the characteristic exponent $\alpha = 2$. However, since Eq. (2.30) is valid only in the range $0 < \alpha < 2$, the $\alpha = 2$ power-law association with the stable distribution is not quite correct (also see below in reference to Takayasu's paper). At any rate, the match in the PDFs Eq. (2.30) and (2.15) holds true only for the tails, and so the vortex system is most likely not a strictly stable distribution. What this connection to stable distributions illustrates though, is that the same mechanism that leads all stable distributions other than the Gaussian to *not* fall under the domain of attraction of the Gaussian is at work for our point vortex system as well — namely the non-existence of the variance that follows from the power-law tails.

The *physical* reason for the property of velocity probability density due to *all* vortices approaching that due to each *single* vortex, is clear if we consider the fact that the closest vortex always dominates the shape of the high u tails. In fact, as discussed by Chandrasekhar [22] in the context of stellar dynamics, the analysis above could have been done on the basis of the nearest neighbor estimate. It is also then clear why $p(u; r)$ moves towards the Gaussian as N is increased — the more densely packed the vortices are, the less a single vortex dominates.

Because vorticity is more likely to be encountered in non-singular, blob form rather than in point vortex singularities, the conditions stated here for the observation of Gaussian statistics are quite favorable. However, the condition of having identically distributed vorticity may be difficult to meet in a more general physical situation, since vortices of different sizes may be found in a given flow. And as mentioned earlier, departure from Gaussian behavior is also expected for small N, or

large N cases when the vortices form a small number of distinct clusters, mimicking the behavior of small N dynamics.

An approach similar to that discussed above has been previously put forth by Takayasu [108], who adopts the analysis of the Holtzmark distribution [22] for the gravitational force field around a star for the velocity field around a vortex. The similarity lies in the fact that the vortex-velocity relationship is given by the Biot-Savart law with its r^{-2} dependence (in three-dimensions) and the star-force relationship is given by the r^{-2} inverse gravitational law. In [108] it is taken as a given that the spatial distribution of point vortices is fractal (what he terms "fractal turbulence"). To highlight the differences with our study, we point out that [108] deals exclusively with the point vortex model (as opposed to non-singular vortex blob type models). This has serious consequences, as discussed earlier — non-singular vortices tend to produce Gaussian statistics, while point vortices do not. Our model provides an understanding of how the statistics change as the vorticity distribution is changed. We believe that in most physical flows (especially two-dimensional flows), the vorticity distribution is not singular, and that the vortex blob model provides a better physical representation. Takayasu also argues that for the two-dimensional case, $p(u)$ is a stable distribution with $\alpha = 2$, and thus that $p(u)$ must be Gaussian. We disagree on the grounds that for this to be true, $p_i(u_i)$ must also be a Gaussian, which is false since we know it to have a -2 exponent power-law tail. For the point vortex, $p(u)$ is not Gaussian (though it cannot strictly be a stable distribution either).

2.3 PDF of the velocity difference

The probability distribution for the velocity difference $p_\delta(\delta u(\mathbf{r}; d\mathbf{r}))$ is examined, where $\delta u(\mathbf{r}; d\mathbf{r}) = u(\mathbf{r} + d\mathbf{r}) - u(\mathbf{r})$. We apply the same method used in constructing the velocity field based on the sum of the contributions of the individual vortices to study the PDF of the velocity difference measured at a fixed point $\mathbf{r}$. Decomposing

the velocity difference,

$$\delta\mathbf{u}(\mathbf{r}, d\mathbf{r}) = \sum_{i=1}^{N} \delta\mathbf{u}_i(\mathbf{r}, d\mathbf{r}), \tag{2.31}$$

where the contribution of each vortex is

$$\delta\mathbf{u}_i(\mathbf{r}; d\mathbf{r}) = -\frac{\Gamma_i}{2\pi}\left[\frac{(\mathbf{r}-\mathbf{r}_i)\times\hat{\mathbf{e}}_z}{|\mathbf{r}-\mathbf{r}_i|^2} - \frac{(\mathbf{r}+d\mathbf{r}-\mathbf{r}_i)\times\hat{\mathbf{e}}_z}{|\mathbf{r}+d\mathbf{r}-\mathbf{r}_i|^2}\right]. \tag{2.32}$$

Now assuming that

$$|d\mathbf{r}| \ll |\mathbf{r}-\mathbf{r}_i|, \quad |\mathbf{r}+d\mathbf{r}-\mathbf{r}_i|^2 \approx |\mathbf{r}-\mathbf{r}_i|^2, \tag{2.33}$$

$$\delta\mathbf{u}_i(\mathbf{r}; d\mathbf{r}) \approx -\frac{\Gamma_i}{2\pi}\left[\frac{(\mathbf{r}-\mathbf{r}_i)\times\hat{\mathbf{e}}_z \;-\; (\mathbf{r}+d\mathbf{r}-\mathbf{r}_i)\times\hat{\mathbf{e}}_z}{|\mathbf{r}-\mathbf{r}_i|^2}\right], \tag{2.34}$$

$$\delta\mathbf{u}_i(\mathbf{r}; d\mathbf{r}) \approx \frac{\Gamma_i}{2\pi}\left[\frac{d\mathbf{r}\times\hat{\mathbf{e}}_z}{|\mathbf{r}-\mathbf{r}_i|^2}\right]. \tag{2.35}$$

The x and y components are

$$\delta u_i(\mathbf{r}; \delta\mathbf{r}) \approx \frac{\Gamma_i}{2\pi}\frac{dr\sin\beta}{|\mathbf{r}-\mathbf{r}_i|^2} \tag{2.36}$$

$$\delta v_i(\mathbf{r}; \delta\mathbf{r}) \approx -\frac{\Gamma_i}{2\pi}\frac{dr\cos\beta}{|\mathbf{r}-\mathbf{r}_i|^2}, \tag{2.37}$$

where

$$\tan\beta \equiv \frac{\delta y}{\delta x}, \quad d\mathbf{r} = dx\hat{\mathbf{e}}_x + dy\hat{\mathbf{e}}_y \tag{2.38}$$

and

$$\delta u(\mathbf{r}, d\mathbf{r}) = \sum_{i=1}^{N} \delta u_i(\mathbf{r}, d\mathbf{r}), \tag{2.39}$$

$$\delta v(\mathbf{r}, d\mathbf{r}) = \sum_{i=1}^{N} \delta v_i(\mathbf{r}, d\mathbf{r}). \tag{2.40}$$

Using derivation similar to section 2.2.1 it can be shown that

$$p_{\delta_i}(\delta u_i) \sim \delta u_i^{-2} \quad \text{for large} \quad \delta u_i\,. \tag{2.41}$$

An interesting feature develops in comparing the PDFs of u and δu constructed as sums of the above individual contributions for the de-singularized case. Letting $\rho \equiv |\mathbf{r} - \mathbf{r}_i|$, u is a sum of terms that are proportional to $1/\rho$, while δu is a sum of terms that are proportional to $1/\rho^2$. This results in a flatter tail for $p_{\delta_i}(\delta u_i)$ as compared to $p_i(u_i)$, as seen by Eqs. (2.41) and (2.15). In terms of $p_\delta(\delta u)$ and $p(u)$, because of the N dependence of the central limit theorem, for a fixed N, $p(u)$ will be much closer to a Gaussian distribution than $p_\delta(\delta u)$. This retention of the power-law form for $p_\delta(\delta u)$ is a reflection of the fact that the influence of a single vortex at $\mathbf{r}$ decays more rapidly for the velocity difference as opposed to the velocity itself. This is in agreement with experiments and direct simulations of turbulence ([113, for example]) where the probability distribution of the velocity is normally distributed while the PDF for the gradient of the velocity either tends more towards an exponential or power law tail. The structure function $F_n = \langle [\delta u(dr)]^n \rangle$ for this simple two-dimensional model displays a $(dr)^n$ dependence (for small dr). This follows from Eq(2.35) which shows that $\delta u \sim dr$. In fact, it is easy to show that this must hold true for small dr for *any* flow, by linearizing u about r.

2.4 PDF of the three-dimensional vorticity distribution

Although we have been dealing entirely with vortex distributions in two dimensions, it is possible to extend the results to three dimensions. We must however discuss an appropriate form for the spatial distribution of the vorticity. Just as the vorticity in two dimensions was discretized to a collection of N delta functions or smooth core structures, the vorticity in three dimensions is often discretized in the form of vector valued vortex particles (vortons) or vortex filaments [69]. Considering the

vector particle approach, the vorticity is given by [70]

$$\omega(\mathbf{x},t) = \sum_{i}^{N} \alpha_i \gamma_i(\mathbf{x} - \mathbf{x}_i(t)) \tag{2.42}$$

where α_i has the units of circulation times length, and the spatial distribution for each vortex is given by some function $\gamma(\mathbf{x})$

$$\gamma_i(\mathbf{x}) = \frac{1}{\sigma_i^3} p(|\mathbf{x}|/\sigma_i) \tag{2.43}$$

with an effective core radius σ_i. This can in turn be substituted into the Biot-Savart equation for three dimensions

$$\mathbf{u}(\mathbf{x}) = -\frac{1}{4\pi} \int \frac{(\mathbf{x} - \mathbf{x}') \times \omega(\mathbf{x}')}{|\mathbf{x} - \mathbf{x}'|^3} d\mathbf{x}' + \nabla\phi \,, \tag{2.44}$$

to obtain a discrete form the velocities of the N vortex elements.

Consider a situation where the vector vortex elements are randomly (uniformly) distributed in space. This is of course a condition that may or may not be dynamically realizable, possibly due to the clustering and alignment of the vortex elements. For our current purposes we limit ourselves to kinematically examining the results of a random distribution.

Following a derivation similar to section 2.2.1, we provide a rough heuristic sketch leading to the result $p_i(u_i) \sim u_i^{-5/2}$. The induced velocity component in the x direction due to a single vortex element is given by

$$u_i \sim \frac{1}{\rho^2} \tag{2.45}$$

where $\rho \equiv |\mathbf{x} - \mathbf{x}_i|$ as before. The probability of having u_i larger than a given value U is

$$P(u_i > U) \sim \rho^3 \sim \frac{1}{U^{3/2}} \,. \tag{2.46}$$

Therefore,

$$p_i(u_i) \sim u_i^{-5/2} \, . \tag{2.47}$$

As in the two-dimensional case, the mean exists but the variance does not. Of course, the conditions under which the vortex motion can be considered random and independent are quite different from the two-dimensional case, and require further investigation.

2.5 Numerical simulations

The velocity field due to N vortices in the stationary configuration discussed in Chapter 1 was numerically studied. Figure 2.2 shows typical probability densities $p_1(r)$ (defined in section 1.2.3 of Chapter 1) at the beginning and end of the simulations with the predicted equilibrium curve. Our numerical simulations provide a limited validation of the closure scheme proposed by Lundgren and Pointin [75] for the equilibrium vortex state, at least for initial configurations that start off with the predicted solution. We believe the equilibrium state of other initial vortex configurations that are more clustered, is an open question.

Assuming there is no θ dependence in the mean, the mean velocity can be evaluated by using Stokes' theorem

$$\int_c \mathbf{u} \cdot d\mathbf{l} = \int_A \omega dA \tag{2.48}$$

and averaging over an ensemble of possible configurations,

$$\langle u_\theta(r) 2\pi r \rangle = \left\langle \int_0^r \omega 2\pi r' dr' \right\rangle \tag{2.49}$$

$$2\pi r \langle u_\theta(r) \rangle = \int_0^r \langle \omega \rangle 2\pi r' dr'. \tag{2.50}$$

Making use of

$$\langle \omega(r) \rangle = \Gamma p_1(r) \tag{2.51}$$

and

$$p_1(r) = \frac{1}{\pi} e^{-r^2} \tag{2.52}$$

as described in section 1.2.3 of Chapter 1,

$$2\pi r \langle u_\theta(r) \rangle = \Gamma \int_0^r p_1(r') 2\pi r' dr' \tag{2.53}$$

$$\langle u_\theta(r) \rangle = \frac{\Gamma}{\pi r} \int_0^r e^{-r'^2} r' dr' = -\frac{1}{2\pi r} \left[e^{-r^2} - 1 \right]. \tag{2.54}$$

This average tangential velocity profile, $\langle u_\theta(r) \rangle$ is compared with the results of a typical numerical simulation in Figure 2.3.

For large N and finite δ, we can summarize the velocity field as consisting of a distinct large scale mean field, with statistical fluctuations about it. By statistical, we mean roughly that the law of large numbers is followed, which states that if the mean exists and the variance σ_i^2 (due to each vortex) is finite, then $\sigma^2 \sim \sigma_i^2/N$. This implies that as $N \to \infty$, the fluctuations die out. This is seen in our simulations.

The PDF $p_i(u_i; r)$ is plotted in Figure 2.4, along with a u_i^{-3} power-law function for comparison. The normalized PDF $p(u; r)$ of $u = \sum u_i$ at $r = .4$, computed from a simulation with $\delta \neq 0$ is shown in Figure 2.5, along with a Gaussian curve. The fit is quite good, in contrast to the $\delta = 0$ case shown in Figure 2.6 where the fit is to a power law curve. Another demonstration of the statistical behavior of the $\delta \neq 0$ case is the $1/N$ dependence of the variance on N. This is shown in Figure 2.7. It is not possible to plot a similar curve for the $\delta = 0$ case because a finite variance does not exist.

For the velocity difference, Figure 2.8 shows the PDF of δu compared to PDF of u, both from a numerical simulation of 422 vortex blobs. The distribution for the velocity approaches Gaussian, while that of the velocity difference is clearly not so.

The Gaussian behavior is expected to breakdown as N is made smaller. This trend is shown in Figure 2.9 in which the flatness (fourth moment/(second moment)^2) of $p(u;r)$ is plotted versus N. Only for relatively large N does the flatness reach the value three corresponding to a Gaussian distribution. The PDF for a simulation with $N = 6$ and $\delta = .0033$ shows normalized $p_i(u_i;r)$ compared with $p(u;r)$. It can be seen that both curves have the same power-law tail profile, quite far from Gaussian, as displayed in Figure 2.10.

2.6 Lagrangian statistics

For homogeneous turbulence the Lagrangian velocity probability densities are identical to the Eulerian velocity statistics [109]. For our vortex configuration which is *not* homogeneous (average velocity is a function of r), the Lagrangian velocity statistics are quite different from the Eulerian ones. Based on our knowledge of the Eulerian mean velocity and the additional finding that the Eulerian velocity fluctuations are proportional to $p_1(r)$, we are able to analytically compute the Lagrangian velocity PDF that compares well to the data obtained from numerical simulations.

2.6.1 Velocity fluctuation dependence on r

The Eulerian velocity fluctuation measured at a fixed r is proportional to the density of the vortex population $p_1(r)$. Figure 2.11 compares the result of numerical computations of the variance $\sigma^2(r)$ as a function of r with the known profile for the density of the vortices $p_1(r)$. Viewing the fluctuations as being caused by the passage of vortices during their trajectory, closer encounters are made for denser vortex populations, resulting in larger deviations from the mean.

2.6.2 PDF of Lagrangian velocity

The PDF of the Lagrangian velocity sampled by a passive particle $p(|\mathbf{u}_L|)$ is shown in Figure 2.12 for a typical case, along with a curve constructed from the model to be discussed below. The notable feature is that it has a long low $|\mathbf{u}_L|$ tail, similar to a (negative) log-normal distribution, and distinctly different from the Eulerian distributions we have observed thus far in this study. This difference is a consequence of the fact that the velocity distributions are not spatially uniform, so as a particle moves about, it samples different statistics, and since the PDF at various r do not share the same mean or variance, it is not possible to apply a central limit theorem type of analysis.

An analytical estimate of the Lagrangian statistics from the Eulerian ones can be computed from the equation

$$p_L(|\mathbf{u}_L|) \sim \int_0^\infty p(u;r)p_1(r)2\pi r dr \tag{2.55}$$

and assuming

$$p(u;r) = \frac{1}{\sqrt{2\pi}\sigma(r)} e^{-[u-\overline{u}(r)]^2/2\sigma^2(r)}, \tag{2.56}$$

$\sigma^2(r)$ is obtained from section 2.6.1, and $\overline{u}(r)$ and $p_1(r)$ are analytically known. As shown in Figure 2.12 this provides quite a good estimate when compared to the values from the simulation.

2.6.3 Integral time scales

The integral time scale is defined as the area under the autocorrelation coefficient curve

$$T = \int_0^\infty c(\tau)d\tau \tag{2.57}$$

where the autocorrelation coefficient

$$c(\tau) \equiv \frac{\overline{[u(t)-\overline{u}][u(t-\tau)-\overline{u}]}}{\overline{[u-\overline{u}]^2}}. \tag{2.58}$$

And because of stationarity, $\overline{u} = \overline{u(t)} = \overline{u(t-\tau)}$. A typical plot of the autocorrelation function for the Eulerian and Lagrangian velocity $|\mathbf{u}|$ and $|\mathbf{u}_L|$ is shown in Figure 2.13. The time scales are quite different, as is also apparent from Figure 2.14 which show the velocities themselves. For the same simulation, ($N = 270$ and $\delta = .1$), $T_E \approx 10$ while $T_L \approx 50$. The reason for the difference is the 'sweeping' effect of the vortices on a stationary observer (Eulerian viewpoint), and the absence of such an effect on a moving observer (Lagrangian viewpoint).

2.7 Summary

We have described the velocity field statistics for the N vortex problem, using a decomposition of the Eulerian velocity at a fixed point into a sum of N individual components whose contributions are supplied by the velocity induced by a single vortex. This allows us to make use of limit distribution theorems to describe the velocity at the fixed point, based on the spatial distribution of vorticity. In particular, the tails of the velocity distribution of individual vortices have been used to show that there is a qualitative difference in the passive field statistics for the singular and the non-singular vortices. The kinematics behind the non-Gaussian form of the velocity difference distribution was determined, which is related to the relative flatness of $p_\delta(\delta u_i)$ tail compared to that of $p_i(u_i)$.

We believe the N vortex system addresses two aspects of vortical flows. One is the coherent, large scale organized motion of many vortices (of the same sign), and the other is the interaction *between* these coherent vortex blobs. We show here that the two cases demonstrate distinct statistical properties.

Vortex methods are also often used in modeling turbulent flows such as the mixing layer. The statistics collected from such simulations have to carefully considered in light of the above discussion on the existence of the variance and the dependence of the variance on the value of δ.

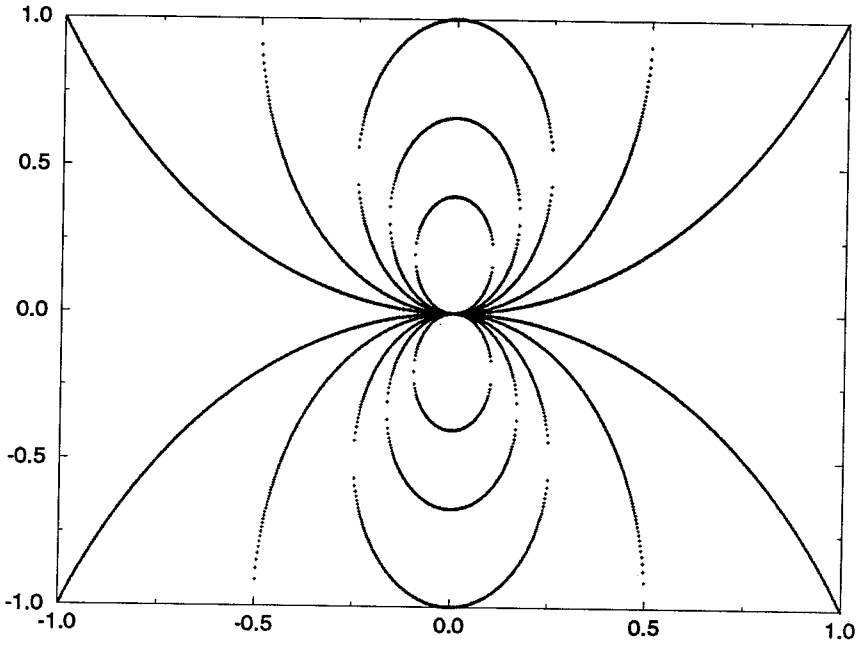

Figure 2.1: Lines of constant U (the velocity component due to a single vortex) around a point

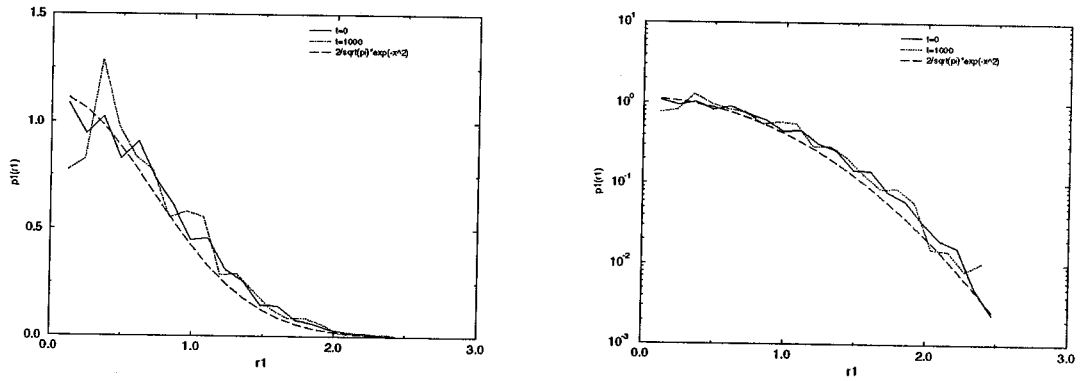

Figure 2.2: Log and linear plots of $p_1(r_1)$ vs r_1 for $N = 913$, $\delta = .0033$ at $t = 0$ and $t = 1000$

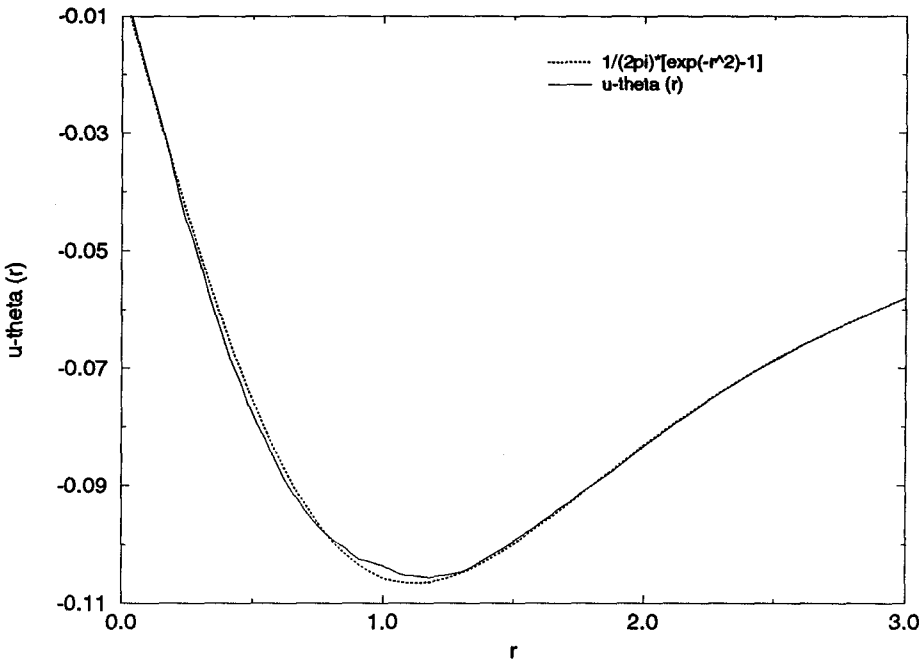

Figure 2.3: $\langle u_\theta(r) \rangle$ for $N = 913,\ \delta = .0033$

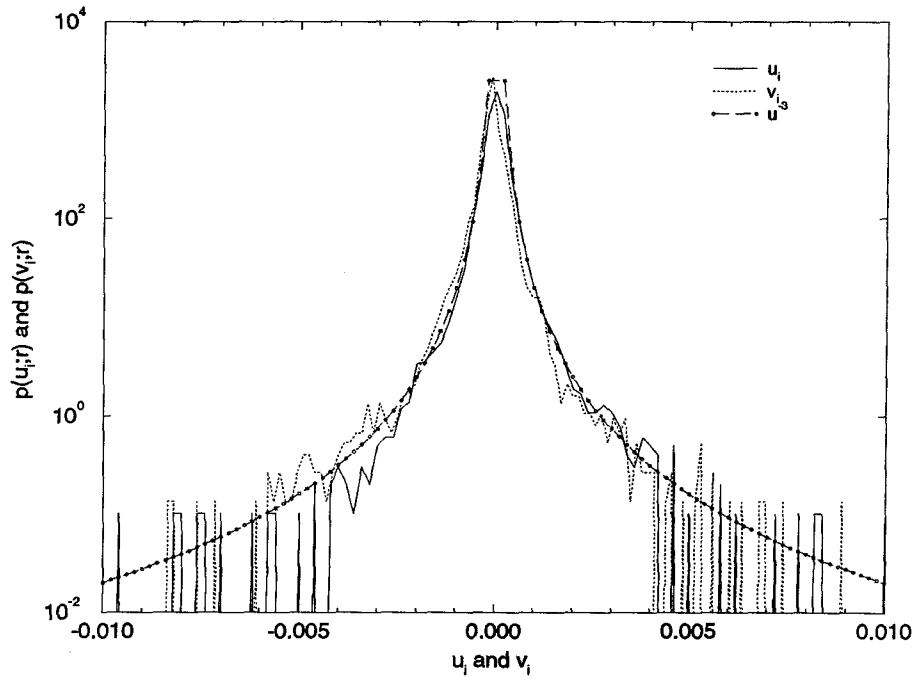

Figure 2.4: $p_i(u_i; r)$ and $p_i(v_i; r)$ for $N = 913,\ \delta = 0$ at $r = .4$

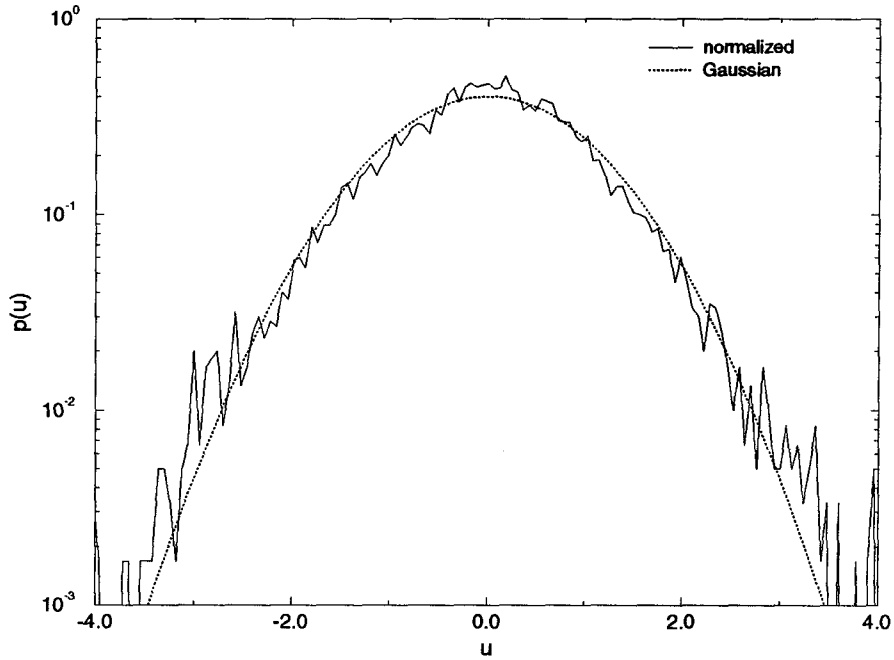

Figure 2.5: Normalized $p(u;r)$ for $N = 270,\ \delta = .1$ at $r = .4$

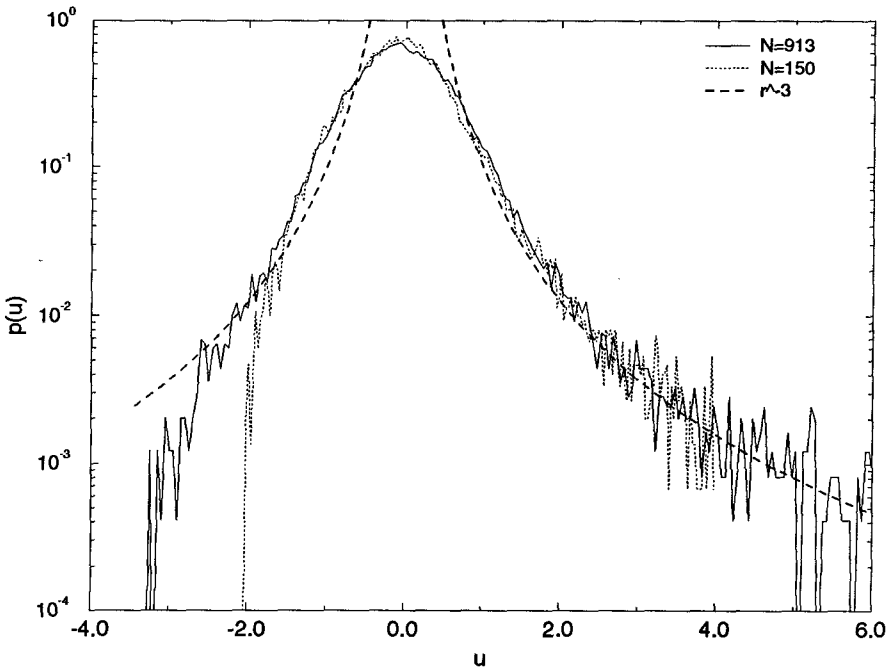

Figure 2.6: Normalized $p(u;r)$ for $N = 913$ and $N = 150,\ \delta = 0$ at $r = .4$

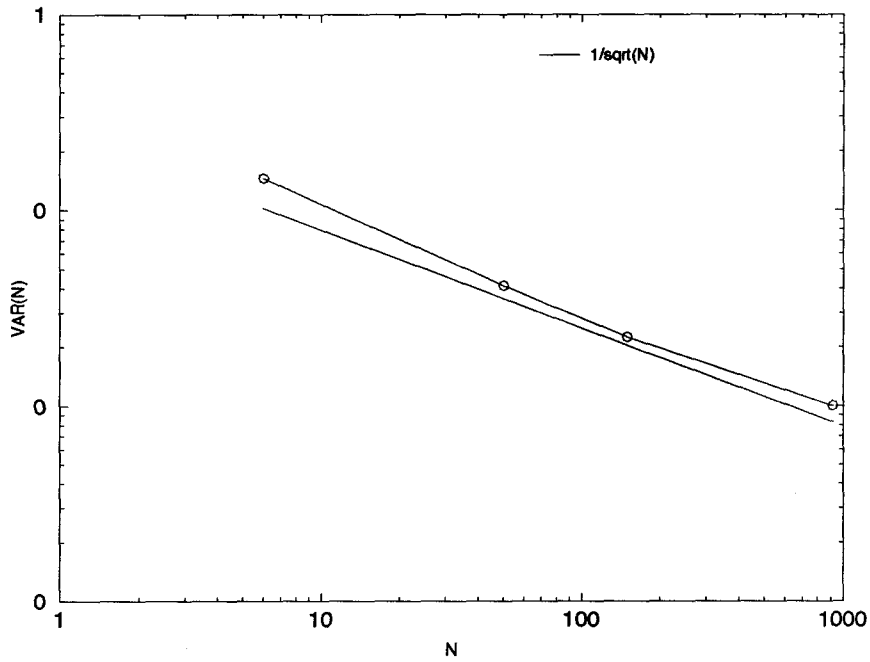

Figure 2.7: Variance of $u(r)$ vs N for $\delta = .0033$ at $r = .4$

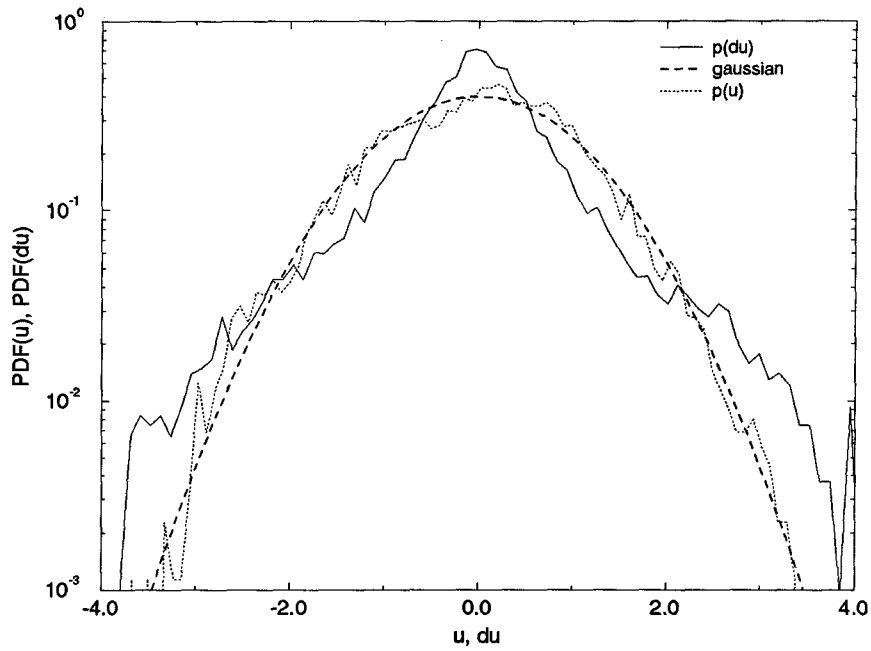

Figure 2.8: Normalized $p_\delta(\delta u; r)$ compared with $p(u; r)$ for $N = 422, dx = .001$, $\delta = 0.01$ at $r = .4$

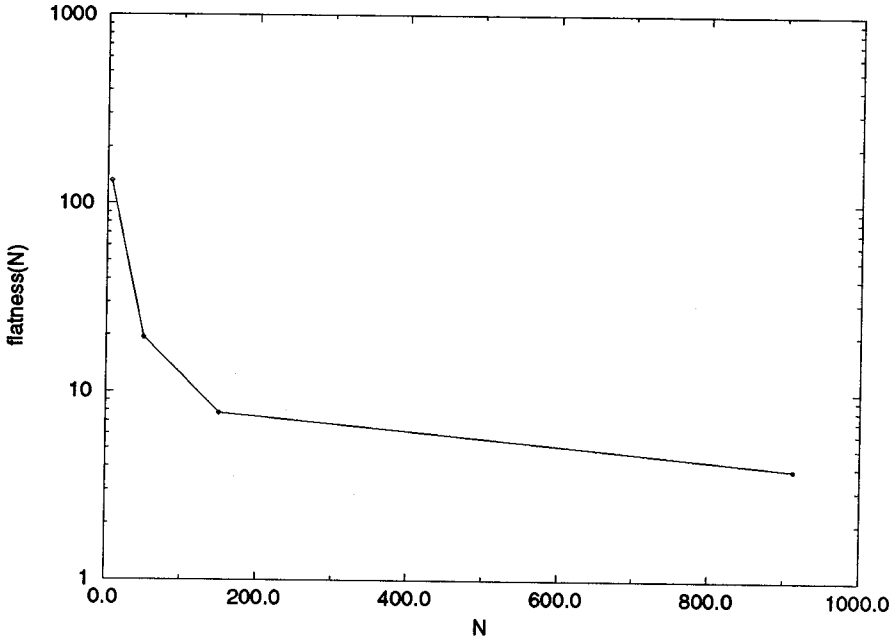

Figure 2.9: Flatness μ_4 as a function of N for fixed δ, showing convergence towards the value 3 for large N

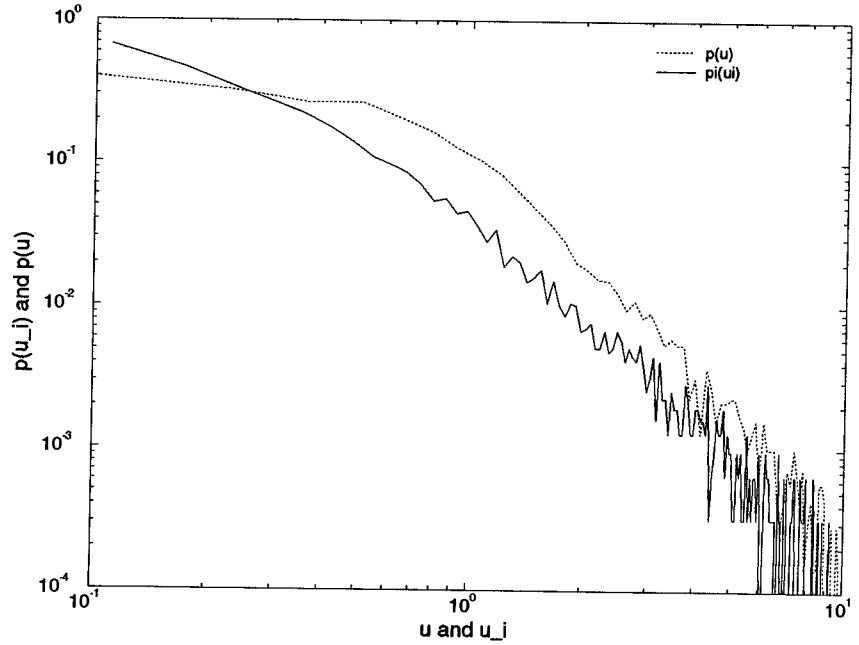

Figure 2.10: Normalized $p_i(u_i; r)$ compared with $p(u)$ for $N = 6$, $\delta = .0033$ at $r = .4$

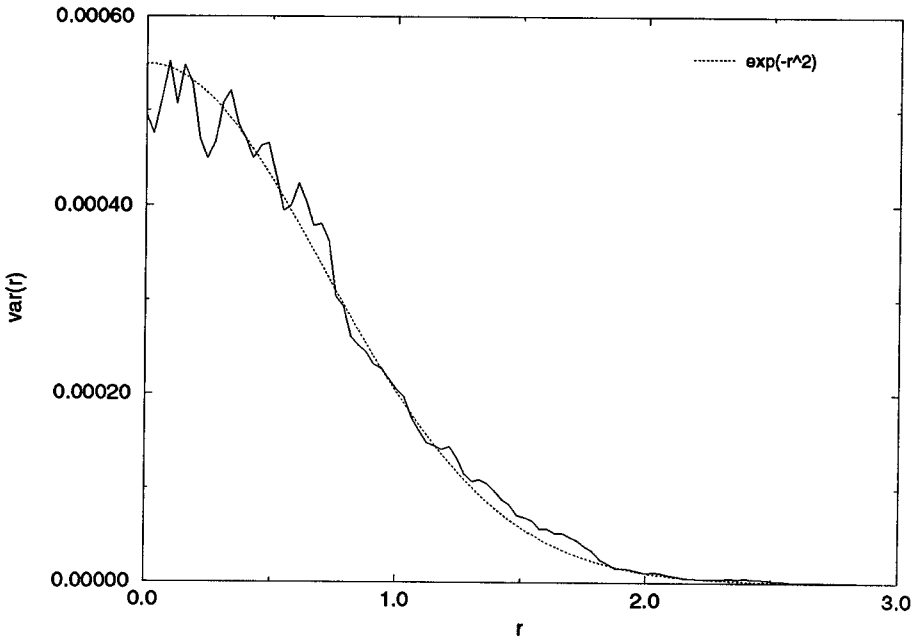

Figure 2.11: Variance of $u(r)$, $\sigma^2(r)$ vs r for $N = 150$, compared with the density of vortices, which follows the function e^{-r^2}

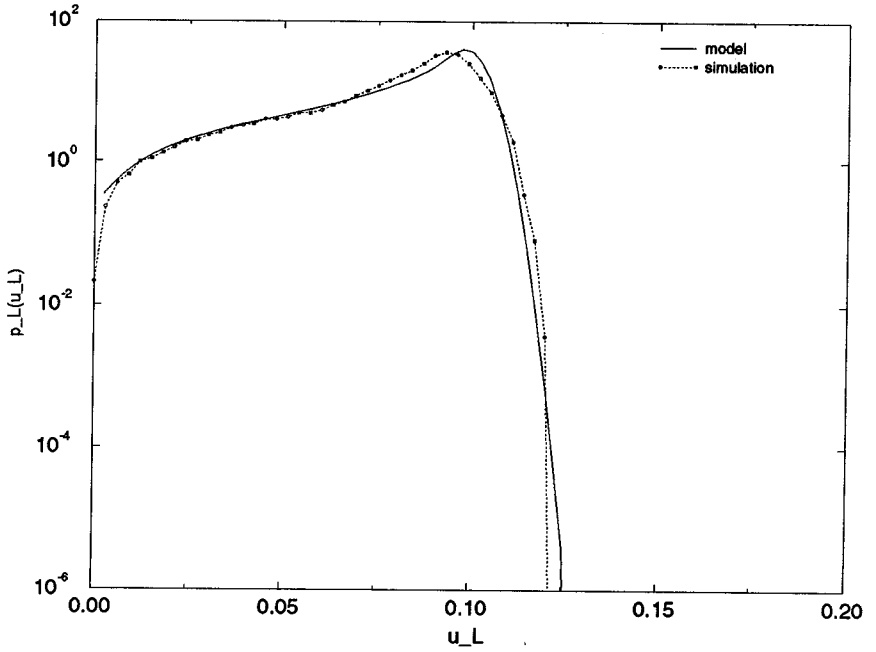

Figure 2.12: PDF of Lagrangian velocity u_L, $p_L(u_L)$ for $N = 270$, $\delta = .1$

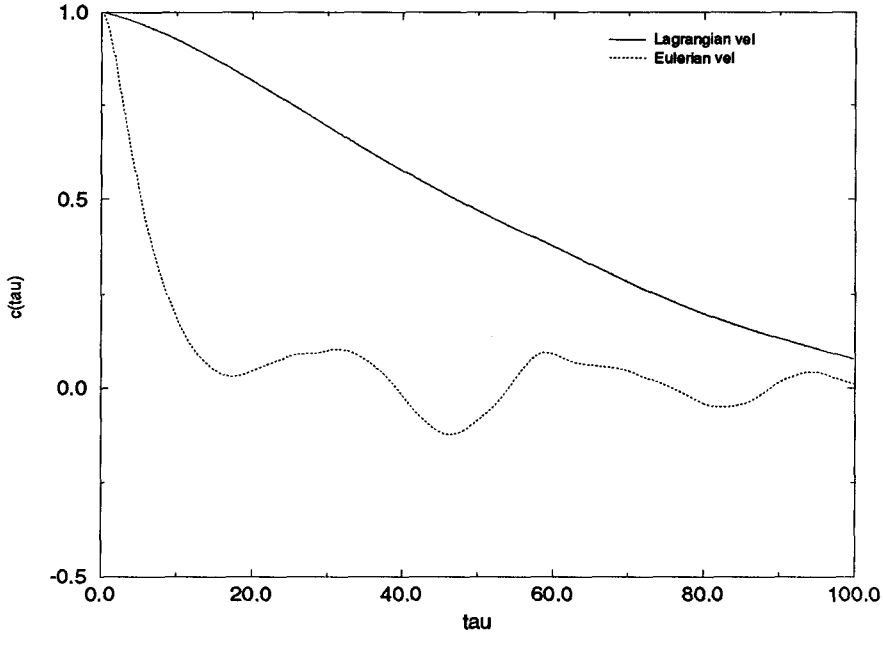

Figure 2.13: Comparison of autocorrelation of Lagrangian ($u_L = |\mathbf{u}_L|$) and Eulerian ($u = |\mathbf{u}|$) velocity signals for $N = 270,\ \delta = .1$

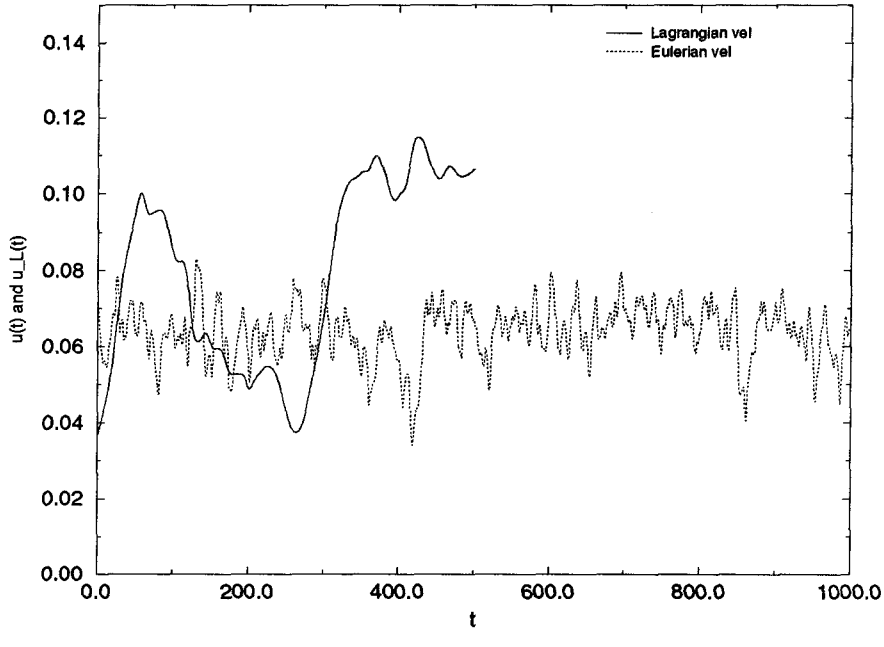

Figure 2.14: Lagrangian $u_L = |\mathbf{u}_L|$) and Eulerian ($u = |\mathbf{u}|$) velocity signals for $N = 270,\ \delta = .1$

Chapter 3

Stretch Statistics of the N-vortex Problem

3.1 Introduction

Why is stretching in the N-vortex problem of interest? We have already discussed in Chapter 1 the importance of studying the N-vortex problem in fluid mechanics and dynamical systems. Stretching of fluid is related to stirring and mixing via the increase of interfacial areas, which brings different fluids together and allows for local diffusion to take place. The relevance of line stretching to fluid mixing is best illustrated by considering an interfacial line that divides two fluids (of scalar value $\xi = 1$ and $\xi = 0$). For low diffusion flows, we can assume that mixing takes place in thin diffusive layers near the interface and mixing between two fluids can be quantified by the length of the interfacial line. In dynamical systems, the divergence of nearby trajectories in phase space is measured by the Lyapunov exponent, which is often seen as an indicator of chaotic particle trajectories. This exponent is the measure of exponential stretch of infinitesimal 'fluid' elements in physical space.

To characterize the stretching, the probability density function (PDF) $p(\lambda)$ are computed, where λ is the finite-time Lyapunov exponent (i.e. the finite time average of the strain experienced by an infinitesimal line segment along its trajectory). In Section 3.3 we present the results obtained from numerical computations of $p(\lambda)$ for various values of the parameters N and δ. The purpose of this is to demonstrate the different types of stretching (and hence mixing) that can result from the interaction of N vortices. As will be discussed in Section 4, $p(\lambda)$ and its high stretch tails are extremely important in the evolution of *line* stretching in the flow.

Stretching and mixing properties of two-dimensional flows and maps [86, 92, 95, 107, 111], as well as in simple vortex flows in particular [12, 14, 92, 102] have previously been investigated. We apply the study of stretching and mixing to vortical flows that embody the complex nonlinear inter-vortex relationships that are present in high Reynolds number turbulent flows. On the other hand the system is simple enough so that we are able to discern the basic mechanism behind statistics that we observe.

The *spatial* distribution of this stretched interface is of course important as well, since we want mixing to involve all fluids and not the same ones over and over again — this becomes especially important in the presence of molecular diffusion when some of the small scales are wiped out and stirring beyond a certain scale does not increase mixing. This issue is addressed in Chapters 4 and 5.

In the next section the definitions and the general properties of stretching processes are discussed. As described in Chapter 1, the numerical simulations were performed from equilibrium initial conditions for the vortices such that we have a stationary process. The results of these simulation are presented in Section 3.3, and the discussion of the results in terms of some models in Section 3.4.

3.2 Stretch distributions

The equation of motion of an infinitesimal line segment $\delta\mathbf{l}$ is

$$\frac{d}{dt}\delta\mathbf{l} = (\delta\mathbf{l}\cdot\nabla)\mathbf{u}, \tag{3.1}$$

where $\mathbf{u}$ is the velocity field, provided in this case by the instantaneous position of the N-vortices. The corresponding equation in tensor form for the stretch experienced by this line segment in the time interval dt is

$$\delta l_i(dt) = \delta u_i dt = \frac{\partial u_i}{\partial x_j}\delta l_j(0)dt. \tag{3.2}$$

Let

$$\delta l \equiv |\delta\mathbf{l}|.$$

Define the instantaneous stretch exponent μ as

$$\mu = \ln\frac{\delta l(dt)}{\delta l(0)}. \tag{3.3}$$

Note that $\mu = \mu(\mathbf{x}, t)$ and depends on how $\delta l(0)$ is aligned with respect to the eigenvectors of the velocity gradient tensor du_i/dx_j.

The Lyapunov exponent is defined as follows [74, 107]

$$\lambda = \lim_{t\to\infty}\frac{1}{t}\ln\frac{\delta l(t)}{\delta l(0)}, \tag{3.4}$$

where $\delta l(0)$ is the initial infinitesimal line segment length and $\delta l(t)$ is the segment length after it has been stretched by the flow. The finite-time version of this exponent is

$$\lambda(t) = \frac{1}{t}\ln\frac{\delta l(dt)}{\delta l(0)}. \tag{3.5}$$

This is evaluated through the Lagrangian trajectory of particles, and at a finite time

t, we can expect a distribution of these finite-time Lyapunov exponent values from an ensemble of particles.

3.2.1 Point collection and line collection

The fluid stretch statistics are evaluated using two techniques. One involves computing the finite-time lyapunov exponents of a fixed number of particles in the usual way. (We will refer to this as *point collection.*) *Line collection* involves tracking the evolution of a line segment (which is approximated by closely spaced particles) as it is stretched by the flow. Particles are inserted during the simulation when the distance between adjacent points exceeds a certain length (ds_{min}). The addition of points allow a better probe of the high stretch regions. Another attribute of line collection is that a spatial distribution of the line is obtained, which gives us a better understanding of the stretching mechanism involved, as shown in Figure 3.1.

We show that by appropriate normalization the two methods provide similar statistics, while both methods retain their advantages and disadvantages depending on the situation. Namely, point collection may fail to provide sufficient resolution for high stretch statistics, while line collection cannot be simulated for long times because the computational requirements simply become too great for even the fastest supercomputers of today (see for example [42]).

Let us define the stretch exponent on an interfacial line to be (λ_L). This is just the Lyapunov exponent as computed for the point collection, except that we have as our set of points a highly selectively chosen set — i.e. those points that have undergone stretching along the line. Because of this weighting, the relationship between the PDF of the finite time Lyapunov exponents λ and the PDF of stretch exponents λ_L on a material line is approximately

$$p_L(\lambda_L;t) = \frac{p(\lambda)e^{\lambda t}}{\int_{-\infty}^{\infty} p(\lambda;t)e^{\lambda t}d\lambda} \tag{3.6}$$

or to compute the Lyapunov exponent distribution from the line stretch statistics,

$$p(\lambda) = \frac{p_L(\lambda_L; t)e^{-\lambda t}}{\int_{-\infty}^{\infty} p_L(\lambda_L; t)e^{-\lambda t}d\lambda}. \tag{3.7}$$

In confining ourselves to the interfacial line of small but finite thickness, there is equal probability of encountering a thin section as it is a thick section. Therefore, due to the fact that there is bound to be more of the highly stretched lines (due precisely to the high stretching), $p_L(\lambda_L; t)$ is weighted more towards the high stretch side. On the other hand, $p(\lambda)$ is based on the probability of λ in the entire (two-dimensional) domain. As lines get stretched the width of the line is inversely proportional to the stretch experienced by that part of the line, so that the measure of the line remains constant, as does the stretch distribution $p(\lambda)$.

Figures 3.2 and 3.3 show plots of $p(\lambda)$ and $p_L(\lambda_L)$ for the same run which show a good match considering that they are for arbitrary initial conditions run for a relatively short time.

3.2.2 The importance of tails

Beigie [14, 12] demonstrated the significant role that non-Gaussian high stretch tails play in the evolution of lines by performing numerical experiments to compare the lengths of the portions of the interfacial line corresponding to the Gaussian component to those corresponding to the non-Gaussian component. It was found that the relative contribution due to the Gaussian statistics decreases exponentially with time. In this section we will generalize this concept to show the dominating role that non-Gaussian high stretch tails play in the *line* evolution.

As pointed out by Beigie [12], the high stretch tails are important because though they correspond to small integrated probability values, they play a significant role in interfacial line stretching and, for incompressible flows, high stretch statistics

correspond to thin striation widths so that they are important in the distribution of small scales.

As we showed in the previous section the stretch distributions on the interfacial lines favor the high stretch side with increasing t. And depending on whether $p(\lambda)$ is Gaussian or not, $p_L(\lambda_L;t)$ can have very different character. This is because for the Gaussian $p(\lambda)$, $p_L(\lambda_L;t)$ remains Gaussian and maintains the same variance, whereas for deviations from the Gaussian, the slope of $p_L(\lambda_L;t)$ keeps growing with t. And since the line width is related to the stretch distribution by $\delta \sim e^{-\lambda t}$, the effect on the makeup of the material line is clear.

For the case where $p(\lambda)$ is Gaussian

$$p(\lambda;t) = \frac{e^{-(\lambda-\langle\lambda\rangle)^2/2\sigma^2(t)}}{\sqrt{2\pi}\sigma(t)}. \tag{3.8}$$

Then using Eq. (3.6),

$$p(\lambda;t)e^{\lambda t} = \frac{e^{(2\sigma^2(t)\lambda t-(\lambda-\langle\lambda\rangle)^2)/2\sigma^2(t)}}{\sqrt{2\pi}\sigma(t)} \tag{3.9}$$

and the condition that

$$\int_{-\infty}^{\infty} p_L(\lambda_L)d\lambda_L = 1 \tag{3.10}$$

$$p(\lambda_L;t) = \frac{e^{-(\lambda-\hat{\mu}_L)^2/2\sigma^2}}{\sqrt{2\pi}\sigma(t)} \tag{3.11}$$

which is still a Gaussian with a different mean $\hat{\mu}_L = \langle\lambda\rangle + \sigma^2 t$, but the same variance $\sigma_L^2 = \sigma^2$. The PDF just gets shifted to the right (higher stretch values). For the case where $p(\lambda)$ is non-Gaussian, consider the following exponential PDF:

$$p(\lambda) = \frac{a}{2}e^{-a\lambda} \quad \text{for } \lambda > 0 \tag{3.12}$$

$$p(\lambda) = \frac{a}{2}e^{a\lambda} \quad \text{for } \lambda < 0\,. \tag{3.13}$$

Then

$$p_L(\lambda_L;t) = \frac{a^2-t^2}{2a}e^{(t-a)\lambda} \quad \text{for } \lambda > 0 \tag{3.14}$$

$$p_L(\lambda_L;t) = \frac{a^2-t^2}{2a}e^{(t+a)\lambda} \quad \text{for } \lambda < 0 \tag{3.15}$$

with $t < a$, which has the mean

$$\hat{\mu}_L = \int_{-\infty}^{\infty} p_L(\lambda_L)\lambda_L d\lambda_L = \frac{2t(a^2-t^2)}{(a-t)^2(a+t)^2}. \tag{3.16}$$

$$\sim \frac{1}{a-t} \quad \text{as } t \to a$$

which blows up in finite time as $t \to a$. The variance is

$$\sigma_L^2 = \int_{-\infty}^{\infty} p_L(\lambda_L)(\lambda_L - \hat{\mu}_L)^2 d\lambda_L = \frac{(a^2-t^2)[2a^3+6at^2-2a^4t+4a^2t^3-2t^5]}{a(a-t)^3(a+t)^3} \tag{3.17}$$

$$\sim \frac{1}{(a-t)^2} \quad \text{as } t \to a$$

which increases with t. This is due to the fact that the slope of the high stretch tail increases by $e^{\lambda t}$ and decreases by $e^{\lambda t}$ for the low stretch side as shown in Figures 3.4 and 3.5. Although the pure exponential function is rather an idealized situation, the trend of the non-Gaussian high stretch tails' increasing contribution to $p_L(\lambda_L)$ in contrast to a stationary $p_L(\lambda_L)$ for the Gaussian PDF is clear. This explains the growing dominance of non-Gaussian tails in the stretch distribution of interfacial lines.

3.2.3 Normalization schemes

Since $p(\lambda;t)$ varies with time, we ask whether $p(\lambda)$ can be renormalized to an invariant form independent of t as $t \to \infty$. Scaling is usually done in two ways — Beigie [14] has referred to these as horizontal and vertical scaling (see also [111]).

Horizontal scaling involves normalizing λ by

$$\lambda_n = \frac{\lambda - \langle\lambda\rangle}{\sigma(t)} \tag{3.18}$$

where $\langle\lambda(t)\rangle$ is the mean, and $\sigma^2(t)$ is the variance. This form of scaling is useful for examining the central, high probability regions of the distribution. Since we are normalizing with the variance which nominally decreases with t, this has the effect of zooming into the central region. So as t gets larger we tend to see narrower and narrower band around the central region, and thus the tendency towards Gaussian distributions.

Vertical scaling involves normalizing $p(\lambda)$ by

$$p_n(\lambda) = -\frac{1}{t}\log(p(\lambda)/\sqrt{t}). \tag{3.19}$$

This type of scaling often holds for temporally chaotic flows, and has the opposite effect of shrinking the tails in towards the central region as t increases.

We use both forms of scalings to track the evolution of $p(\lambda)$. We will show in Section 3.3 that there is a slow convergence to an invariant distribution for both scalings. This being the case, each can be used selectively to emphasize or view the high probability or low probability regions as needed. In what follows, normalization will imply horizontal normalization, unless stated otherwise.

3.3 Numerical results

Stretch statistics ranging from Gaussian to exponential were obtained by Beigie et al. [14] for near-integrable, chaotic two-vortex problems. The existence of non-Gaussian high stretch tails and the significance of their role in interfacial stretching were shown in that study. By varying N and δ, we study the types of stretch

statistics obtained in a more general setting of N vortex interactions. In particular, we find that the statistics range from Gaussian for vortices that overlap to strongly non-Gaussian for isolated vortices.

For flow around a *single* vortex, it is clear that the stretching is linear. This is because the flow direction is always tangential, and depends only on the distance r from the center. Therefore any line segment becomes aligned with this tangential flow direction, and after the initial r differences have been stretched out, there ceases to be any stretching, and after long enough time the Lyapunov exponent goes to zero. (It must be remembered however that, near the vortex, the velocity values tend to be much larger than farther away, so that the stretch rate due to the initial non-alignment will be large.)

For the case of *two* vortices, the situation does not change near the vortex, and the steady flow (in a translating or rotating frame of reference) in general prevents exponential line stretching. Fluid particles are either trapped by one or the other vortex, or by neither, and this status doesn't change over time. It is easy to see how the stretching properties are changed when external perturbation is introduced. It has the effect of realigning the line segments from time to time so that exponential line growth is possible. In the study by Rom-Kedar et al. [102] and Beigie et al. [14] a sinusoidal straining to a two-vortex system was externally introduced. For the present study, the perturbation to the motion of a passive particle around a vortex is provided by the other vortices when the number of vortices is greater than two. This provides us with a situation different from the near-integrable two-vortex problem in that the perturbation is of order one (far from integrable), and it is precisely the effect of this difference that we wish to explore.

There are three known constants of motion that are in involution with each other for the N vortex problem, so that the particle motion (the restricted problem) of a $N \geq 3$ system can have chaotic particle trajectories [2, 4, 87]. The chaotic nature of the Lagrangian particle trajectories and the stretching of material lines

are closely related. But a rigorous connection has not been found between the stretch statistics and what we know of the velocity field statistics. This is because stretching involves both spatial *and* temporal velocity variations. In what follows, we numerically examine several different cases involving the parameters N and δ.

We first concentrate on the stirring induced by three vortices as it represents the type of action typical of a small number of interacting vortices. Figure 3.6 shows a line that has been advected by the three vortices with $\delta = .1$. A blow-up of the region around one vortex is shown in Figure 3.7. One clear feature of this type of flow is the existence of an island around each vortex. The azimuthal flow near a vortex blob is given roughly by the Lorentzian profile ($\sim r/(r^2 + d^2)$) and the boundary between the chaotic region and the core region forms where the $1/r$ (tangential) velocity dependence due to a vortex is reduced sufficiently to be influenced by the effect of the other vortices. Using a fixed number of passive particles to track the flow for longer times, two more large islands are visible, as seen in Figure 3.8. It is possible that higher resolution computations may yield smaller island regions as well. The initial placement of the particles are chosen such that they lie in the 'chaotic' zone. Figures 3.9 and 3.10 shows the evolution of a group of points initially placed completely within one of the islands. The points do not move outside the island, and the statistics collected for these are quite different from those collected in the chaotic region, as we shall see below.

Figure 3.11 shows the PDF of the Lyapunov exponents obtained from the advection of the points in a simulation similar to those of Figure 3.8. Most of the λ values are positive, indicating the exponential stretch experienced by the particles through their trajectories. Figure 3.12 shows the horizontally-scaled log-plot of $p(\lambda_n)$. There are deviations from a Gaussian PDF that has the same mean and variance. This shape appears to be generic for the class of problems that we study here, with the maximum value being different from the mean, always on the low stretch side. The high stretch tails tend somewhat towards the exponential, (although not quite) and

have higher probability values than the Gaussian, while the low stretch tail tends to dip below it. In applying the vertical scaling at various times, we see a slow convergence towards an invariant function $p_n(\lambda)$ as shown in Figure 3.13. For the distribution of λ obtained from an interfacial line, the results are similar, but sharper (more non-Gaussian) due to the fact that line simulations are run for much shorter times.

The PDF associated with the particles confined in the island of Figure 3.9 and 3.10, is shown in Figure 3.14, and it is clearly quite different in shape and value from the PDF of the chaotic region. Most notably, about half of the probability values are in the negative λ region (with more expected for increasing t).

In comparing the results of the three-vortex problem to the perturbed two-vortex problem of Beigie [12] we observe that in that study the statistics were collected from a part of the unstable manifold only, while the results presented so far in this study have been for the entire ergodic region. (The distinction could be important, because the stretch statistics depend strongly on how the stretchings are spatially distributed, and how different stretching values are "shared" over the finite time t.) Because of the 'template' property of the unstable manifold, a line segment that is advected by the flow eventually follows the unstable manifold quite closely. See Beigie [12] or Beigie et al. [15] for a thorough exposition, especially pertaining to situations where the system is aperiodic. Non-periodic flows are no longer amenable to simplified analyses involving Poincaré sections, but the unstable manifolds are nonetheless present and dominate the topology of the flow. In the present three-vortex problem we find that stable and unstable manifolds exist and determine the stretching of line elements in the flow. The problem is best thought of as a three-dimensional problem, with the third dimension being time; the manifolds are two-dimensional sheets and the invariant hyperbolic set is a one-dimensional line. The location and shape of these structures are determined by the vortices, and therefore follow them in a Lagrangian manner as they wind about. In Figure 3.15 we show

the evolution of an unstable manifold emanating from a hyperbolic set between two vortices. The geometry of the lines shown in Figure 3.6 is clearly similar to the unstable manifold shown in Figure 3.15. As discussed in Section 3.2.2, $p(\lambda)$ can also be obtained from the line stretching simulations such as shown in Figure 3.6 by the formula $p(\lambda) = p_L(\lambda_L)e^{-\lambda t}$. This is shown in Figure 3.16 where we see the characteristic non-Gaussian features we discussed earlier — we note that the features are sharper here.

The core parameter δ plays the role of distributing the vorticity more uniformly. So for large values of δ such that there is an overlap of the vortex blobs, the islands around the vortices disappear, and the stretch statistics become closer to Gaussian. The advected lines and points are displayed in Figures 3.17, 3.18, and 3.19 with the corresponding stretch statistics shown in Figures 3.20 and 3.21. In comparison to the $\delta = .02$ or $\delta = .1$ cases, $p(\lambda)$ for $\delta = 1.0$ is more or less Gaussian.

We turn now to flows with a relatively larger number ($N \sim$O(100)) of vortices. Figure 3.22 shows a line segment that has been stretched by the action of $N = 150$ vortices, with $\delta = 0.1$. Figure 3.23 shows a similar vortex configuration advecting a fixed number of passive particles (after long times). The horizontally-scaled stretch statistics from this simulation is shown compared to a Gaussian curve in Figure 3.24. As the core parameter δ is varied we observe a similar trend as in the three-vortex case; namely the statistics moving progressively away from Gaussian as the vortex cores get more and more isolated from each other. This is similar to the findings in Chapter 2 for the Eulerian velocity statistics, and it is also useful to refer back to the vorticity distribution plots shown in Figures 1.1-1.4. See Figures 3.25 and 3.26 for the line distribution and PDF for $\delta = .5$.

For both the large and small N cases, the non-Gaussian stretch distribution is due to the slow transport of particles between two distinct regions of the flow (note: we are not concerned with the islands here). The slow and fast regions are created because the *vortices* are confined to a smaller region than the *passive*

particles, as seen in Figure 3.23. Numerically, the outer bounds of the vortex and passive particle motion appear stable, for the time scales considered. However, their absolute boundedness is still an open question (except for that imposed by the invariants of motion). If the statistics were collected from within the well-stirred inner region only (i.e. the region that is 'swept' by the vortices), the stretch can be considered Gaussian for larger values of δ. However, the ergodic region (in the two-dimensional physical space for the passive particles) extends beyond this well-stirred region and consists of a larger, outer region. The reason for the poor stretching in the outer region is because the fluctuations due to the vortex interactions die out quickly with r ($\sim e^{-r^2}$, see section 2.6.1 in chapter 2). This, and the fact that the mean velocity in the outer region is also decaying with r, keeps the statistics from being collected from a randomly mixed set. For large values of δ, the vorticity is better distributed, so that the velocities in the inner region are not much greater than that in the outer region. This results in a much more uniform sharing of the stretch values by the particles, and hence the trend towards Gaussian statistics.

In comparison to the closed oscillating vortex pair (OVP) problem [14], the underlying mechanism of non-uniform stretchings being the cause of non-Gaussian PDF is the same, but the details are different. In the closed OVP flow, there were some isolated points that were continually exposed to very strong stretches (due to isolated intersections with the stable manifold and hence being brought towards the hyperbolic point). In the current case, the non-uniform stretchings arise from the fact that particles (or line segments) are located in two distinct regions that are open for transport, but over a long time scale. In fact, for the $N = 150$ case, the inter-region transport time is so long compared to the 'mixing' time within the regions, that non-Gaussian PDF is evident even under horizontal scaling. For small N, the transport between regions is much less marked, and the non-Gaussian components disappear under horizontal scaling. There is another point of comparison to this phenomena, and that is the evidence of sharp peaks in the PDF of finite time Lyapunov exponents for two-dimensional chaotic flows that have KAM tori. The

'stickiness' of the tori ensures that a small group of particles experience stretching that is quite different from that of the rest of the ergodic region.

3.4 Discussion

To summarize the findings of the previous section, the distribution of finite-time Lyapunov exponents in the N-vortex flows range from Gaussian to strongly non-Gaussian depending on the parameter values. The PDF $p(\lambda)$ has a characteristic non-Gaussian shape for small δ and approaches the Gaussian distribution as δ increases. The 'smallness' of δ is of course scaled with respect to the inter-vortex distance. The non-Gaussian statistics are caused by the non-uniform sampling of stretching by the particles, which is due to the sufficiently slow transport between the fast-stirred inner region and the slow-stirred outer region.

3.4.1 Multinomial multiplicative process model

We now present a model that illustrates the mechanism responsible for the data presented in the previous section. Beigie [12] has previously examined the binomial and trinomial multiplicative process in an attempt to demonstrate the exponential high stretch tails of the stretch distributions of chaotic tangles in perturbed two vortex systems. The so called open flow (two vortices of the opposite sign that are perturbed) produces stretch statistics that are Gaussian, while the closed flow (perturbed two vortices of the same sign that are perturbed) produces non-Gaussian high stretch tails. These models did not exactly duplicate the closed flow PDF, but served their purpose in illustrating the mechanism that lead to high stretch (nearly exponential) tails (which is caused by the non-uniform distribution of the stretches).

We develop a generalized version of this model and use it to illustrate the stretching mechanism that occurs in the N-vortex systems. The model is constructed as

follows: An initial domain extending from 0 to 1 is sectioned into m segments, each of width α_i, and each segment is stretched by an amount $1/\alpha_i$. Each of the resulting segments is then sectioned into m new segments, and the process is repeated for the second step, etc. Using the generalized Bernoulli trials [94], at the nth step the set of stretches are

$$\{\prod_{i=1}^{m} \alpha_i^{-k_i};\ k_i \in [0,n],\ i \in [1,m],\ \sum_{i=1}^{m} k_i = n\} \tag{3.20}$$

with each of these stretches having a PDF of

$$p(\mathbf{k}) \ \propto \ \frac{n!}{\prod_{i=1}^{m}(k_i)!} \prod_{i=1}^{m} \ \alpha_i^{k_i} \tag{3.21}$$

where $\mathbf{k}$ refers to any particular configuration of k_i's such that $\sum_{i=1}^{m} k_i = n$. There are M of these different stretches at any n,

$$M = \prod_{i=1}^{m-1} \frac{(n+i)}{i} = \frac{(n+m-1)!}{(m-1)!n!} \ . \tag{3.22}$$

The stretch exponent λ associated with each of these stretches are

$$\lambda_{k_1,k_2,\ldots,k_m} = \ \frac{1}{n}\log[\prod_{i=1}^{m} \alpha_i^{-k_i}] \ = \ \frac{1}{n}\sum_{i=1}^{m} -k_i \log \alpha_i \ ; \tag{3.23}$$

$$k_i \in [0,n] \ \ , \ \ \sum_{i=1}^{m} k_i = n \ . \tag{3.24}$$

Using Stirling's formula, as $n \to \infty$

$$\frac{1}{n}\log p(\mathbf{k}) \approx \log(n) - 1 + \frac{1}{n}\sum_{i=1}^{m}[k_i \log \alpha_i - (1/2 + k_i)\log k_i + k_i] \ , \tag{3.25}$$

and

$$\frac{1}{n}\log p(k) \sim \sum_{\lambda(\mathbf{k})=\lambda(k)}^{\mathbf{k}} \frac{\log p(\mathbf{k})}{n} \ . \tag{3.26}$$

For the $m = 2$ (two-stretch) system, it is easy to show that under the horizontal scaling the $p(\lambda)$ approaches the Gaussian distribution as shown by Farmer et al. [39]

for the baker's transformation. On the other hand, vertical scaling has the effect of driving λ to the fringes (away from $\lambda = \langle\lambda\rangle$), and so deviates from Gaussian. Therefore, depending on whether the interest is on the PDF of the Lyapunov exponents over the entire domain, or just along an interfacial line, different results are possible.

We numerically compute a few cases with $m = 5$ to demonstrate the range of behavior that is possible with this model. Figure 3.27 shows $p(\lambda)$ from a system with a wide range of stretches (see caption for the parameters). The deviation from Gaussian is evident, but the most significant feature is the similarity to the result from the three-vortex system simulation. This illustrates the quite general form of the PDF seen in the previous section. The trend for increasing t, of slow convergence to a time-invariant curve is shown in Figures 3.28 and 3.29. For a system with a much more narrow range of stretches, the results approach Gaussian, as expected (see Figure 3.30).

The purpose of bringing in the extra stretchings in the multiplicative model is to match the general behavior of complex systems in which there is almost always many different stretches that are simultaneously applied to different parts of the flow, and to show that they do not always mix uniformly to produce Gaussian statistics. And in particular, the PDFs we have computed for the N-vortex flow can be explained in terms of this many-stretch system — and that non-Gaussian tails especially can exist for arbitrarily long times.

3.4.2 Gaussian and non-Gaussian stretch statistics

In this section we analyze the finite-time Lyapunov exponent distribution in terms of the local, instantaneous stretch rates and explain the different types of statistics we see in our numerical studies.

Line stretching is a multiplicative processes so it is natural to expect log-normal

statistics of $\delta l(t)/\delta l(0)$ (or normal for the exponent λ), depending on certain conditions. The conditions for the existence of Gaussian stretch statistics can be constructed as follows: Let

$$\mu(\mathbf{x}(t), dt) \equiv \log\left(\frac{\delta l(dt)}{\delta l(0)}\right) \tag{3.27}$$

represent the instantaneous stretch at some position $\mathbf{x}$, at time t. The line segment length after time dt is evaluated by

$$|\delta l_i(dt)| = \left|\frac{\partial u_i}{\partial x_j}\delta l_j(0)\right| dt. \tag{3.28}$$

Note that the stretch $\frac{\delta l(dt)}{\delta l(0)}$ depends on the velocity gradient tensor as well as the alignment of the line segment vector $|\delta l_j(0)|$ with respect to the velocity gradient tensor at that particular location and time. This means the previous history may be important for this instantaneous quantity as well. The average of the instantaneous stretchings experienced during the Lagrangian trajectory of a passive fluid particle forms the Lyapunov exponent

$$\lambda \equiv \frac{1}{ndt}\sum_{i=1}^{n}\mu(\mathbf{x}(t), dt). \tag{3.29}$$

If we consider the instantaneous local stretching as a random process, then there is a probability density function (PDF) $p_\mu(\mu)$ associated with an ensemble of particles. Furthermore, if $p_\mu(\mu)$ has a mean and a variance, and the μ's are random and independent, then by the central limit theorem, $p(\lambda)$ for this ensemble will be normally distributed. It is clear that much depends on how the local stretch statistics are sampled as the fluid particle makes its Lagrangian trajectory, and it is difficult to know *a priori* exactly under what conditions the fluid motion will be sufficiently mixing to produce normal stretch statistics.

As a means of demonstrating the above mentioned decomposition, the PDF $p_\mu(\mu)$ of the instantaneous stretch distribution μ, for several different parameter values are shown in Figures 3.31, 3.32, 3.33, and 3.34. The particle are initially sufficiently

stirred to the point of uniform spatial distribution. Note that the distribution of $p_\mu(\mu)$ can range from nearly power-law, to a flat constant. It is the shape of these distributions, as well as how randomly these plots are sampled through a particle's trajectory that determines the resulting $p(\lambda)$.

A possible simplification in the evaluation of Eq. (3.28) is that $\delta l_j(dt)$ and $\frac{\partial u_i}{\partial x_j}$ are independent and random. While it is reasonable to assume that the tensor $\frac{\partial u_i}{\partial x_j}$ has a stationary distribution (since the vortices are statistically stationary), the orientation of the $\delta l_j(dt)$ vector depends on the degree of persistence of the strain tensor, and is therefore not independent of it. This dependence of the orientation of the vector $\delta l_j(dt)$ on the gradient tensor is shown in the comparisons of $p_\mu(\mu)$ computed for initially uniform orientations evaluated at short times ($t = 5$ or 10). and after the vectors have been allowed to be directed by the flow for long times. As seen in some of the plots presented above, it is seen that the random approximation for the orientation of $\delta(0)$ is justified for some cases, but not for others. Thus, the wide array of possibilities for the stretch distribution are such that we are thwarted in applying even the simplest of approximations.

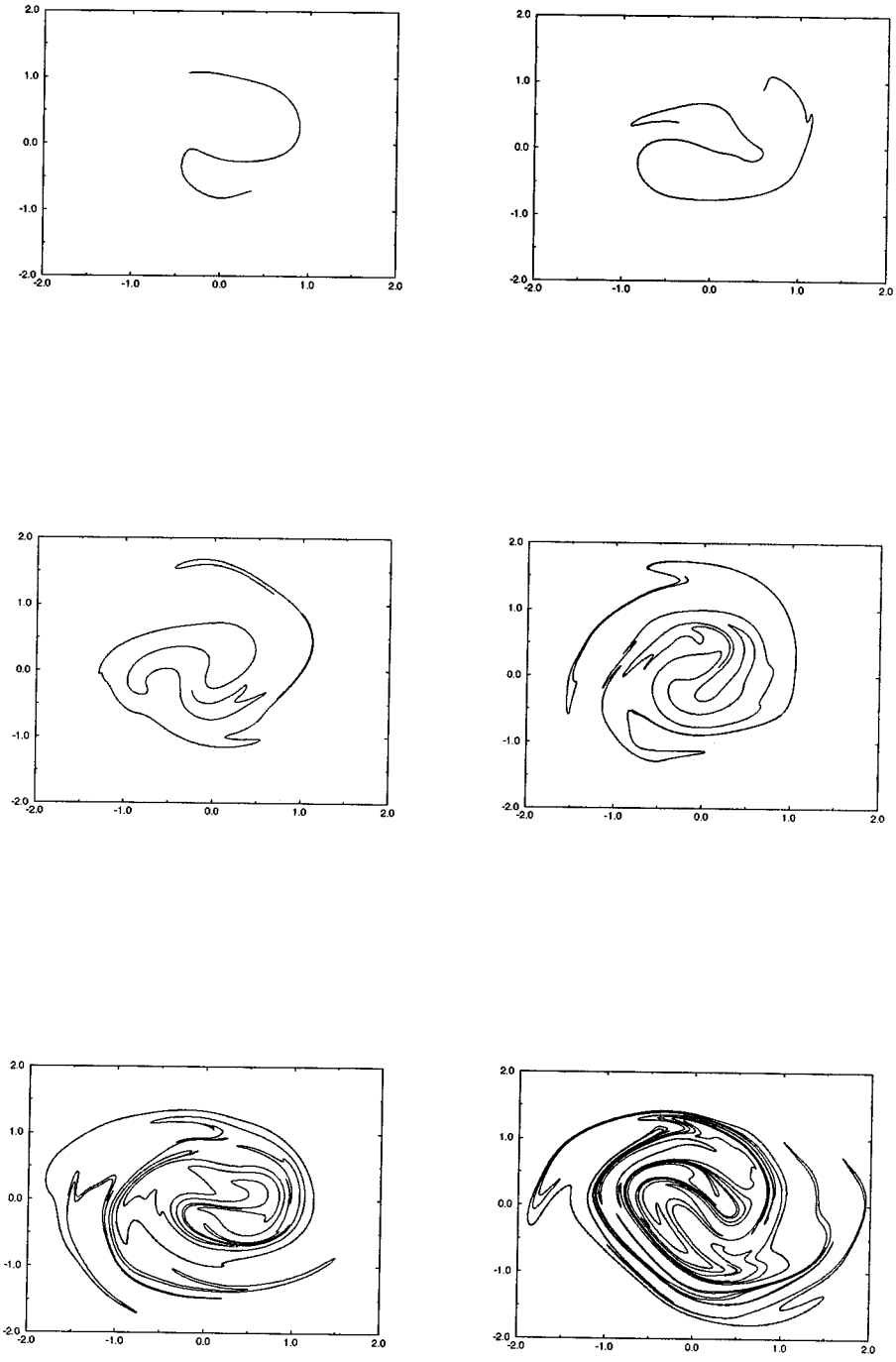

Figure 3.1: Sequence of line evolution due to stirring by N-vortices for $N = 150$, $\delta = .5$ at $t = 100, 200, 300, 400, 500$ and 600 (a),(b),(c),(d),(e),(f) left to right from top

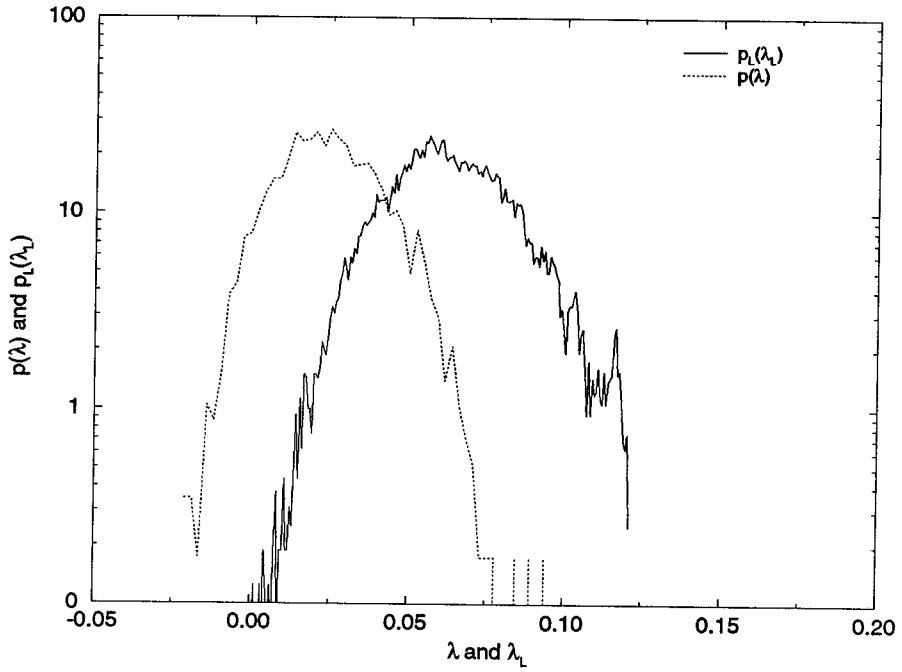

Figure 3.2: Comparison of $p(\lambda)$ and $p_L(\lambda_L)$ at $t = 120$ for $N = 150,\ \delta = .1$

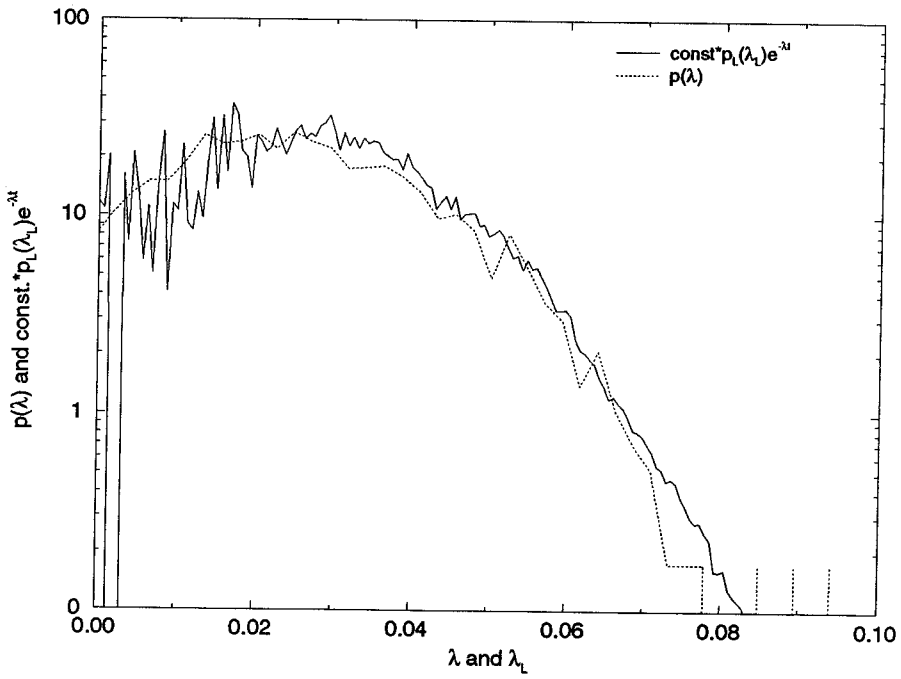

Figure 3.3: Comparison of $p(\lambda)$ and $p(\lambda_L)e^{-\lambda t}/\int p(\lambda;t)e^{-\lambda t}dt$ at $t = 120$ for $N = 150,\ \delta = .1$

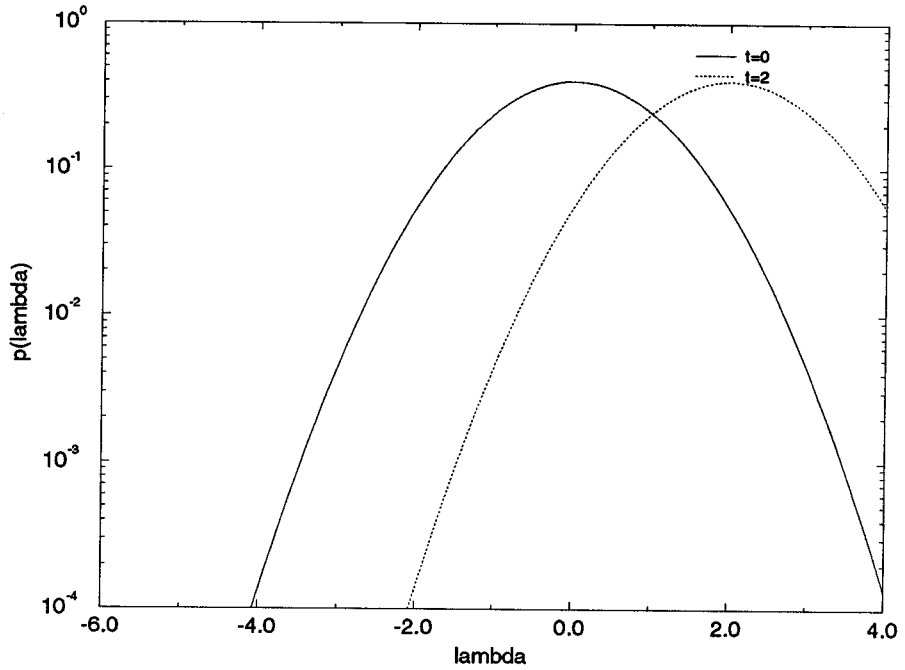

Figure 3.4: Comparison of $p_L(\lambda_L; 0)$ and $p_L(\lambda_L; t)$ for Gaussian tails

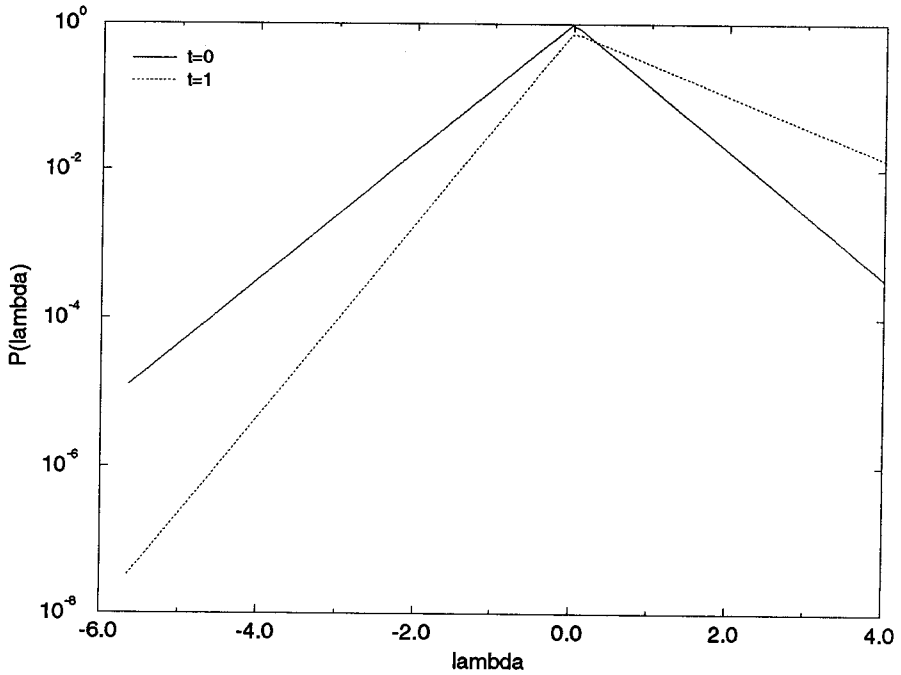

Figure 3.5: Comparison of $p_L(\lambda_L; 0)$ and $p_L(\lambda_L; t)$ for exponential tails

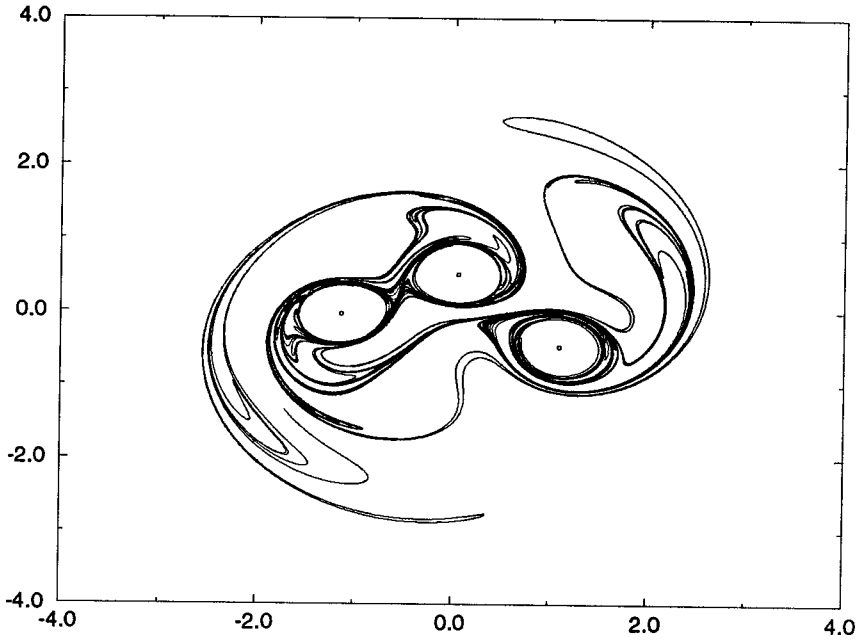

Figure 3.6: Line stirred by N-vortices, for $N = 3,\ \delta = .1$

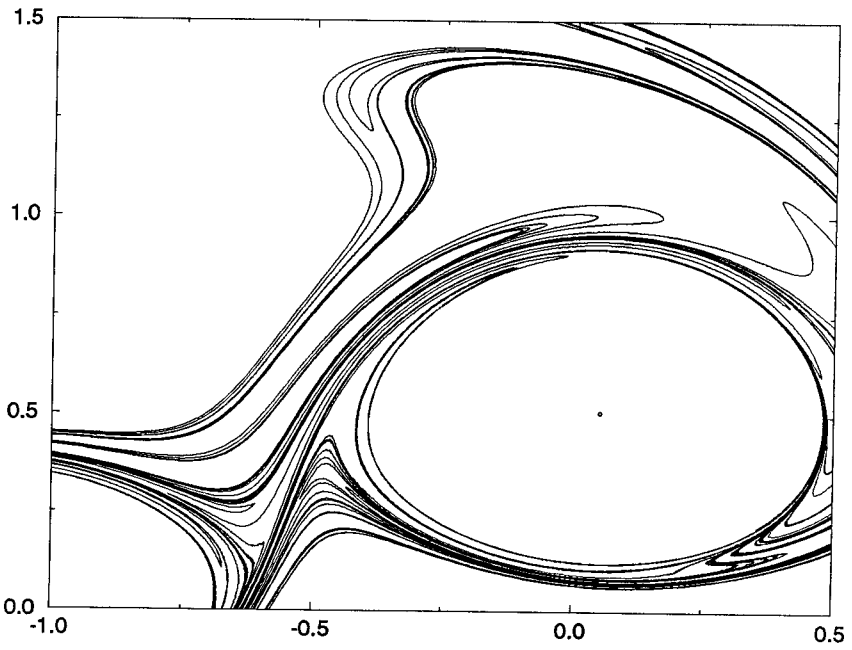

Figure 3.7: Line stirred by N-vortices, for $N = 3,\ \delta = .1$ (detail)

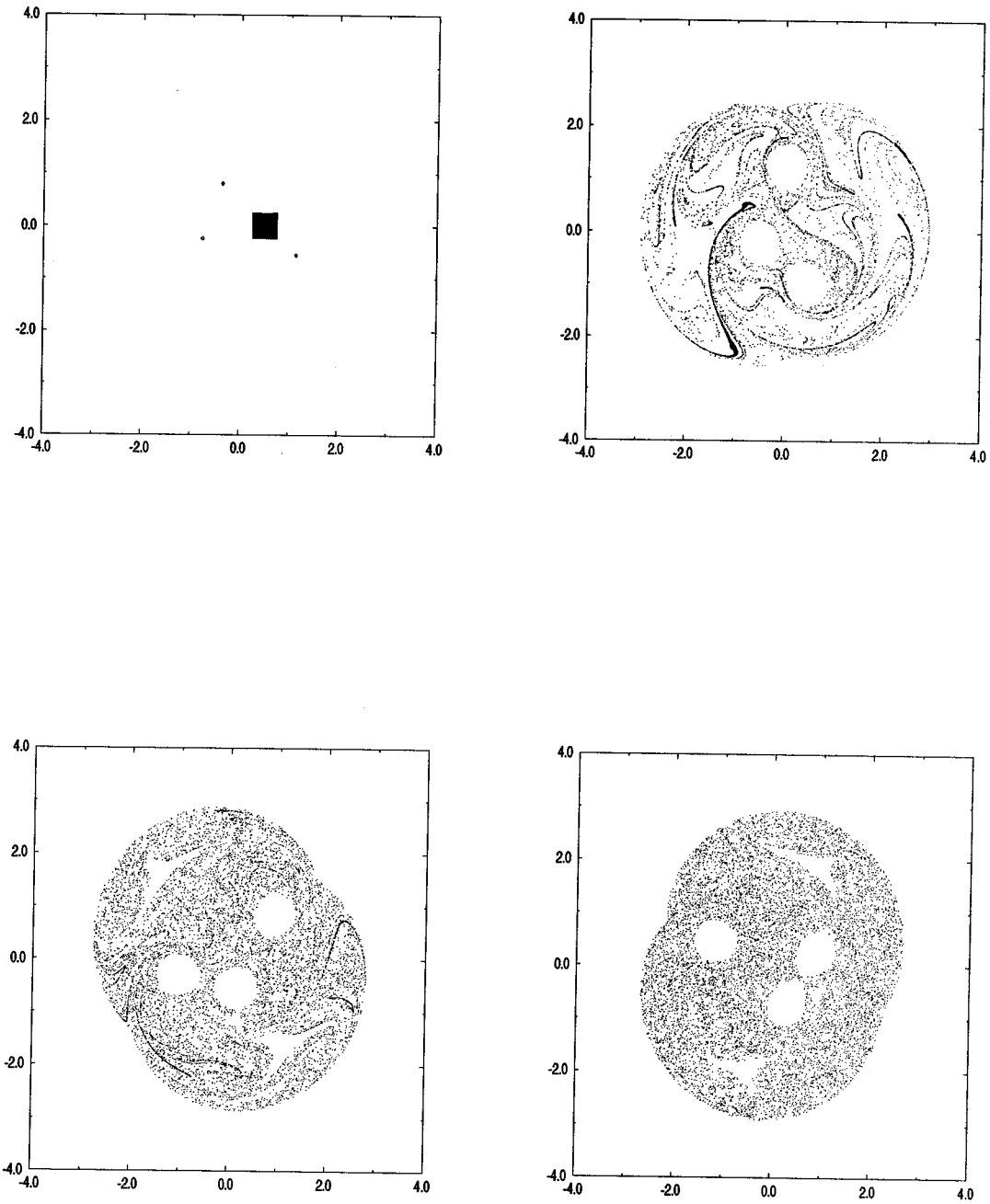

Figure 3.8: Sequence of particles stirred by N-vortices for $N = 3$, $\delta = .1$ at $t = 0, 500, 1000$, and 1500 (a),(b),(c),(d) left to right from top

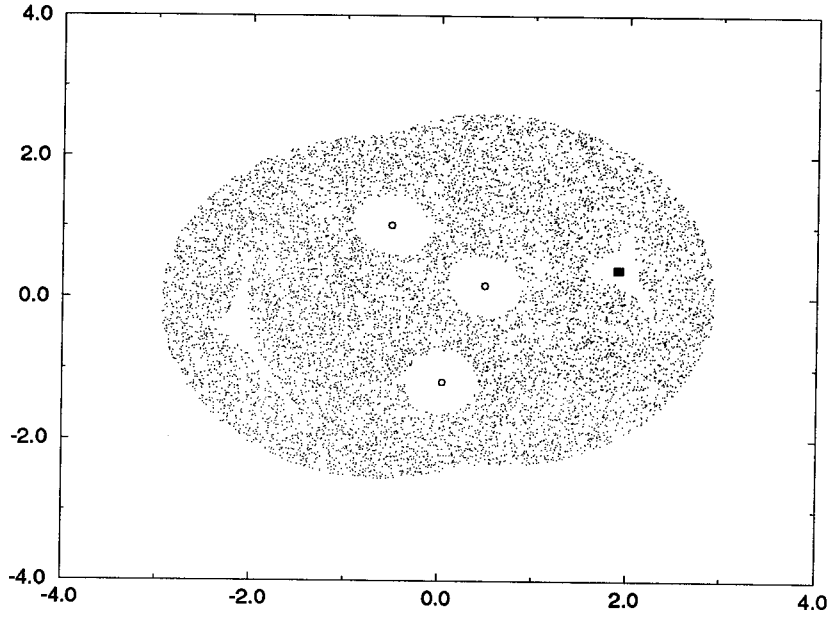

Figure 3.9: Particles within an island in the N-vortex system for $N = 3$, $\delta = .1$ at $t = 0$

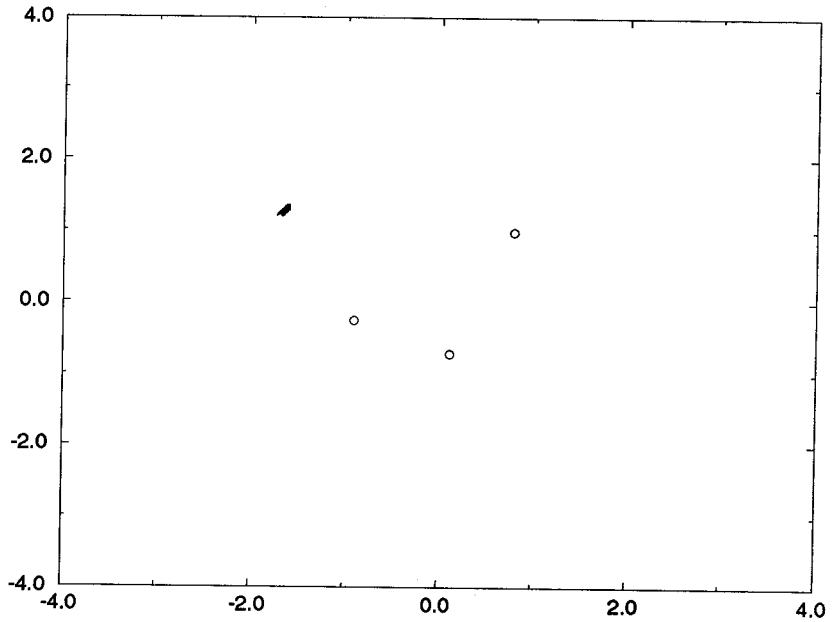

Figure 3.10: Particles within an island in the N-vortex system for $N = 3$, $\delta = .1$ at $t = 1000$

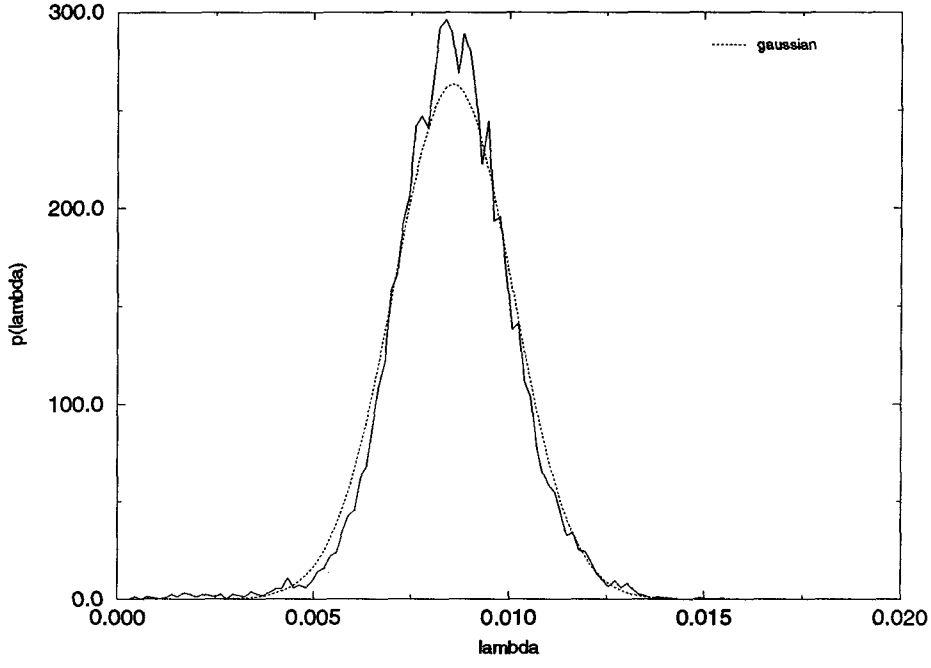

Figure 3.11: PDF $p(\lambda)$ vs λ compared to Gaussian curve for $N = 3,\ \delta = .02$

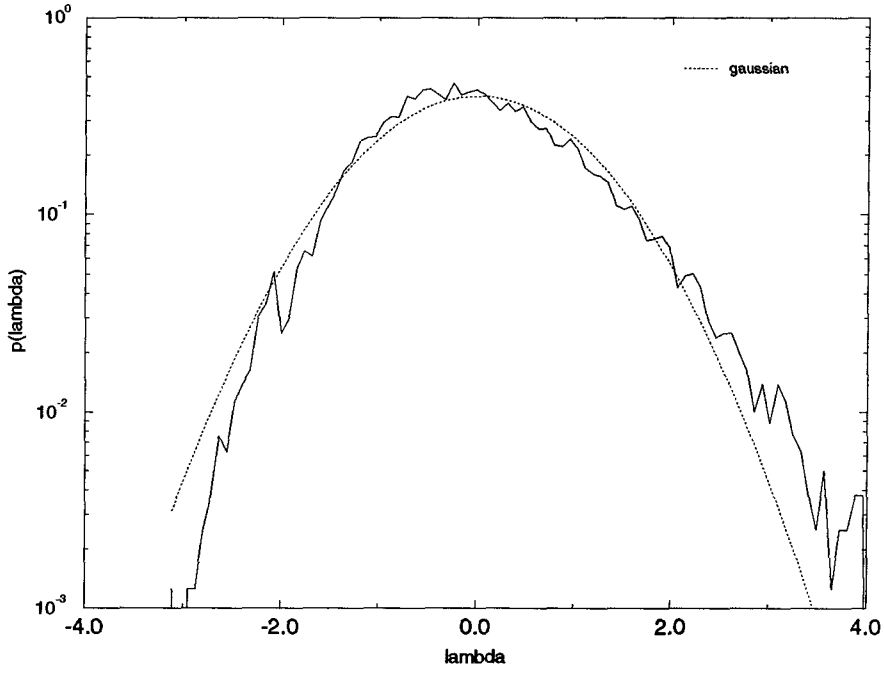

Figure 3.12: Normalized PDF $p(\lambda_n)$ vs λ_n compared with a Gaussian curve for $N = 3,\ \delta = .02$

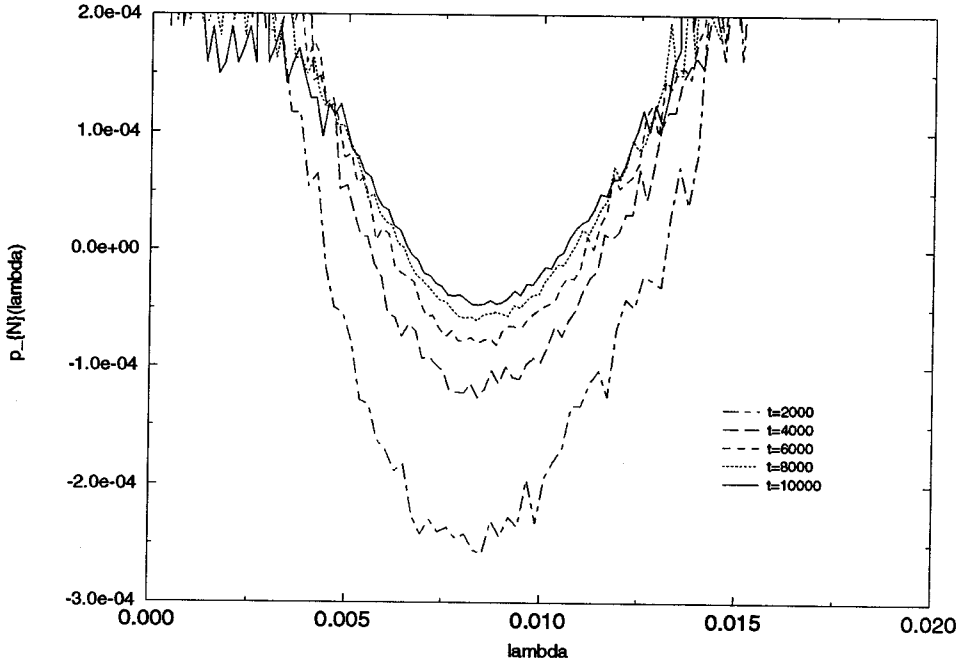

Figure 3.13: Vertically normalized PDF $p_n(\lambda)$ vs λ for $N = 3,\ \delta = .02$

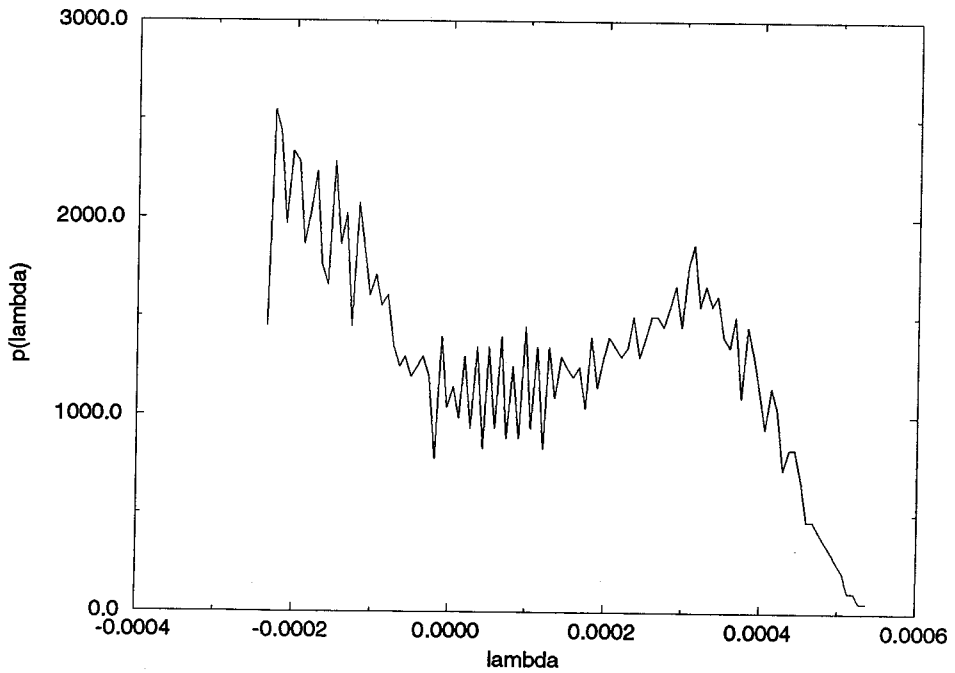

Figure 3.14: PDF $p_n(\lambda_n)$ vs λ_n for $N = 3,\ \delta = .1$ for particles within the islands

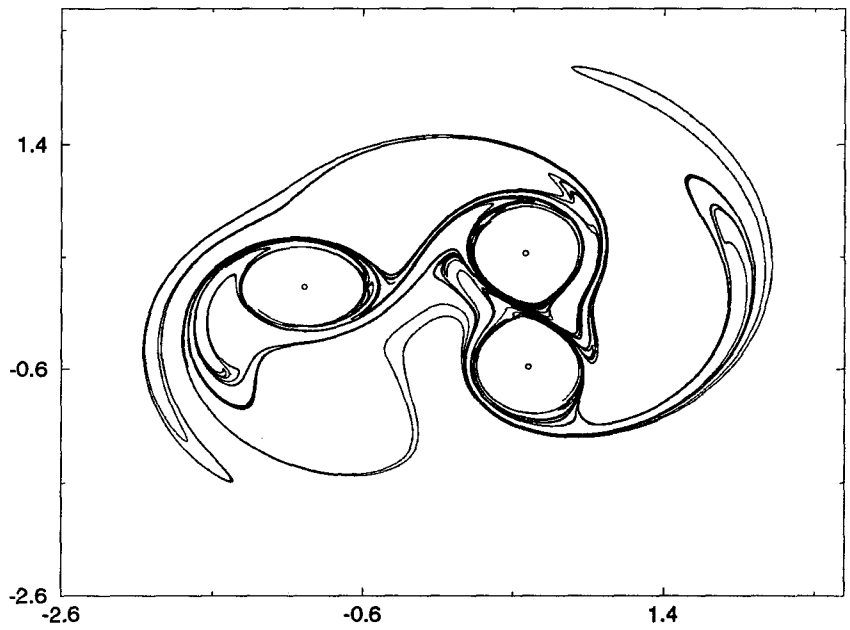

Figure 3.15: A segment of the unstable manifold for $N = 3,\ \delta = .1$

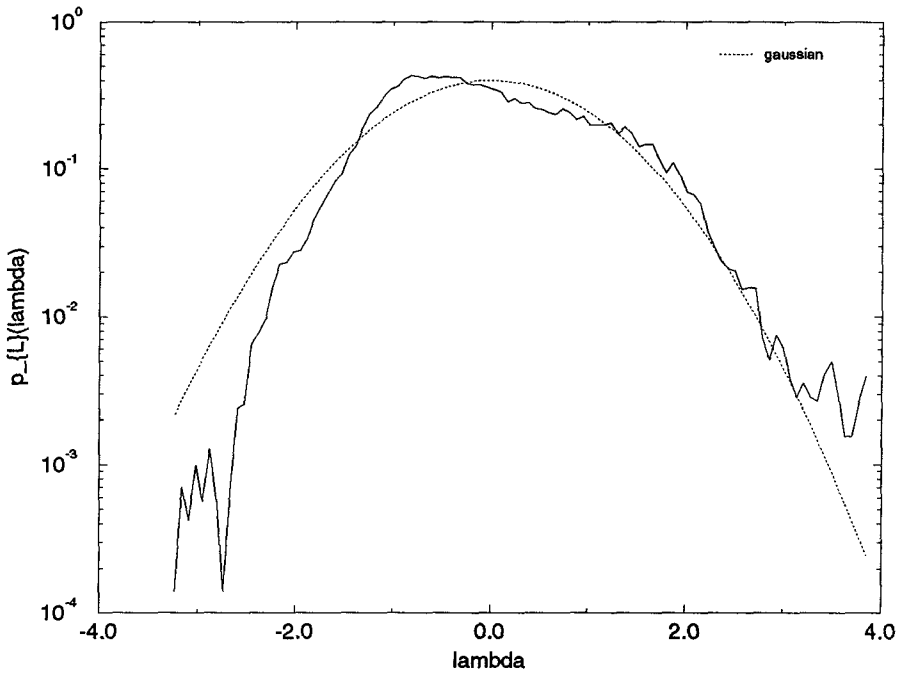

Figure 3.16: PDF $p_L(\lambda_L)$ vs λ_L for the segment of the unstable manifold for $N = 3,\ \delta = .1$

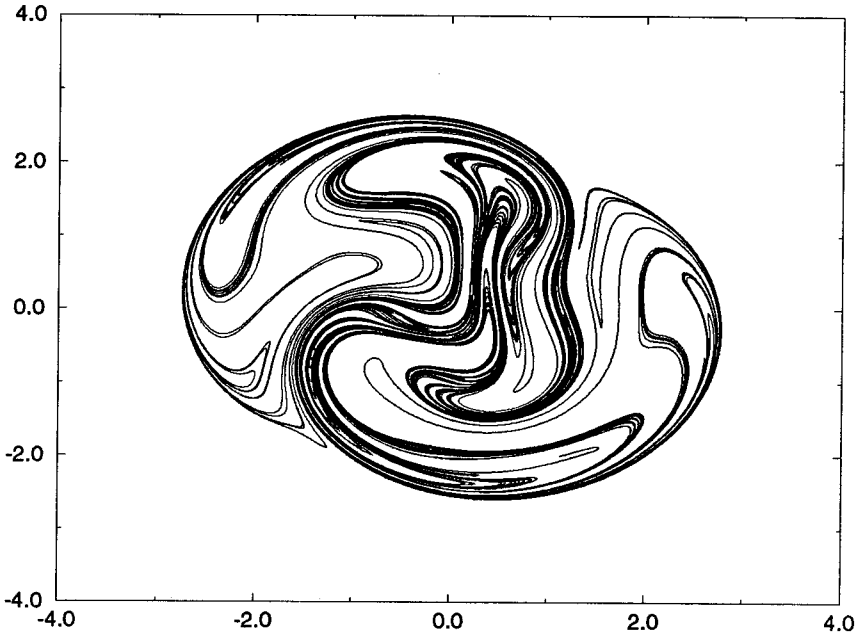

Figure 3.17: Line stirred by N-vortices for $N = 3,\ \delta = 1.0$

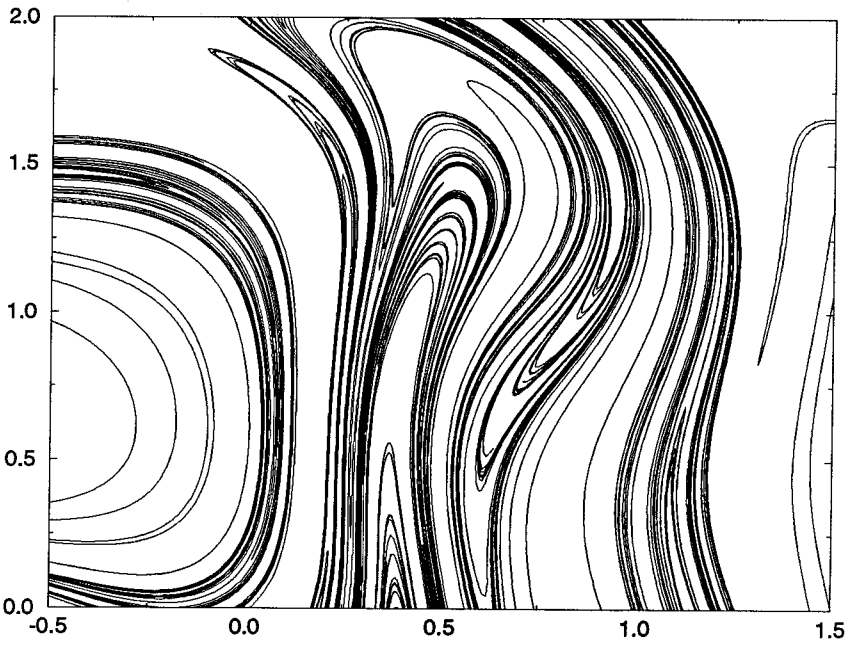

Figure 3.18: Line stirred by N-vortices for $N = 3,\ \delta = 1.0$ (detail)

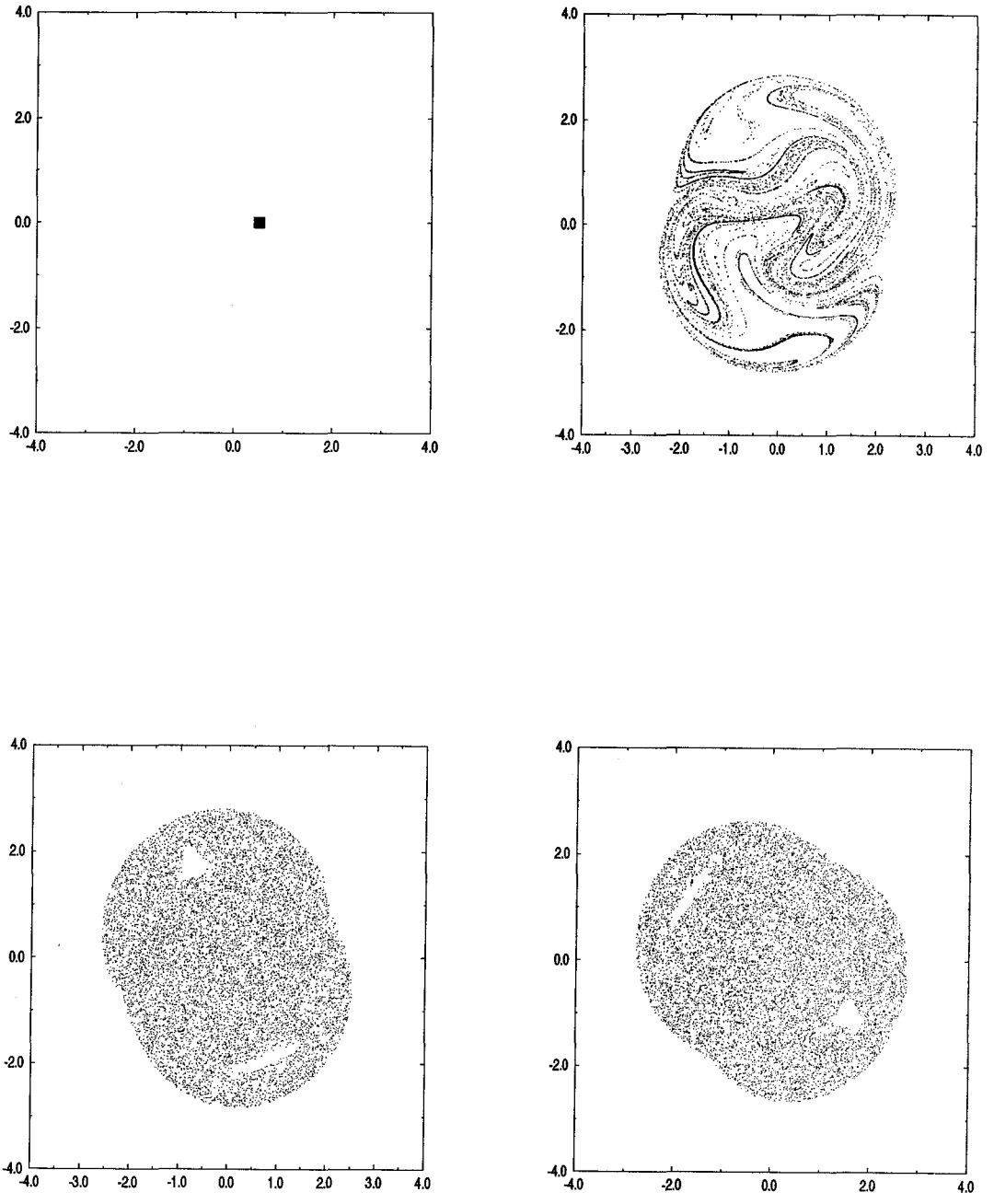

Figure 3.19: Sequence of particles stirred by N-vortices for $N = 3$, $\delta = 1.0$ at $t = 0, 1000, 3000, 5000$ (a),(b),(c),(d) left to right from top

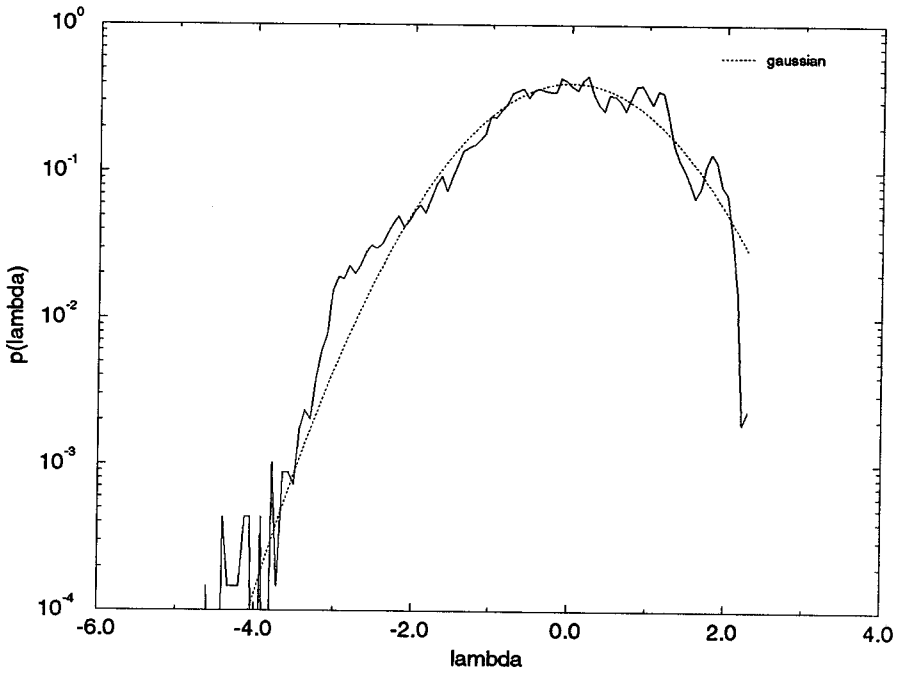

Figure 3.20: Normalized PDF $p_L(\lambda_L)$ along interfacial line for $N = 3, \delta = 1.0$

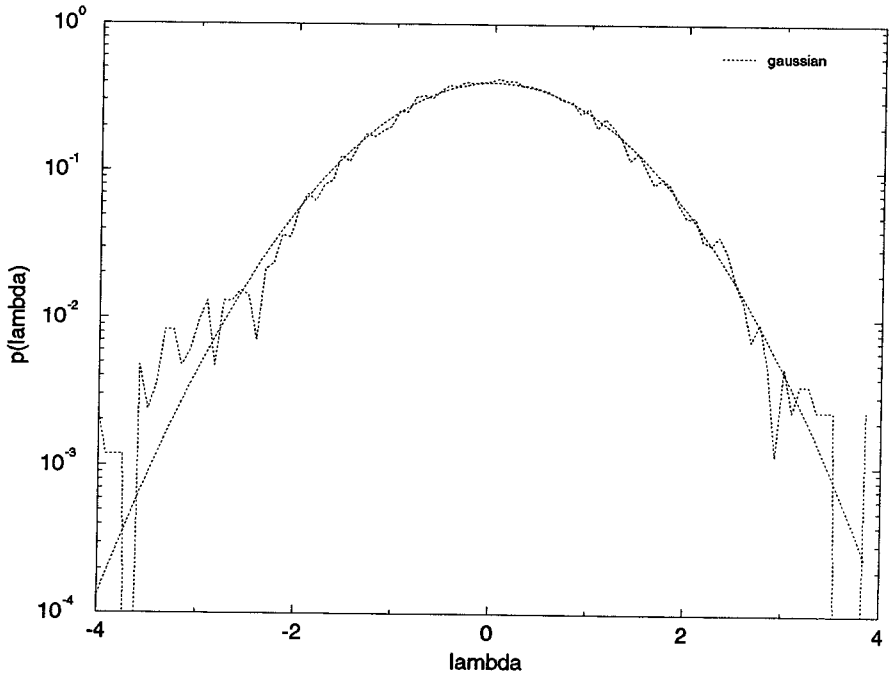

Figure 3.21: Normalized PDF $p(\lambda)$ from particles for $N = 3,\ \delta = 1.0$

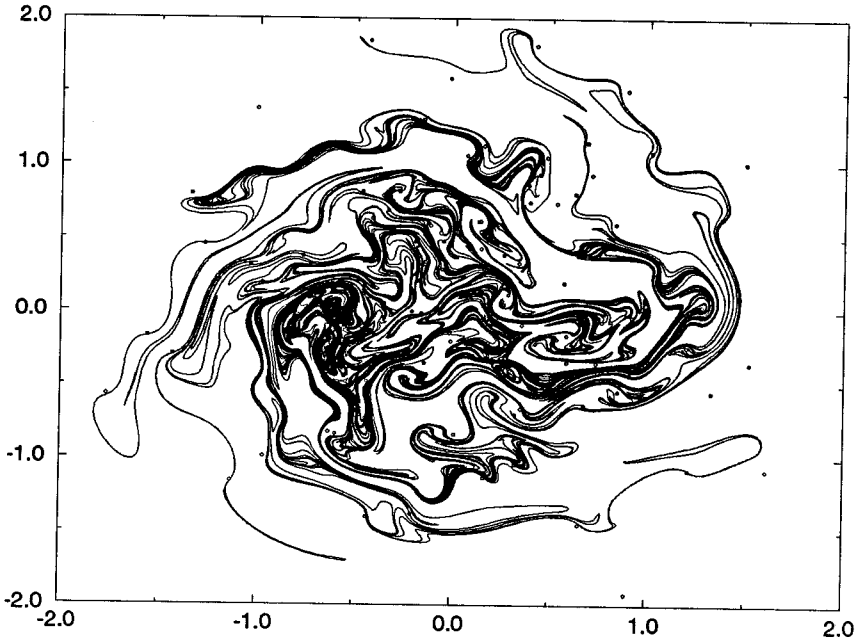

Figure 3.22: Line stirred by N-vortices for $N = 150,\ \delta = .1$

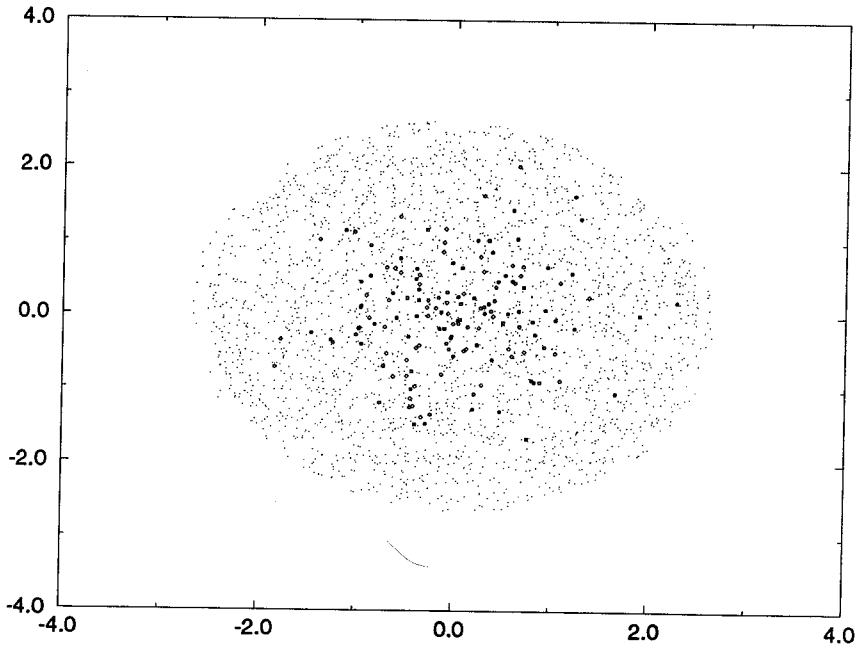

Figure 3.23: Particles stirred by N-vortices for $N = 150,\ \delta = .1$ (particles are shown by dots and vortices by circles)

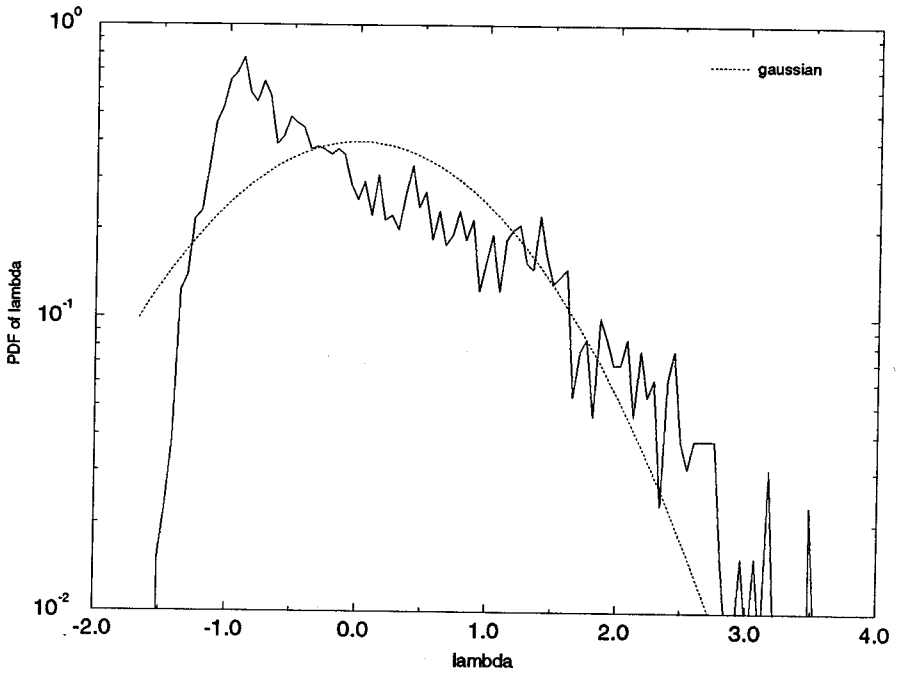

Figure 3.24: Normalized PDF $p(\lambda)$ vs λ from particles stirred by N-vortices for $N = 150, \delta = .1$

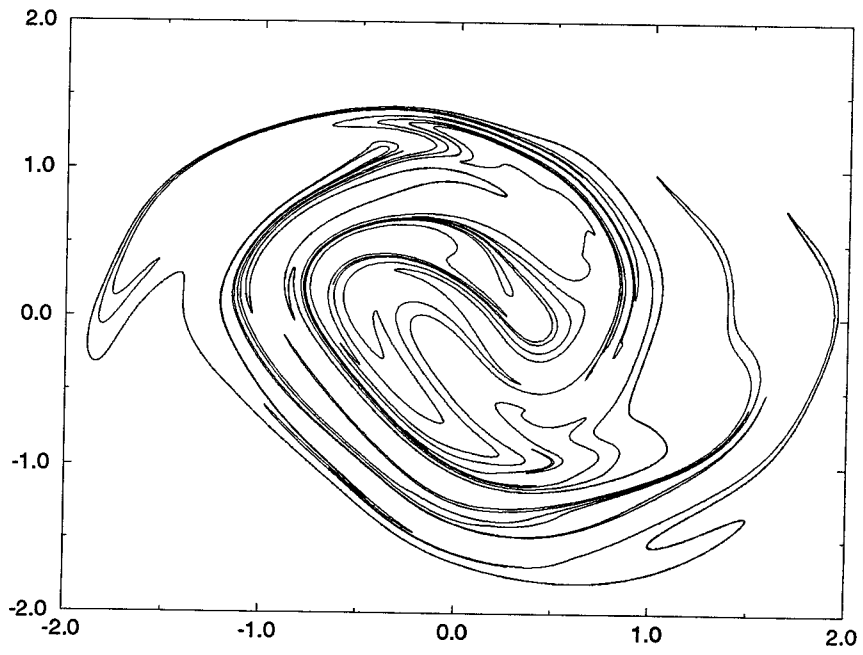

Figure 3.25: Line stirred by N-vortices for $N = 150,\ \delta = .5$

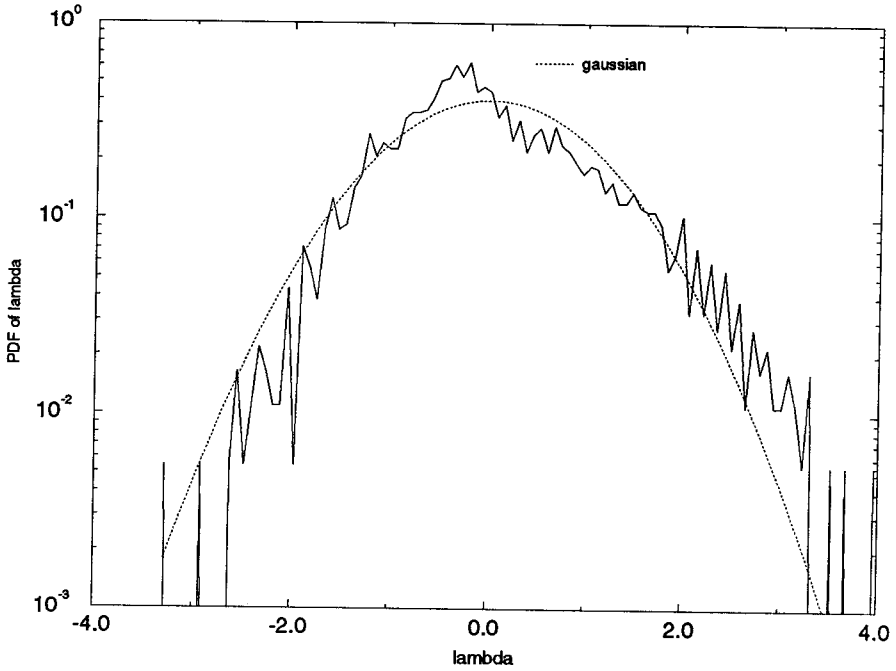

Figure 3.26: Normalized PDF $p(\lambda)$ vs λ from particle evolution for $N = 150,\ \delta = .5$

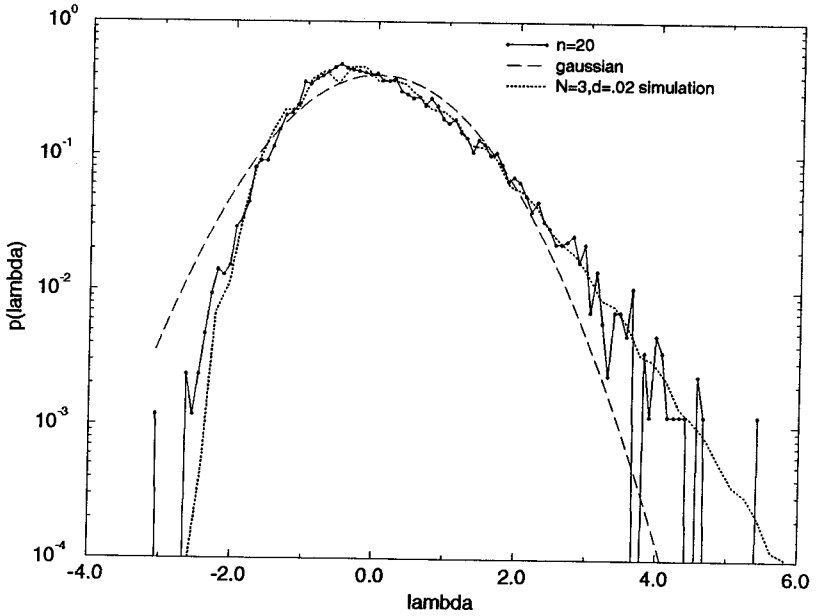

Figure 3.27: Normalized PDF for 5-nomial stretch model at $n = 20 \quad \alpha_1 = .01, \alpha_2 = .1, \alpha_3 = .2, \alpha_4 = .3, \alpha_5 = .39$

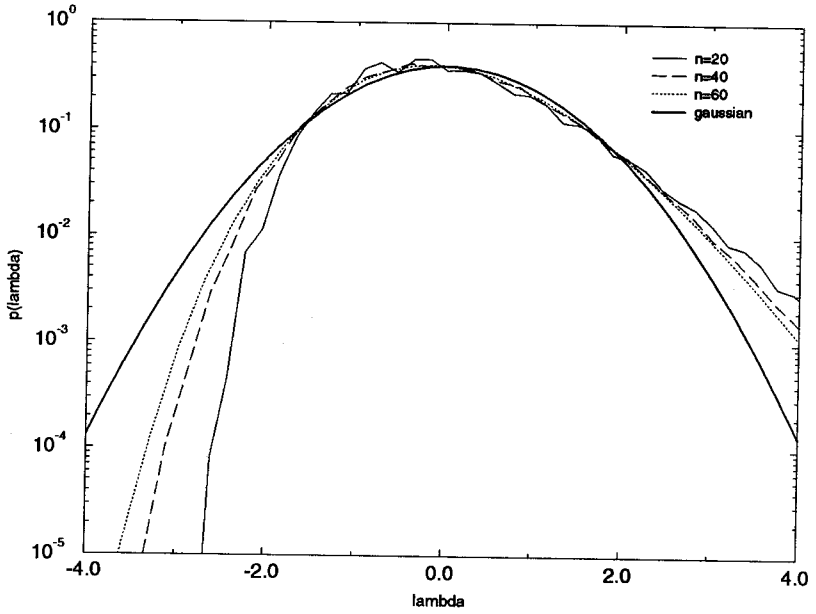

Figure 3.28: Normalized PDF $p(\lambda)$ vs λ for 5-nomial stretch model, $\alpha_1 = .01, \alpha_2 = .1, \alpha_3 = .2, \alpha_4 = .3, \alpha_5 = .39$

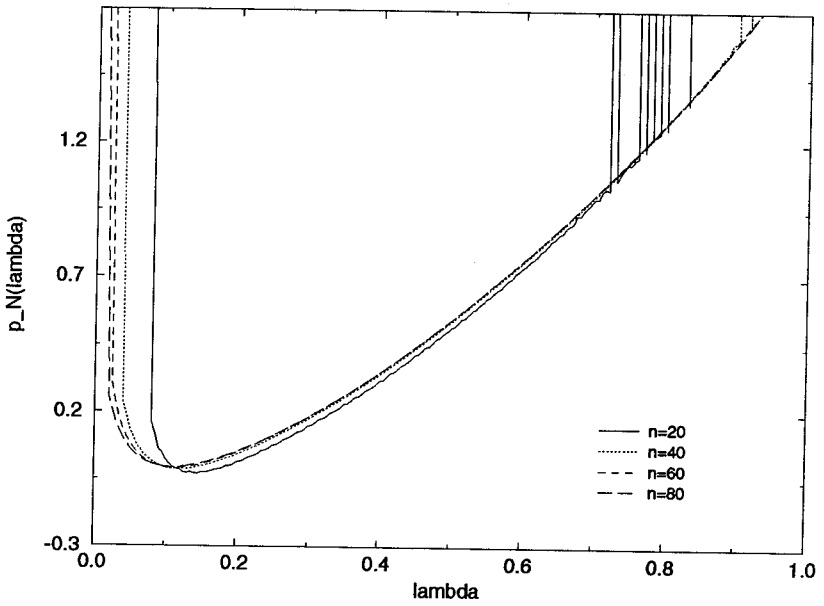

Figure 3.29: Vertically normalized PDF $p_n(\lambda)$ vs λ for 5-nomial stretch model, $\alpha_1 = .01, \alpha_2 = .1, \alpha_3 = .2, \alpha_4 = .3, \alpha_5 = .39$

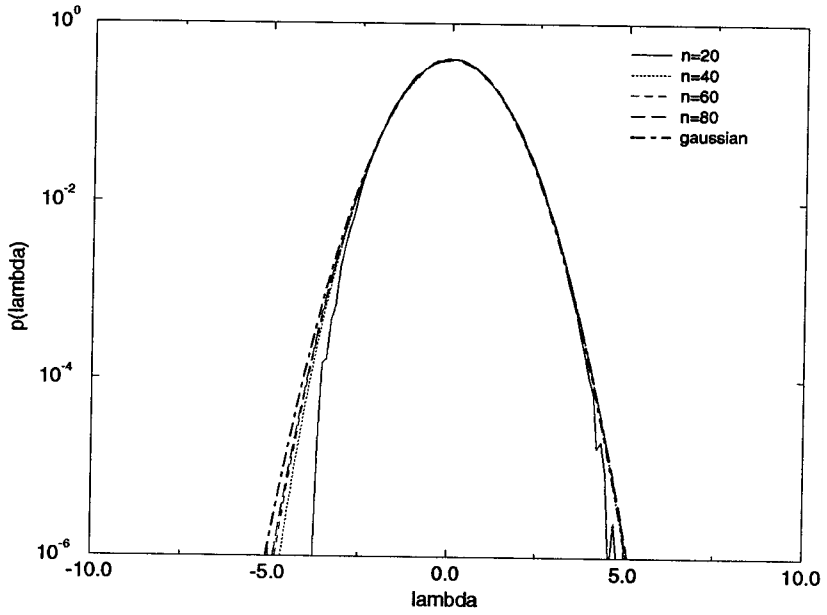

Figure 3.30: Normalized PDF $p(\lambda)$ vs λ for 5-nomial stretch model, $\alpha_1 = .183, \alpha_2 = .191, \alpha_3 = .2, \alpha_4 = .212, \alpha_5 = .214$

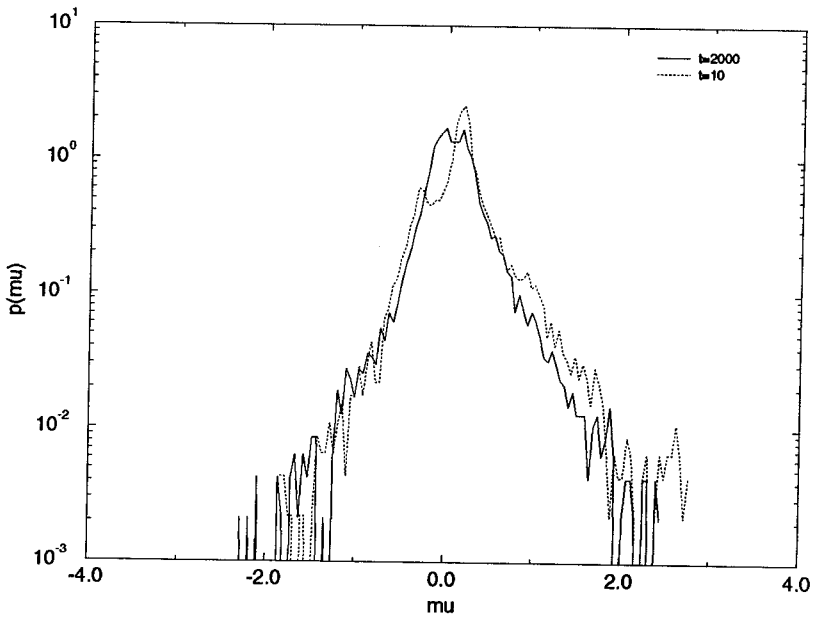

Figure 3.31: PDF $p(\mu)$ of instantaneous stretchings μ for $N = 3,\ \delta = .02$

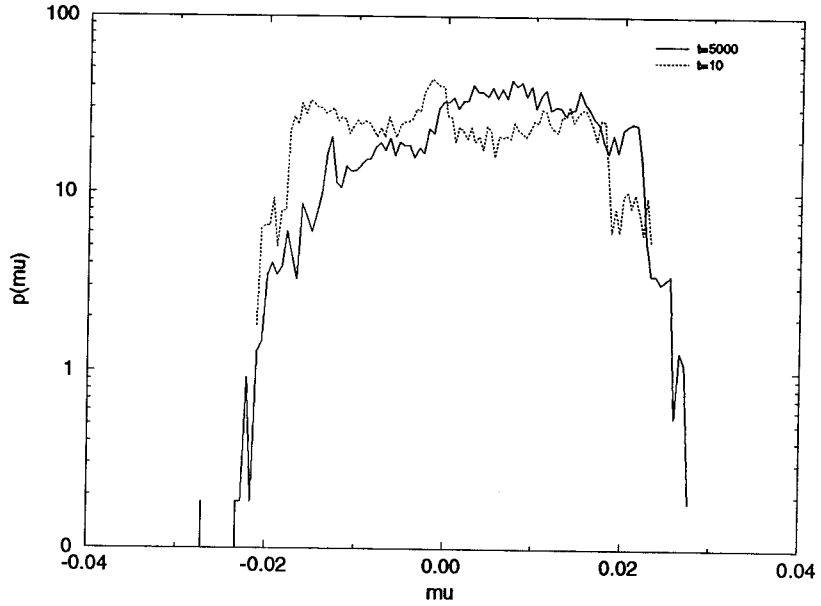

Figure 3.32: PDF $p(\mu)$ of instantaneous stretchings μ for $N = 3,\ \delta = 1.0$

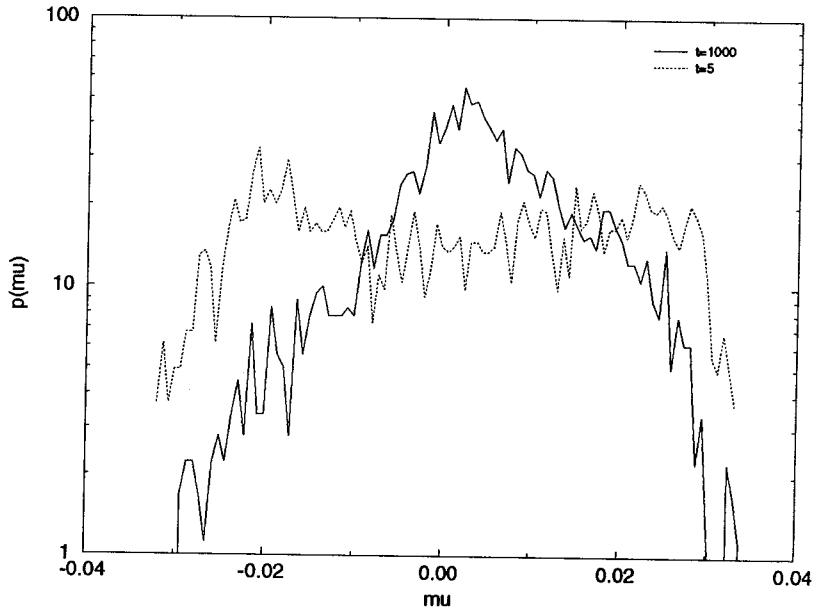

Figure 3.33: PDF $p(\mu)$ of instantaneous stretchings μ for $N = 150,\ \delta = .5$

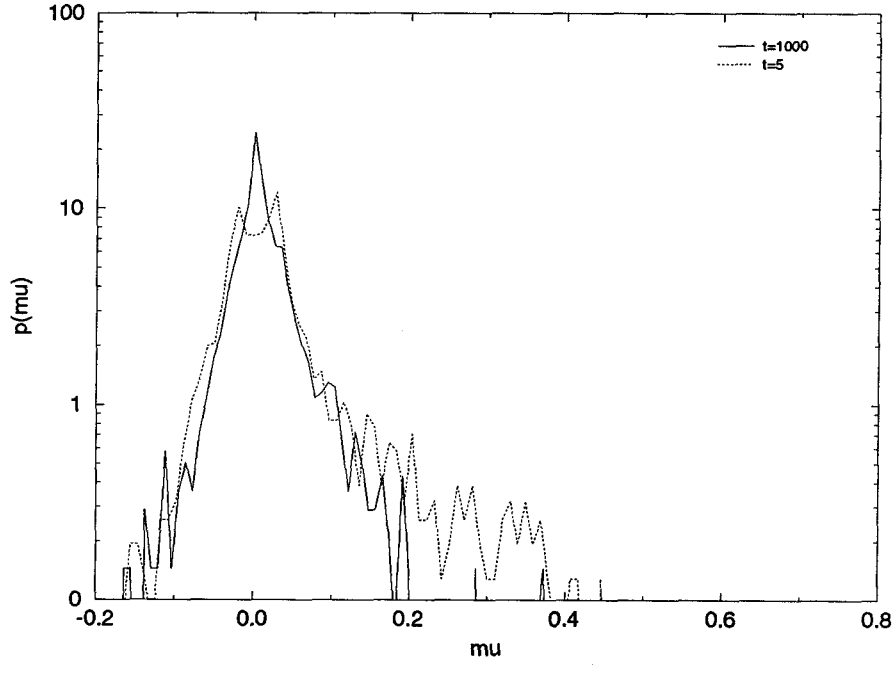

Figure 3.34: PDF $p(\mu)$ of instantaneous stretchings μ for $N = 150,\ \delta = .02$

Chapter 4

The Geometry of Non-Diffusive Interfaces in Vortex Flows

4.1 Introduction

We continue our study of flows induced by N vortices moving themselves under self induction. In this chapter, we examine the stirring of an interfacial line by the N-vortices.

An interesting observation of numerical simulations [78] and theoretical [64] studies of two-dimensional turbulence is that vorticity tends to form large scale coherent structures (inverse energy cascade). This suggests that it may be possible to represent some aspects of the large scale two-dimensional turbulence with the N-vortex model. On the other hand, there is also the formation of fine scales of vorticity (enstrophy cascade) by filamentation which has been observed in many studies [79, 63] and we believe it to be a common result of the vortex interaction. Although we do not have the means of creating very fine scale *vorticity* due to this mechanism (because we maintain a fixed number of discrete vortices), we are certainly capable

of producing this effect on the passive fluid.

The implicit assumption in using the N vortex model then, is that the *dynamical* effects due to the fine scale vorticity is ignored. The stirring observed in this flow can be seen as that produced by the interaction of vortices of some minimum size.

The relevance of line stretching to fluid mixing is best illustrated by considering an interfacial line that divides two fluids (of scalar value $\xi = 1$ and $\xi = 0$). In the presence of low diffusion and in a bounded flow, one measure of the mixing between the two fluids is the length of the interfacial line as it evolves, as discussed in Chapter 3. However, the spatial distribution of the interfacial line is also important in determining the mixing, and this spatial distribution can be characterized by the spectra. The scalar spectrum is often measured in studies of turbulence, where the results are compared to the theories by Obukhov, Corrsin, Batchelor [73] and Saffman [104] which yield various power-law spectra.

4.2 Telegraph model

The spatial distribution of a scalar can be characterized by its spectrum, which is the Fourier transform of the autocorrelation function

$$C(\mathbf{r}) = \langle \xi(\mathbf{x})\xi(\mathbf{x}+\mathbf{r}) \rangle, \tag{4.1}$$

$$S(\mathbf{k}) = \frac{1}{(2\pi)^d} \int_{-\infty}^{\infty} C(\mathbf{r}) e^{-i\mathbf{k}\cdot\mathbf{r}} d\mathbf{r} \ . \tag{4.2}$$

By the Wiener-Khintchin theorem, $S(k)$ is also equal to $|\hat{\xi}(\mathbf{k})|^2$, where

$$\hat{\xi}(\mathbf{k}) = \frac{1}{(2\pi)^d} \int_{-\infty}^{\infty} \xi(\mathbf{x}) e^{-i\mathbf{k}\cdot\mathbf{x}} d\mathbf{x}. \tag{4.3}$$

In the this section we analyze the spectrum of an interfacial line that is sliced by

a one-dimensional cut. For our non-diffusive flow, we find it convenient to represent the spatial distribution of the scalar $\xi(x)$ by an 'on-off' telegraph signal that takes on the values of either 1 or -1 as a function of the position x along the cut (we take the value of 1 and -1 rather than 1 and 0 for convenience, since normalization by $\langle\xi\rangle$ and $\langle\xi^2\rangle$ will force these values anyway). The autocorrelation function can then be expressed as

$$C(r) = E\{\xi(x)\xi(x+r)\} = \sum_{i=1}^{2} \zeta_i P(\zeta_i) \tag{4.4}$$

where ζ_i are values associated with the possible states, which we will call odd or even: The even state being given by

$$\{\xi(x) = 1, \xi(x+r) = 1\} \text{ or } \{\xi(x) = -1, \xi(x+r) = -1\},\ \zeta_1 = 1 \tag{4.5}$$

and the odd state by

$$\{\xi(x) = 1, \xi(x+r) = -1\} \text{ or } \{\xi(x) = -1, \xi(x+r) = 1\},\ \zeta_2 = -1\ . \tag{4.6}$$

Note that $r = |r|$, and the derivation of $C(r)$ then only requires the evaluation of the probabilities for each possible state ζ

$$P(\zeta_1) = P(\text{even number of transition points in } r) \tag{4.7}$$

$$P(\zeta_2) = P(\text{odd number of transition points in } r)\ , \tag{4.8}$$

and

$$C(r) = P(\text{even}) - P(\text{odd}) \tag{4.9}$$

4.2.1 Random distribution

Consider the case where the scalar $\xi(x)$ is randomly distributed, such that the locations of the transition points are given by the Poisson distribution.

$$P(k) = \frac{(\lambda r)^k e^{-\lambda r}}{k!} \; ; \quad k = 0, 1, 2, 3... \tag{4.10}$$

where k refers to the number of 'events' or in our case the number of transition points that occur in the interval $[x, x+r]$. Following the analysis of Rice or Papoulis [100, 94], the probability of there being an even number of points in the interval r is

$$P(\text{even}) = \sum_{k \text{ even}} \frac{(\lambda r)^k e^{-\lambda r}}{k!} \; ; \quad k = 0, 2, 4... \tag{4.11}$$

$$= e^{-\lambda r} \cosh(\lambda r) \tag{4.12}$$

and an odd number of points

$$P(\text{odd}) = e^{-\lambda r} \sinh(\lambda r) \; . \tag{4.13}$$

Therefore, using Eq. (4.9),

$$C(r) = e^{-2\lambda r} \quad r \geq 0 \tag{4.14}$$

which is just the standard exponential decay of correlations. Taking the Fourier transform of Eq. (4.14),

$$S(k) \sim \frac{\lambda}{k^2 + \lambda^2}, \tag{4.15}$$

so that $S(k) \sim k^{-2}$ for $k \gg \lambda$. As a check we generate $\xi(x)$ assuming a Poisson distribution as shown in Figure 4.1 and plot the autocorrelation function $C(r)$ and the spectrum $S(k)$ of this signal in Figures 4.2 and 4.3 respectively. For $k \ll \lambda$, $S(k) \sim \frac{1}{\lambda} \sim$ constant which is basically white noise.

4.2.2 Fractal (power-law) distribution

For a fractal interface distribution, we perform a local geometric analysis similar to that by Vassilicos and Hunt [112]. It must be noted that the question of *existence* of fractal distribution of lines in fluid mechanics, and especially in turbulent flows is in a state of debate (see [34, 80, 21, 106, 76] for interesting discussions and presentation of experimental evidence).

For a fractal distribution with dimension D $(0 < D < 1)$, the box counting method is often used to characterize the geometry with the equation

$$N(r) \sim r^{-D} \ . \tag{4.16}$$

Strictly speaking, $N(r)$ is the *minimum* number of boxes of size r that will cover all the (transition) points, but we approximate this by a uniform, side by side covering of the domain by the boxes. Let $N_E(r)$ be the number of empty boxes and $N_T(r)$ be the total number of boxes possible, so that over a unit domain

$$N_T(r) = \frac{1}{r}, \tag{4.17}$$

$$\begin{aligned} N_E(r) &= N_T(r) - N(r) && (4.18) \\ &= \frac{1}{r} - cr^{-D} = \frac{1 - cr^{1-D}}{r}. && (4.19) \end{aligned}$$

The probability of an empty box $P_E(r)$ given that all boxes are size r is

$$P_E(r) = \frac{N_E(r)}{N_T(r)} = 1 - cr^{1-D} \tag{4.20}$$

and the probability of an occupied box is given by

$$P_F(r) = \frac{N(r)}{N_T(r)} = cr^{1-D}(r) \ . \tag{4.21}$$

We then decompose $P(\text{even})$ and $P(\text{odd})$ into contributions from the empty and filled boxes

$$P(\text{even}) = P(\text{even}|\text{empty})P_E(r) + P(\text{even}|\text{filled})P_F(r) \tag{4.22}$$

$$P(\text{odd}) = P(\text{odd}|\text{empty})P_E(r) + P(\text{odd}|\text{filled})P_F(r) \tag{4.23}$$

and using Eq(4.9)

$$C(r) = P_E(r)[P(\text{even}|\text{empty}) - P(\text{odd}|\text{empty})] + P_F(r)[P(\text{even}|\text{filled}) - P(\text{odd}|\text{filled})] . \tag{4.24}$$

It is clear that within the empty boxes, $P(\text{even}|\text{empty}) \approx 1$ and $P(\text{odd}|\text{empty}) \approx 0$ since there are no transition points. We will now argue that in the filled boxes $[P(\text{even}|\text{filled}) - P(\text{odd}|\text{filled})]$ is not a function of r. Consider the average number of boxes of size r_2 within a filled box of size r_1, with $r_2 < r_1$.

$$N(r_1) = cr_1^{-D} \tag{4.25}$$

$$N(r_2) = cr_2^{-D} \tag{4.26}$$

and assuming uniform distribution of the $N(r_2)$ boxes in the $N(r_1)$ boxes, (N.B. this is a reasonable assumption, given that $N(r)$ gives no additional weighting to the different measures in the boxes anyway — if we construct a fractal distribution with a non-uniform distribution of the boxes within the boxes, as will be the case if we prescribe a fractal correlation dimension, the results of this section will change. This point is brought up again later.) the average number of r_2 boxes per r_1 box is $\left(\frac{r_2}{r_1}\right)^{-D}$. Thus the geometry depends only on the ratio, and not on r. Therefore, Eq.(4.24) becomes

$$C(r) \approx (1 - cr^{1-D}) + \text{const} \times r^{1-D} \tag{4.27}$$

$$\approx 1 - \text{const} \times r^{1-D} \tag{4.28}$$

and

$$S(k) = FT\{1 - cr^{1-D}\} \sim k^{-(1-D)-1} = k^{D-2} \,. \tag{4.29}$$

As a check, we numerically generate some sample cases with various values of D and plot $\xi(x), C(r)$ and $S(k)$ in Figures 4.4, 4.5, and 4.6 for $D = .3$, Figures 4.7, 4.8, and 4.9 for $D = .5$, and Figures 4.10, 4.11, and 4.12 for $D = .75$.

We must note however that merely assuming a fractal geometry with some dimension D does not sufficiently define the geometry to enable us to specify the autocorrelation and the spectrum of $\xi(x)$ fully. To illustrate, we bring up the idea of a multifractal geometry (see for example [51, 49, 50, 40, 1, 111, 49, 76] and references therein) and the accompanying concept of a spectrum of dimensions which are defined as follows:

$$D_q = \frac{1}{q-1} \lim_{r \to 0} \frac{\log \sum_i \mu_i^q(r)}{\log r} \tag{4.30}$$

where q is an index taking the values between $-\infty$ and $+\infty$ and μ_i is the measure of box i. For our scalar interface application, we can think of μ_i as being proportional to the number of transition points within the box i. The fractal dimension D that we have been using thus far is just Eq.(4.30) with $q = 0$ and it is easy to see that it is equivalent to the box counting method we have been using. It is clear then that the spectrum of dimensions D_q, $-\infty < q < \infty$ defines the geometry much more fully than a single $D_0 = D$. The physical significance of the various values of D_q can be seen when we consider that probability of transition points in different boxes are likely to be different — varying the value of q allows us to put different weighting on the uneven measure of the boxes. Thus D_q's are all equal only if the measure μ_i of the boxes are uniform. The point of this discussion is that as far as the specification of the scalar interface geometry goes, some of the other dimensions, in particular the correlation dimension D_2 may have a stronger link to the scalar autocorrelation function and the power spectrum. We take up this issue later in this chapter when we discuss the numerical results of the stirring by N vortices.

We also note that the connection between the stretching properties (distribution of Lyapunov exponents) and the spectrum of fractal dimensions (and the scalar spectrum, as mentioned above) for chaotic flows have been made by Ott and Antonsen [90, 1].

Two special cases (k^{-1} and k^{-2})

Batchelor predicted a k^{-1} spectrum for the viscous convective subrange of three-dimensional turbulence and in the inertial range for the enstrophy spectrum as well in two-dimensional turbulence. The k^{-2} spectrum is also of interest, as Saffman predicted such a spectrum (for enstrophy) for very discontinuous spatial distributions of vorticity. See Lesieur [73] for additional discussions and derivations. One reason for the recent focus on the spectra of scalar distributions is that numerical simulations have not been able to establish fully the type of spectra that should exist for two dimensional turbulent flows.

It has been suggested by Vassilicos and Hunt [112] that the spectra k^{-2} and k^{-1} are just the special cases related to the sparse ($D = 0$) and the space-filling ($D = 1$) distribution of interfaces. Crisanti et al. [26] have also reported similar results using different arguments. Our results of this section indicate a similar conclusion is warranted. However, we must also point out that these are not the exclusive sources of these spectrum. Antonsen and Ott [1] also arrive at the k^{-1} spectrum for the spectrum of passive scalars in chaotic flows. They find that in the presence of KAM surfaces the initial value problem yields the k^{-1} spectrum as $t \rightarrow \infty$, while they determine that the spectrum cannot be approximated as a power law in k in the absence of KAM surfaces. In addition, they show that for the steady state problem (with a scalar source term), where the measure was found *no* to have fractal properties, the k^{-1} spectrum is also reached. In the next section we show another type of scalar geometry that can produce the k^{-1} spectrum. Pierrehumbert [96] argues that the k^{-1} spectrum derived through the space-filling

fractal distribution is sensitive to the details of the geometry, and poses a 'fragile' limit. There is also experimental and theoretical evidence that point to discrepancies with the k^{-1} spectrum in its general form. In their measurement of the spectra of high Schmidt number turbulent jets, Miller and Dimotakis [81] did not observe a k^{-1} spectrum. Dimotakis and Miller [33] have also expressed concerns about the validity of Batchelor's spectrum having to do with the divergence of the variance of fluctuations

$$\overline{(\xi - \bar{\xi})^2} = \frac{1}{\pi} \int_0^\infty S(k) dk \ . \tag{4.31}$$

It is clear that the relationship between the scalar spectrum and the scalar geometry is still not fully resolved for general flows and that there are several possibilities for the kinematic sources of the k^{-1}, k^{-2}, and even $k^{-5/3}$ spectrum. Identifying the link between the dynamic arguments (involving dimensional analysis and conservation laws) for the power law spectrum and their kinematic manifestation remains an open task.

4.2.3 Large scale power-law, random small scales

The notion of $1/f^\gamma$, (γ near 1) spectra is well known in the study of electrical noise and relaxation phenomena. Although there are many possible physical sources of this spectra, one of the simplest is the idea of activated random processes [38, 83, for example]. A random process with a characteristic relaxation length scale τ or density $\lambda \sim 1/\tau$ has an autocorrelation $C(r) \sim \exp(-\lambda r)$, and the Lorentzian spectrum Eq. (4.15) derived above. We call the characteristic inverse length scale λ the density, because it can roughly be thought of as the density of the interfacial lines per unit length. Imagine now a set of intervals, each with a different density λ, and autocorrelation within the interval, $C(r;\lambda)$. The autocorrelation function for

the entire set is just the weighted average of each interval,

$$C(r) = c\int_{\lambda_{min}}^{\lambda_{max}} C(r;\lambda)p(\lambda)d\lambda \tag{4.32}$$

$$= c\int_{\lambda_{min}}^{\lambda_{max}} e^{-\lambda r}p(\lambda)d\lambda\ . \tag{4.33}$$

The spectrum is then

$$S(k) = \frac{c}{2\pi}\int_{-\infty}^{\infty} e^{-ikr}\int_{\lambda_{min}}^{\lambda_{max}} e^{-\lambda r}p(\lambda)d\lambda dr \tag{4.34}$$

$$= \frac{c}{2\pi}\int_{\lambda_{min}}^{\lambda_{max}} p(\lambda)\int_{-\infty}^{\infty} e^{-\lambda r}e^{-ikr}drd\lambda \tag{4.35}$$

$$S(k) = \frac{c}{2\pi}\int_{\lambda_{min}}^{\lambda_{max}} p(\lambda)\frac{\lambda}{k^2+\lambda^2}d\lambda\ . \tag{4.36}$$

Take the particular case of $p(\lambda) \sim 1/\lambda$: Then from Eq. (4.36)

$$S(k) = \frac{c}{2\pi}\int_{\lambda_{min}}^{\lambda_{max}} \frac{d\lambda}{k^2+\lambda^2} \tag{4.37}$$

$$= \frac{1}{k}\tan^{-1}\left(\frac{\lambda}{k}\right)\Bigg|_{\lambda_{min}}^{\lambda_{max}} \tag{4.38}$$

$$= \frac{1}{k}\left[\tan^{-1}\left(\frac{\lambda_{max}}{k}\right) - \tan^{-1}\left(\frac{\lambda_{min}}{k}\right)\right]. \tag{4.39}$$

Then for $\lambda_{min} \ll k \ll \lambda_{max}$,

$$S(k) \approx \frac{1}{k}\frac{\pi}{2} \sim k^{-1}. \tag{4.40}$$

We point out that this provides a possible kinematic explanation for the k^{-1} spectrum, one that is probably more robust than a fractal distribution. Locally, the interfacial lines are randomly distributed, but there is a power law dependence for the density of the lines. For the more general case of $p(\lambda) \sim 1/\lambda^{\gamma}, (\gamma \approx 1)$, integrating Eq. (4.36) gives us

$$S(k) \sim k^{-\gamma} \tag{4.41}$$

for $\lambda_{min} \ll k \ll \lambda_{max}$.

In applying the above considerations to our scalar distribution $\xi(x)$, we consider an ensemble of local interfacial striations, each with a local density of λ. If $p(\lambda)$ can be represented by a power law, then we can expect a power law spectra of the same power exponent as well. As for the *physical* mechanism that might create this sort of a distribution, we conjecture that the stretch and fold action of the vortices on the interfacial line may be locally random, but have different densities at different locations, caused by the uneven distribution or alignment.

4.3 Spatial distribution of lines by vortex stirring

We now turn to the spectra of interfaces advected by N-vortices. We shall examine the one-dimensional spectra by taking a one-dimensional cut through interfacial line structures such as shown in Figure 3.17 of chapter 3. Figure 4.13 shows the construction of the one dimensional $\xi(x)$ profile with a cut through $y = 0$ for the simulation involving $N = 3$, $\delta = 1.0$. The scalar distribution $\xi(x)$ itself is shown in Figure 4.14. The autocorrelation $C(r)$ and the spectrum $S(k)$ are plotted in Figure 4.15 and 4.16 respectively. An interesting feature of the spectrum is the power-law form, with an exponent of around 1.7 (note that the linear fit in the log-log spectrum plot is only approximate, and of a limited range). We show similar results for the $N = 150$, $\delta = .5$ case in Figures 4.17, 4.18, 4.19, 4.20, and for the $N = 150$, $\delta = .1$ case in Figures 4.21, 4.22, 4.23, and 4.24. These other cases show slightly different exponents but otherwise show similar trends. The result of a different cut at $x = 0$ through the interfacial structure associated with Figure 4.22 is shown in Figures 4.25 and 4.26. The similarity of the results supports the argument for isotropy.

There are two issues that arise with respect to the stirring of the interfacial lines

by N-vortices: One is a characterization of the resulting spatial distribution $\xi(x)$, and the other is an understanding of the basic physical mechanism behind such a distribution.

A box counting algorithm has been used on several one-dimensional cuts through the interfacial line structure created from the stirring due to N vortices. This method consists of finding the function $N(r)$ which is the number of boxes of size r required to cover all the transition points. If there is a power-law dependence on r, then the geometry is said to be fractal where the dimension D (or D_0) is the negative exponent of r. As a check, we first apply the box counting method to the fractal distribution of points in Figure 4.4. The plot of $\log(r)$ vs $\log(r)$ shown in Figure 4.27 shows an acceptable constant-slope range. The box counting is applied to the structure shown in Figure 4.14 and the function $N(r)$ is shown in Figure 4.28 as a log-log plot. The slope of this plot is not constant — in fact, the curve appears nearly quadratic (it would have to be linear for fractal distributions). The 'local dimension' $D(r) = d[\log(N(r))]/d[log(r)]$ then appears to be a linear function. We can fit this curve to an equation of the form

$$N(r) = ar^{-(b+c\log r)} . \tag{4.42}$$

Although we have no physical motivation to suggest why this might be occuring, we must also point out that it is a more general form of $N(r)$ than a fractal distribution, for whose appearance there is also a lack of convincing argument for the N-vortex problem. A *two-dimensional* box counting measurement of the same scalar interface distribution gave us similar results ($D(r)$ varying between 1 and 2 for two-dimensions) as seen in Figure 4.29. Evaluation of $N(r)$ for the $N = 150, \delta = .5$ and $N = 150, \delta = .1$ cases (one-dimensional cuts) are shown in Figures 4.30 and 4.31 which also show similar results. Whether this is due to the short time nature of our simulations or whether this is a time invariant distribution caused by this type of vortex flow is not certain. We note that a distribution similar to this is also

seen in the experimental study of a turbulent jet by Miller and Dimotakis [80], and they apply a log-normal stochastic model to achieve a good fit to their $N(r)$ plot. More recently, Catrakis and Dimotakis [21] have also obtained similar results for the turbulent jet.

Using the method of section 4.2.2, the autocorrelation function corresponding to Eq. (4.42) is

$$C(r) \sim 1 - ar^{1-(b+c\log r)} \tag{4.43}$$

and the spectra is given by the Fourier Transform of Eq. (4.43). It may be convenient to think of the $(c\log r)$ component of $D(r) = (b + c\log r)$ as the 'correction' term to the constant dimension D associated with a strictly power-law fractal distribution. However, with the parameters a, b, and c, it is not difficult to fit this $C(r)$ to other convenient functions such as the stretched exponential function $\sim \exp(-a|r|^{\gamma})$ which also produces a power law spectrum [83] $S(k) \sim k^{(-1+\gamma)}$. Interestingly enough, we encountered this same Fourier pair in the stable probability distribution law of Chapter 2 (Eqs. (2.29) and (2.30)). The stretched exponential autocorrelation provides a better fit at large r than the local power-law $(1 - a|r|^{\gamma})$. However, noting the relationship

$$e^{-a|r|^{\gamma}} \approx 1 - a|r|^{\gamma} + \frac{(a|r|^{\gamma})^2}{2} - \ldots \ , \tag{4.44}$$

both functions could provide adequate fit at small r.

In addition to the box counting to determine the function $N(r)$, we have also computed the correlation function $H(r)$ for the one-dimensional interfacial transition points (i.e., the derivative of $\xi(x)$ for the scalar $\xi(x)$, rather than $\xi(x)$ itself). $H(r)$ is defined as the number of pairs of points that are separated by a distance less than r [49, 96].

$$H(r) \equiv \lim_{n\to\infty} \frac{1}{n^2} \sum_{i,j=1}^{n} \theta(r - |\mathbf{x}_i - \mathbf{x}_j|) \equiv \int_0^r C(r')dr' \tag{4.45}$$

where $\theta(x)$ is the Heaviside step function, n is the number of 'particles' making up the set, and $C(r)$ is the usual autocorrelation function. A log-log plots of $H(r)$

is shown in Figure 4.32 for the scalar interface distribution of Figure 4.14 for the $N = 3,\ \delta = 1.0$ case. Figure 4.33 shows the result of a two-dimensional calculation of the quantity $\log(\sum_i \mu_i^2(r))$ versus $\log(r)$. Similarly, Figures 4.34 and 4.35 show $H(r)$ for the $N = 150,\ \delta = .5$ and $N = 150,\ \delta = .1$ cases respectively. A reasonable linear fit in the log-log plot can be seen in all plots indicating a power law function of the form $H(r) \sim r^{D_2}$. The scaling dimension D_2 was introduced earlier in section 4.2.2 in discussing the spectrum of multifractal distributions. The connection between $H(r)$ and D_2 was established by Grassberger and Proccacia [49, 50] when $H(r)$ takes a power-law form. Although they aimed their analysis towards the characterization of strange attractors associated with dissipative dynamical systems, and used time series measurements, we find the geometric characterizations useful in our spatial context as well.

An interesting facet of all this is that the interfacial line stirred by the N vortices can be described as possessing a nearly constant correlation dimension (at least over a limited range) D_2, while not having a fractal dimension for the capacity D_0 (or D). This suggests that measuring the correlation dimension or the correlation function $H(r)$ may provide an independent useful characterization of the scalar geometry apart from the usual box counting function $N(r)$. This makes sense because these are just two of an infinite number of parameter values describing the measure of a geometric set. In fact, D_0 probably has a weaker effect on the spectrum because it does not account for the varying measures of each box.

Although we have devoted a large part of this chapter analyzing the spectrum, we must stress the fact that the spectrum has a non-invertible relationship with the physical distribution $\xi(\mathbf{x})$. That is, identifying a spectrum does not tell us anything specific about the spatial distribution of the scalar, because different types of the scalar distribution can result in the same spectrum. We agree with Pierrehumbert [96] that more direct geometric characterizations such as $H(r)$ provide better description of the geometry than the power spectrum, and suggest further

that evaluations of the functions $N(r)$ and $H(r)$ themselves may be useful, even when the geometry does not adhere to a strict power-law form.

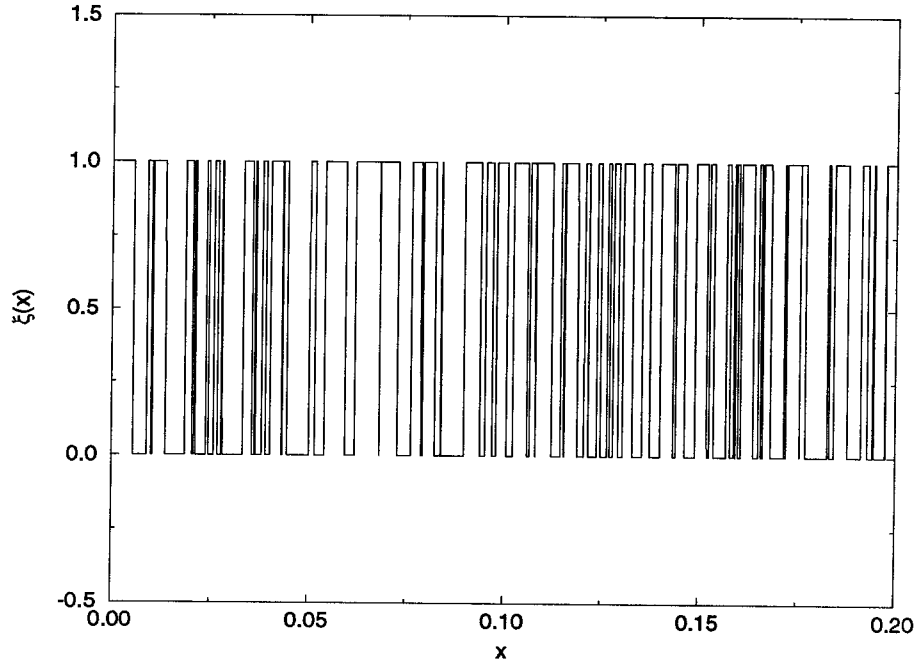

Figure 4.1: $\xi(x)$ vs x for a random distribution of transition points.

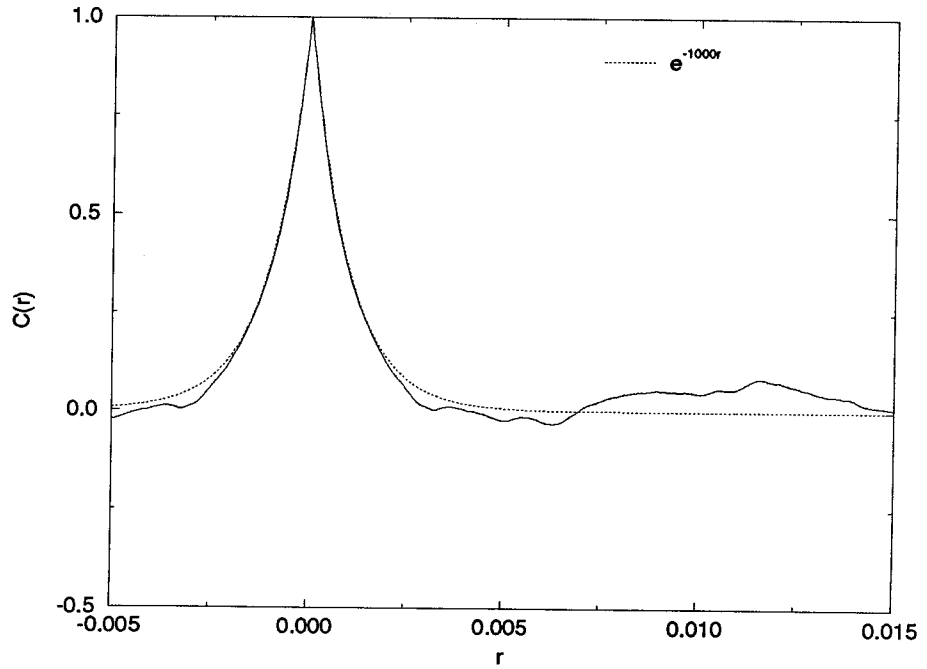

Figure 4.2: Autocorrelation,$C(r)$ vs r for a random distribution of points

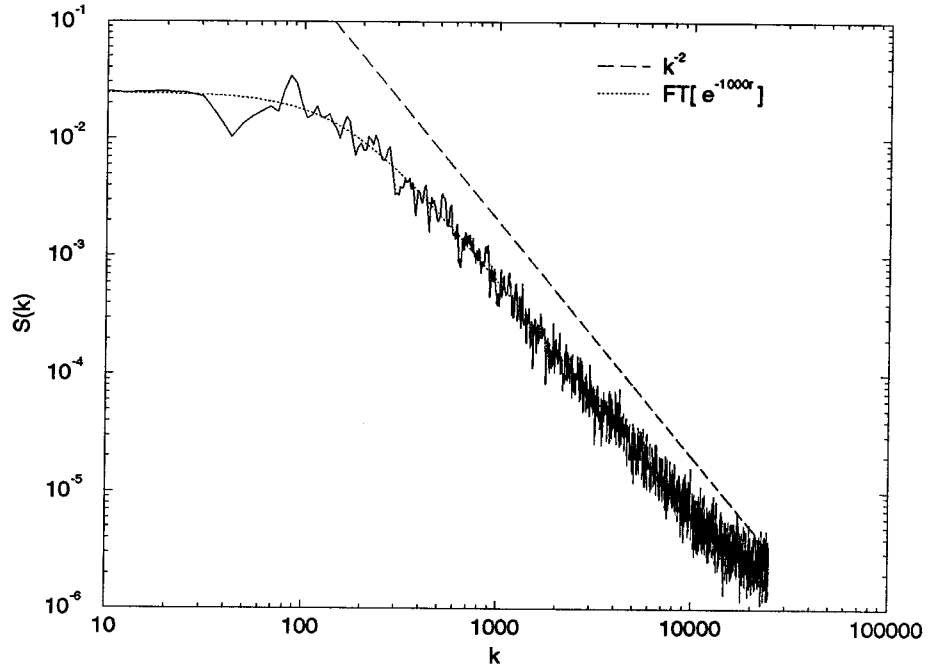

Figure 4.3: Scalar spectrum $S(k)$ vs k of a random distribution of points

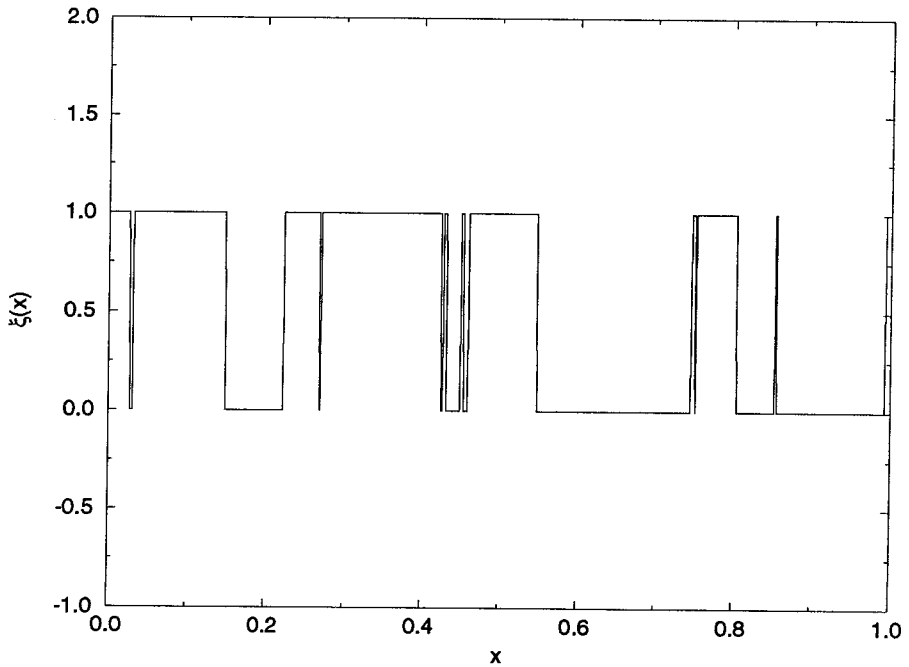

Figure 4.4: One-dimensional cut of a fractal distribution with $D = .3$, $\xi(x)$ vs x

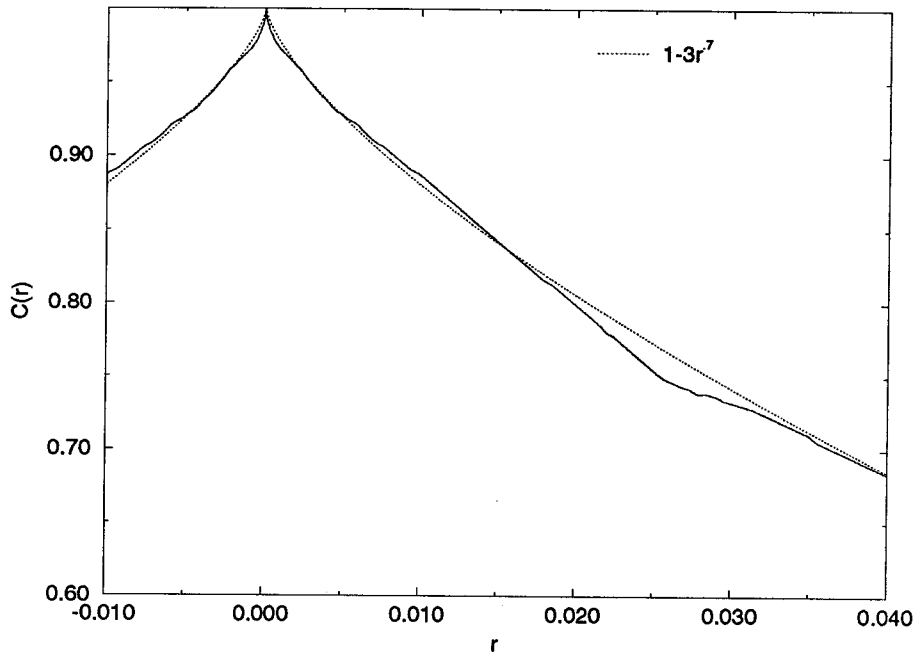

Figure 4.5: Autocorrelation for $D = .3$, $C(r)$ vs r

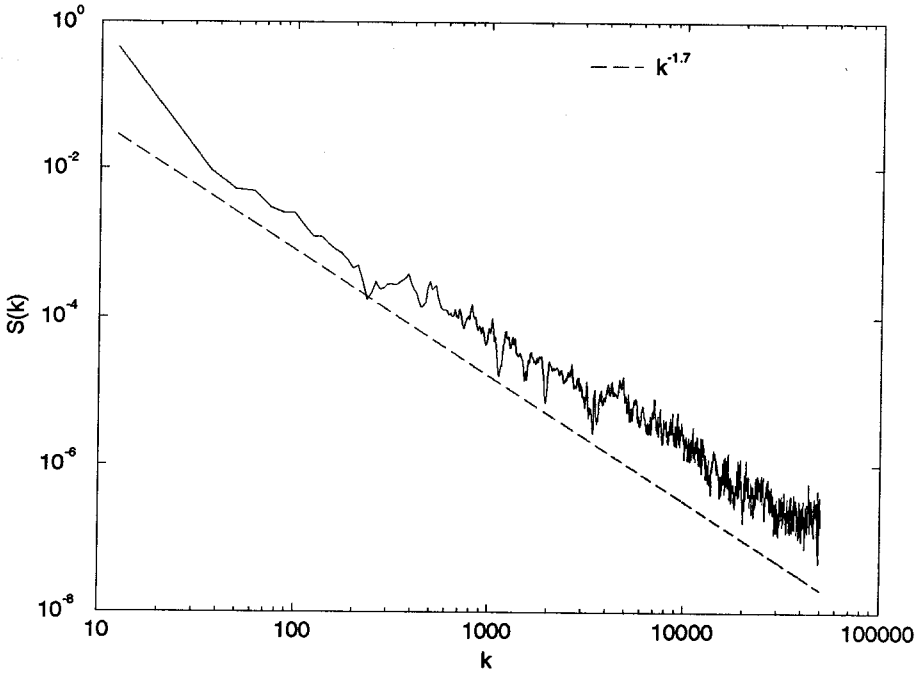

Figure 4.6: Scalar spectrum for $D = .3$, $\xi(x)$ vs x

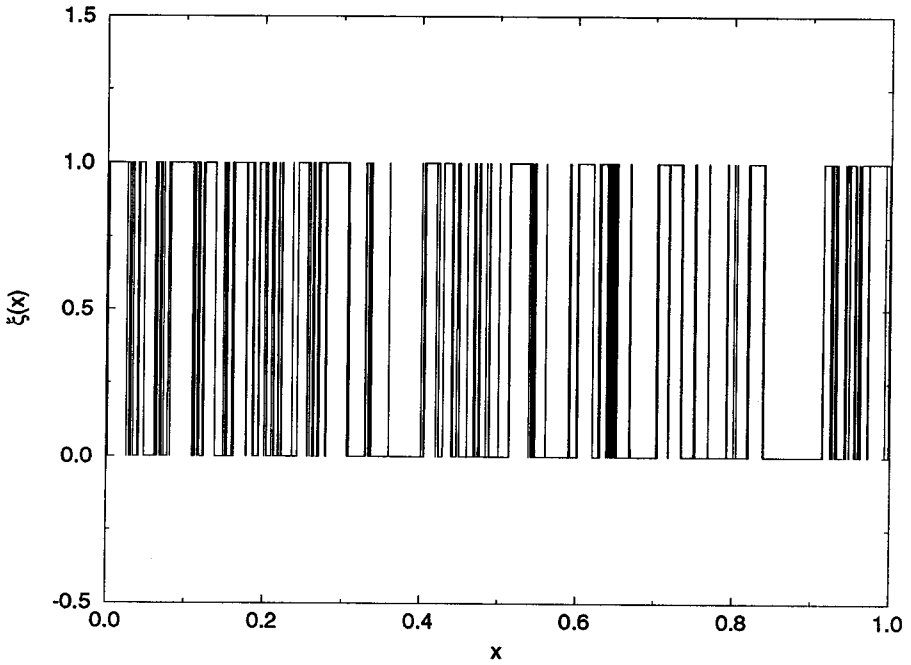

Figure 4.7: One-dimensional cut of a fractal distribution with $D = .5$, $\xi(x)$ vs x

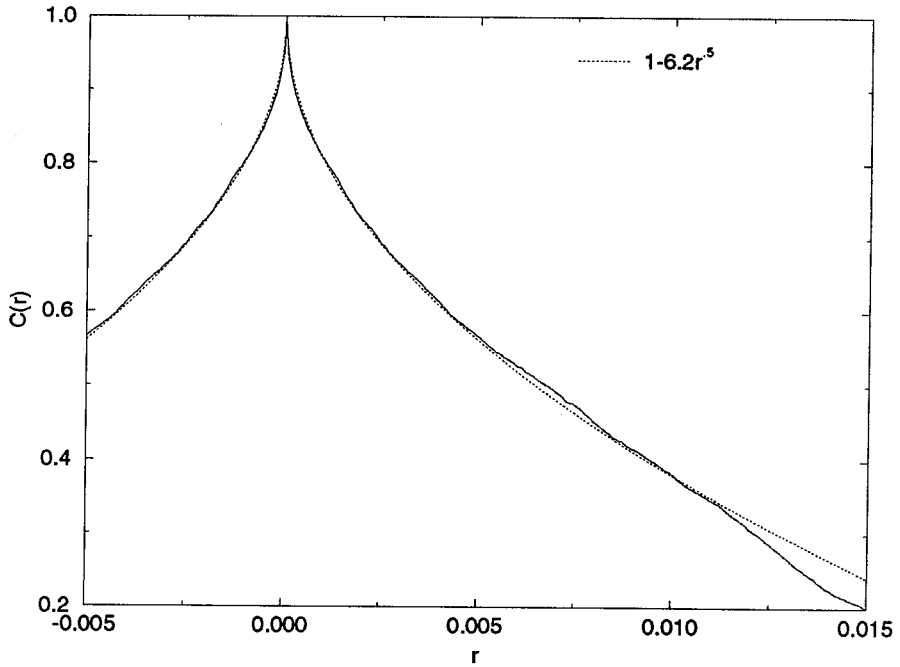

Figure 4.8: Autocorrelation for $D = .5$, $C(r)$ vs r

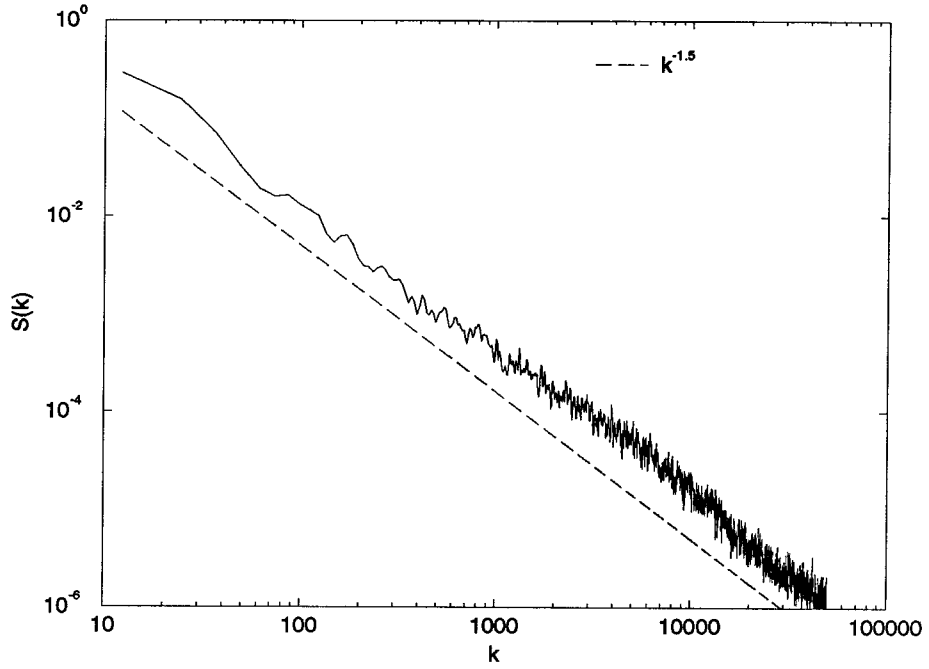

Figure 4.9: Scalar spectrum for $D = .5$, $S(k)$ vs k

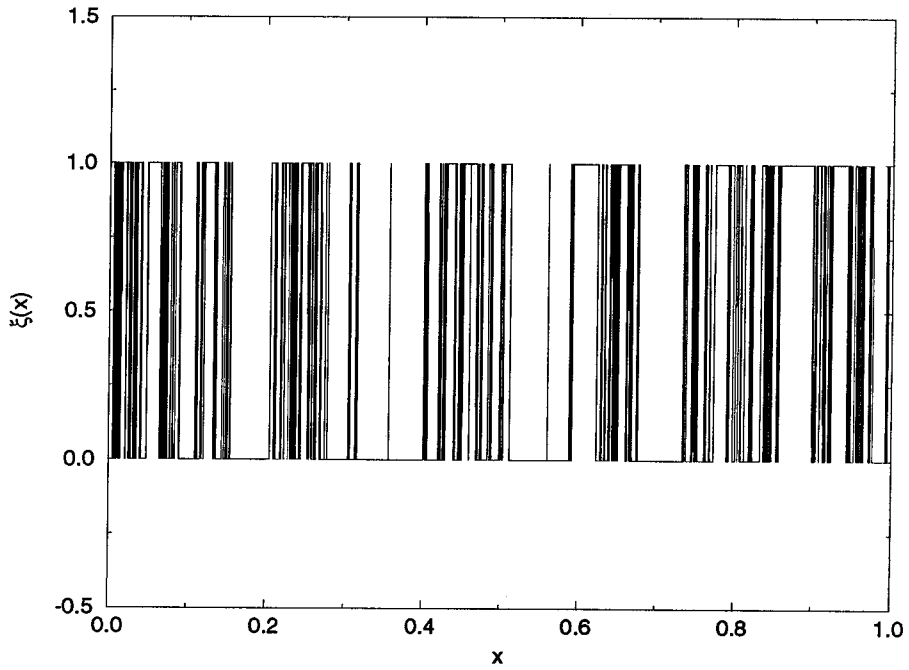

Figure 4.10: One-dimensional cut of a fractal distribution with $D = .75$, $\xi(x)$ vs x

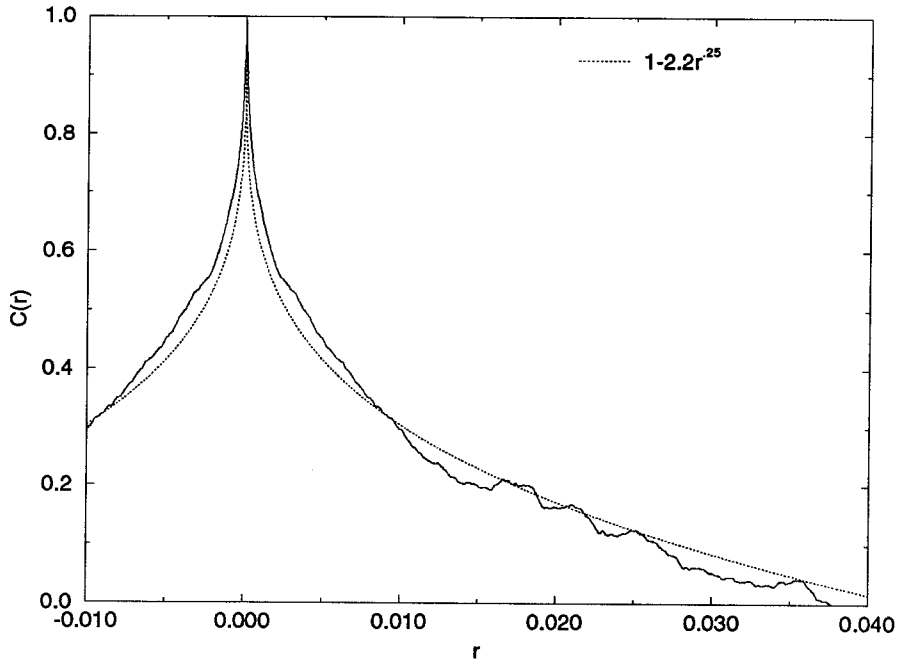

Figure 4.11: Autocorrelation for $D = .75$, $C(r)$ vs r with power-law and stretched exponential fit

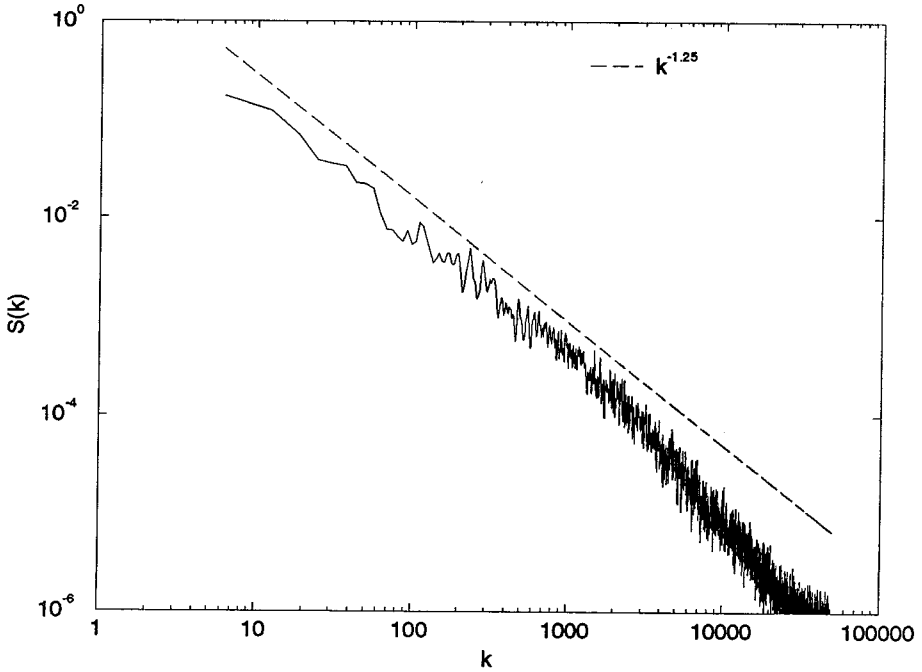

Figure 4.12: Scalar spectrum for $D = .75$, $S(k)$ vs k

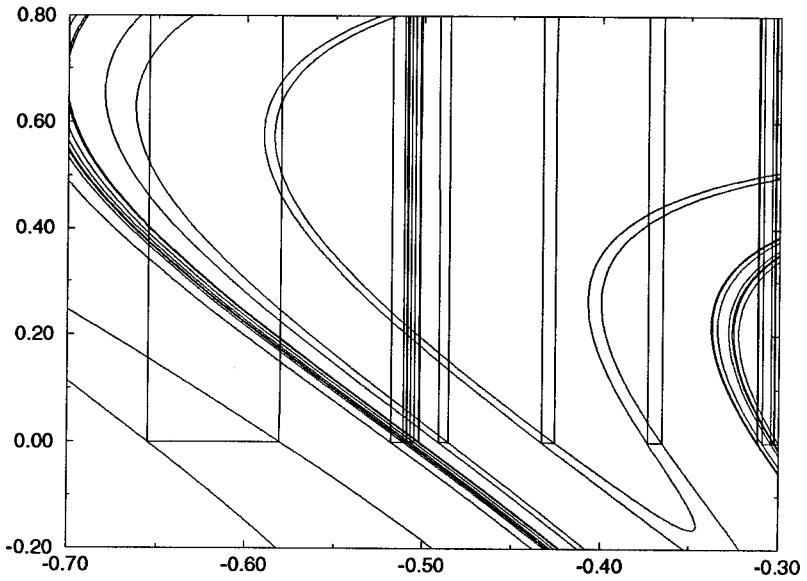

Figure 4.13: Construction of the one-dimensional cut at $y = 0$ from the interfacial line stirred by N vortices, $N = 3, \delta = 1.0$

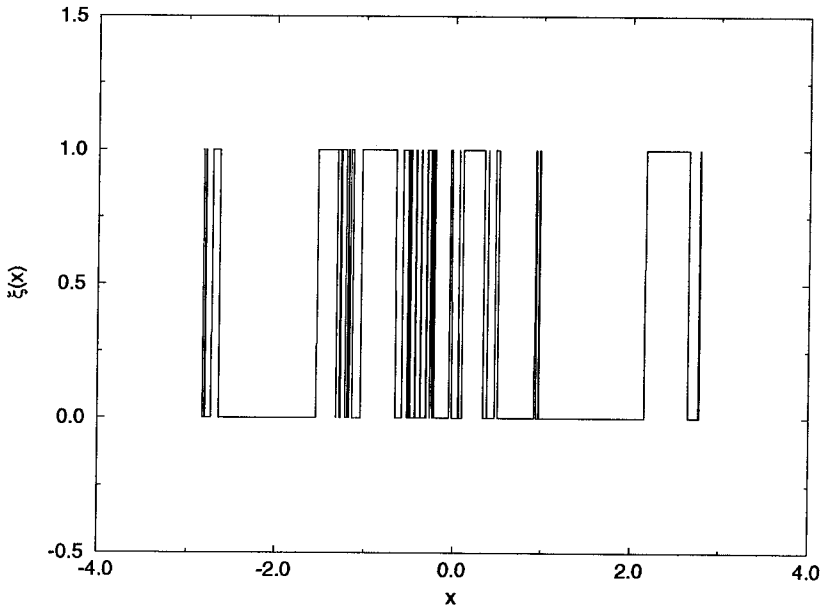

Figure 4.14: One-dimensional cut of interfacial line from $N = 3, \delta = 1.0$ N-vortex simulation at $y = 0$, $\xi(x)$ vs x

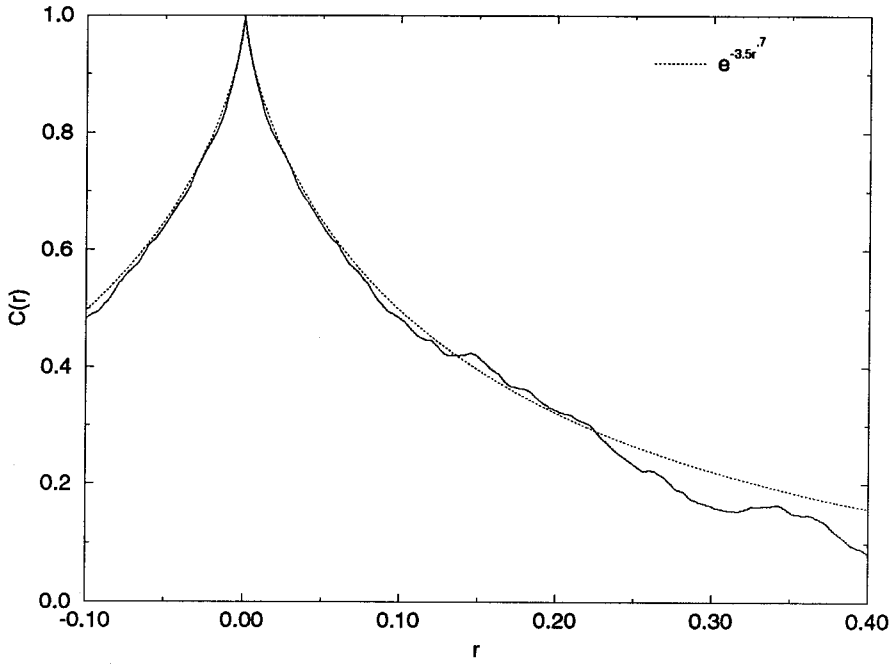

Figure 4.15: Autocorrelation of $\xi(x)$ for $N = 3, \delta = 1.0$, $C(r)$ vs r

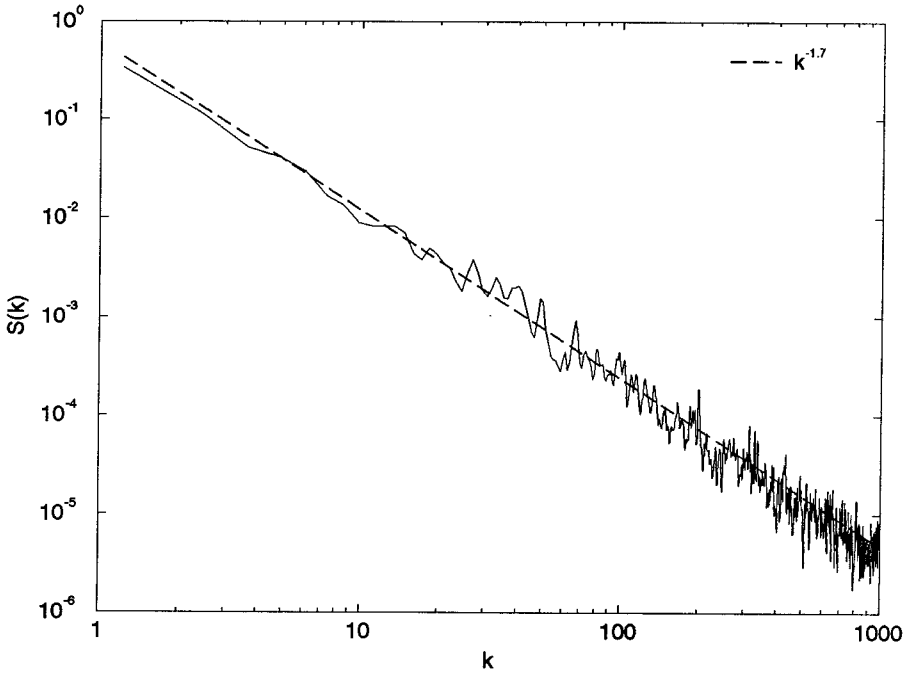

Figure 4.16: Scalar spectrum for $N = 3, \delta = 1.0$, $S(k)$ vs k

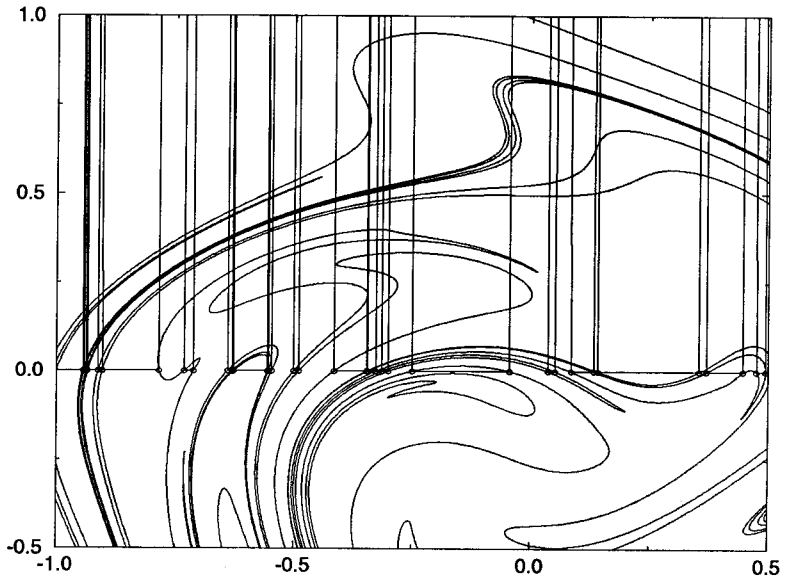

Figure 4.17: Construction of the one-dimensional cut at $y = 0$ from the interfacial line stirred by N vortices, $N = 150, \delta = .5$

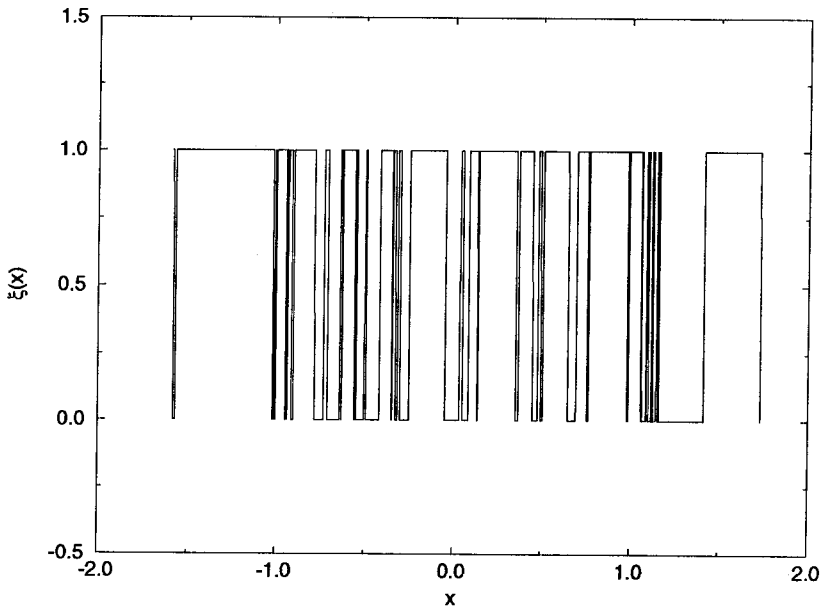

Figure 4.18: One-dimensional cut of interfacial line from $N = 150$, $\delta = .5$ N-vortex simulation at $y = 0$, $\xi(x)$ vs x

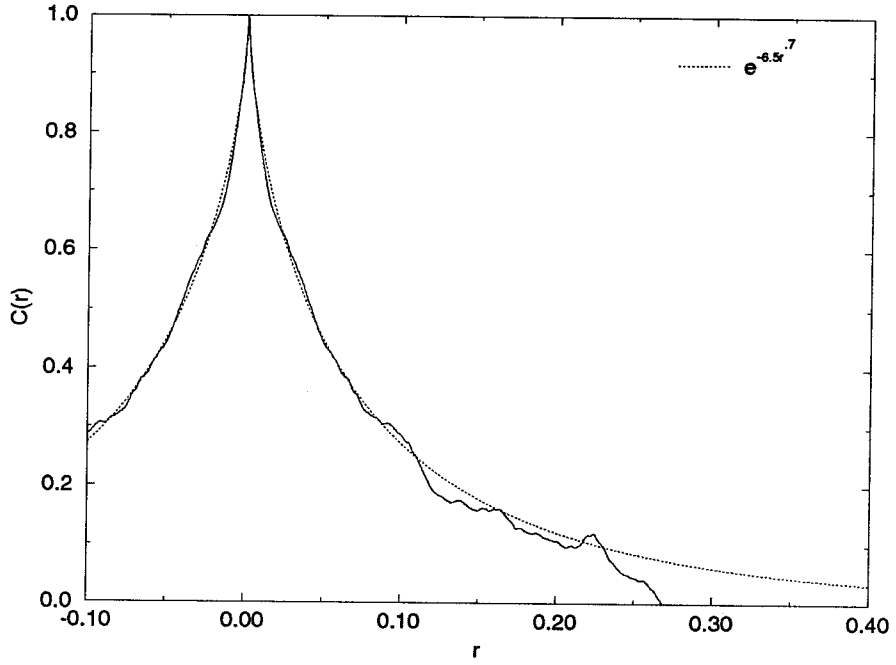

Figure 4.19: Autocorrelation of $\xi(x)$ for $N = 150, \delta = .5$, $C(r)$ vs r

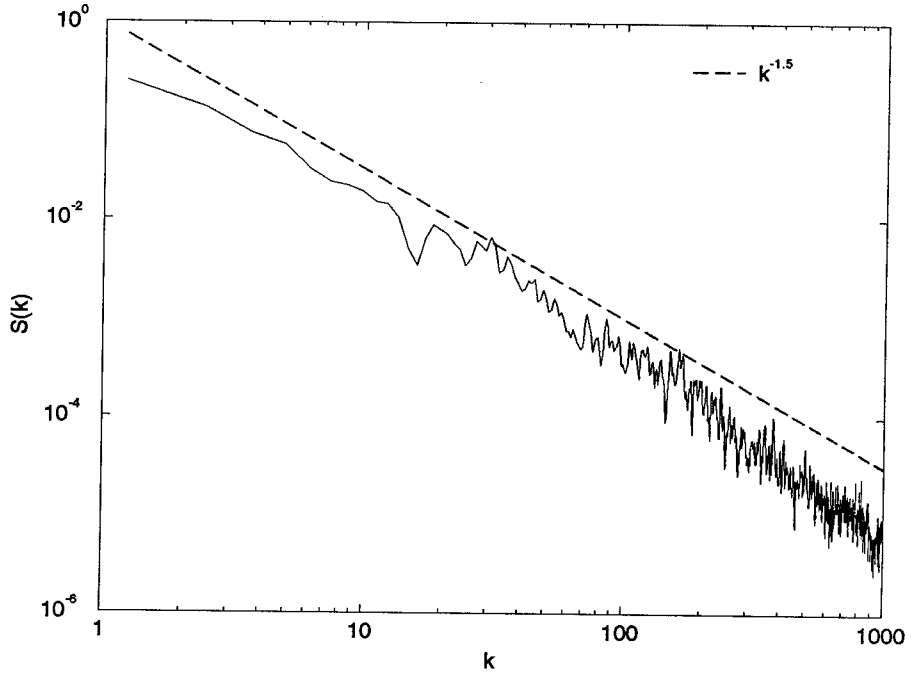

Figure 4.20: Scalar spectrum for $N = 150,\ \delta = .5\ ,\ S(k)$ vs k

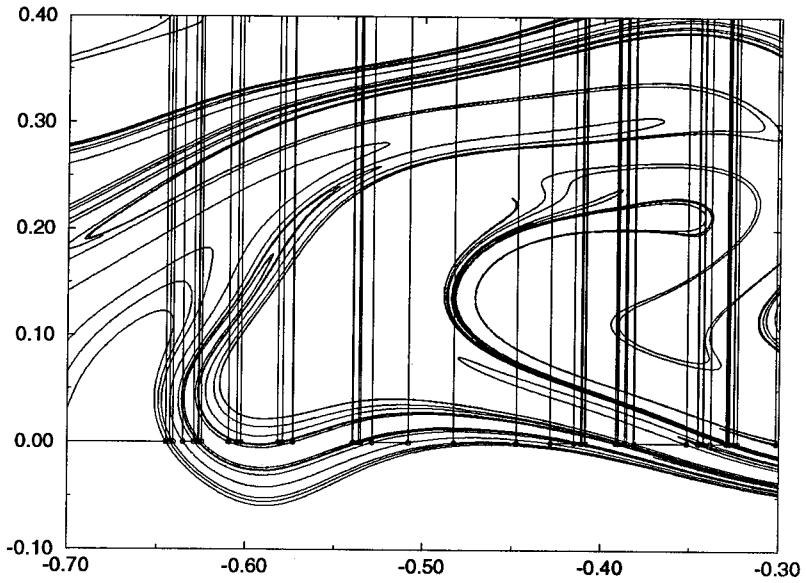

Figure 4.21: Construction of the one-dimensional cut at $y = 0$ from the interfacial line stirred by N vortices, $N = 150, \delta = .1$

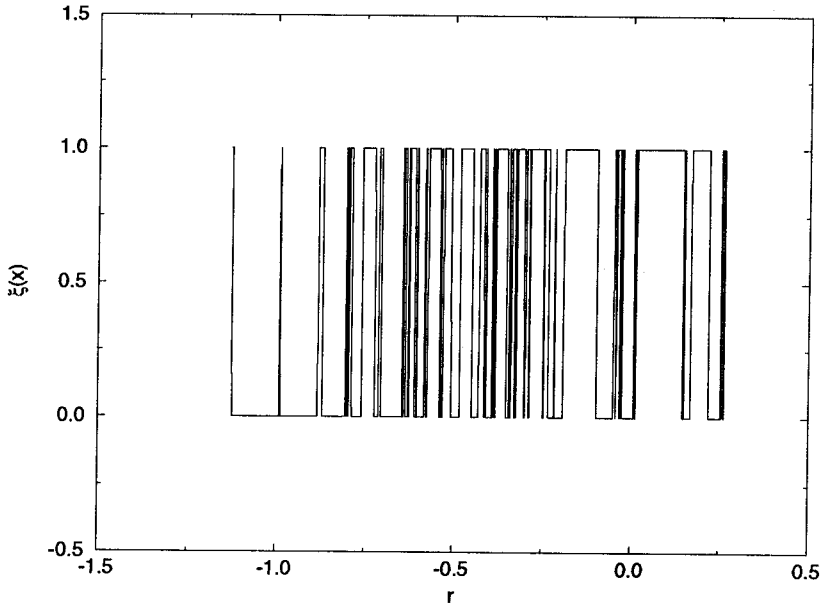

Figure 4.22: One-dimensional cut of interfacial line from $N = 150$, $\delta = .1$ N-vortex simulation at $y = 0$, $\xi(x)$ vs x

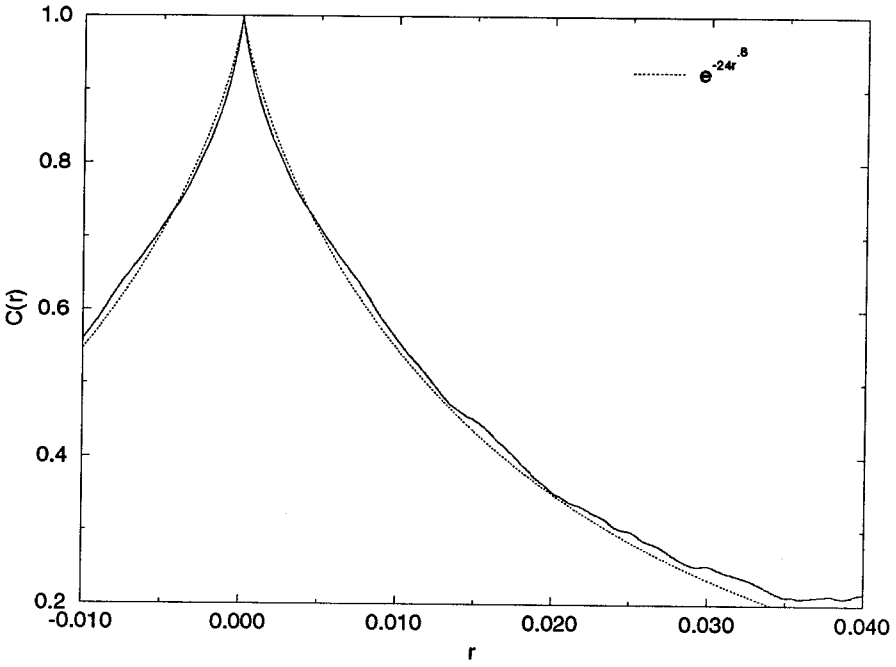

Figure 4.23: Autocorrelation of $\xi(x)$ for $N = 150,\ \delta = .1,\ C(r)$ vs r

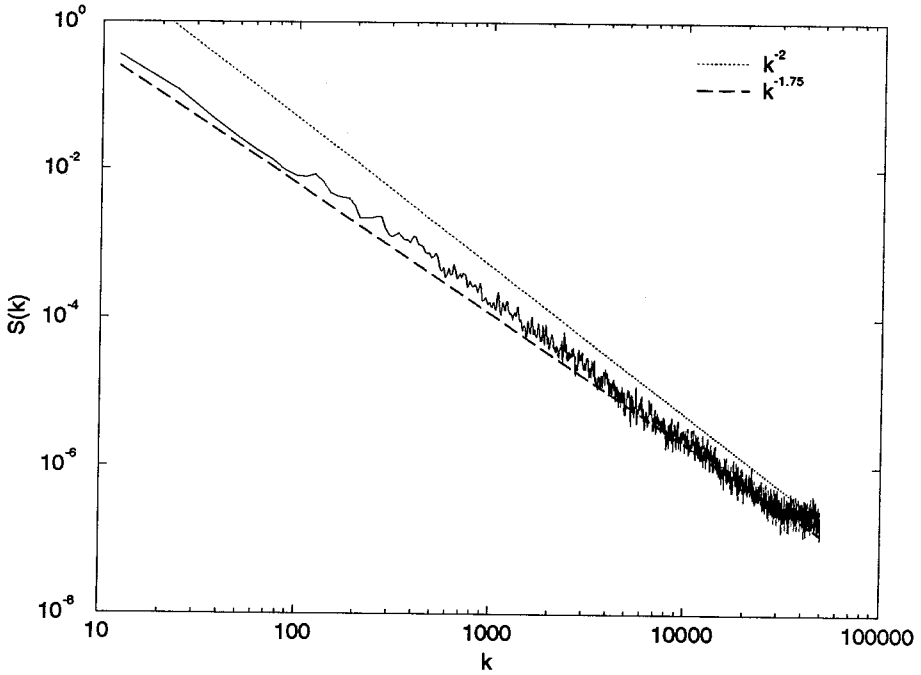

Figure 4.24: Scalar spectrum for $N = 150,\ \delta = .1,\ S(k)$ vs k

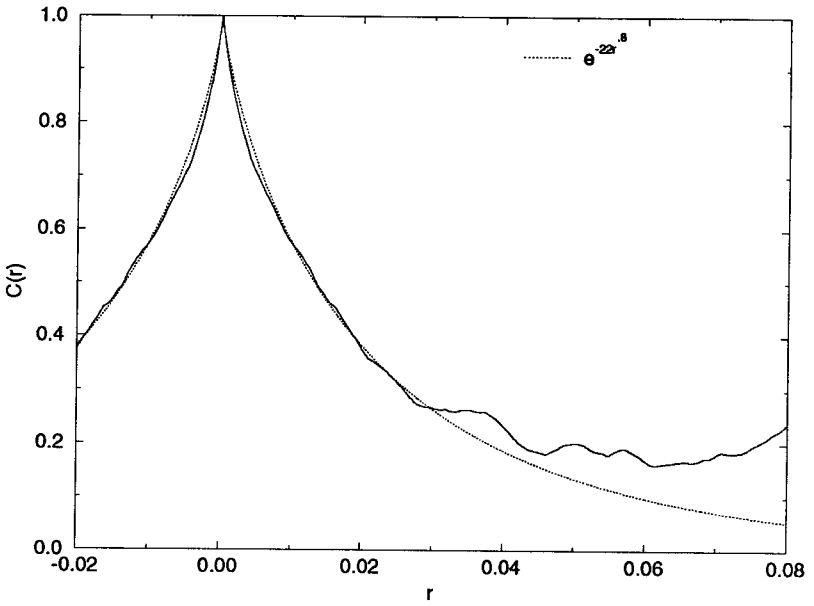

Figure 4.25: Autocorrelation of $\xi(x)$ from one-dimensional cut at $x = 0$ for $N = 150$, $\delta = .1$, $C(r)$ vs r

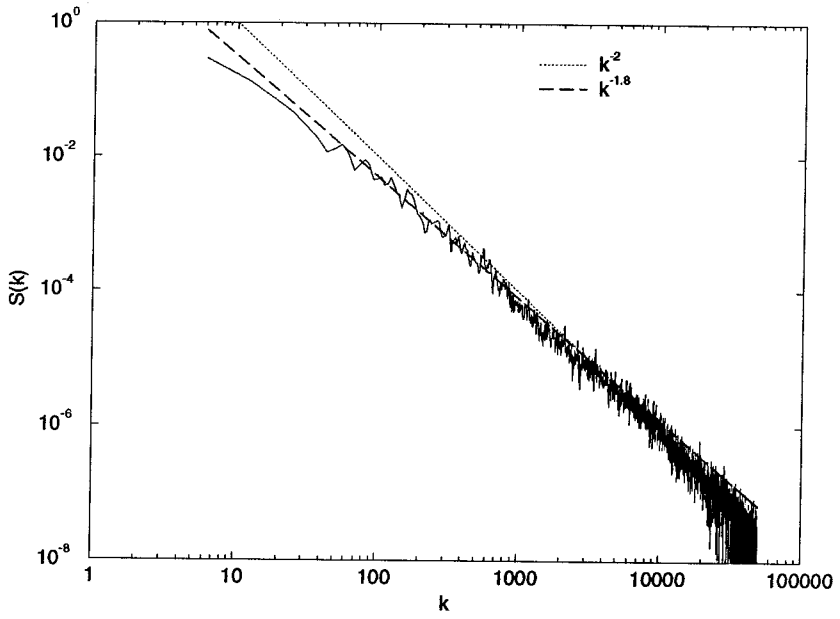

Figure 4.26: Scalar spectrum from one-dimensional cut at $x = 0$ for $N = 150, \delta = .1$, $S(k)$ vs k

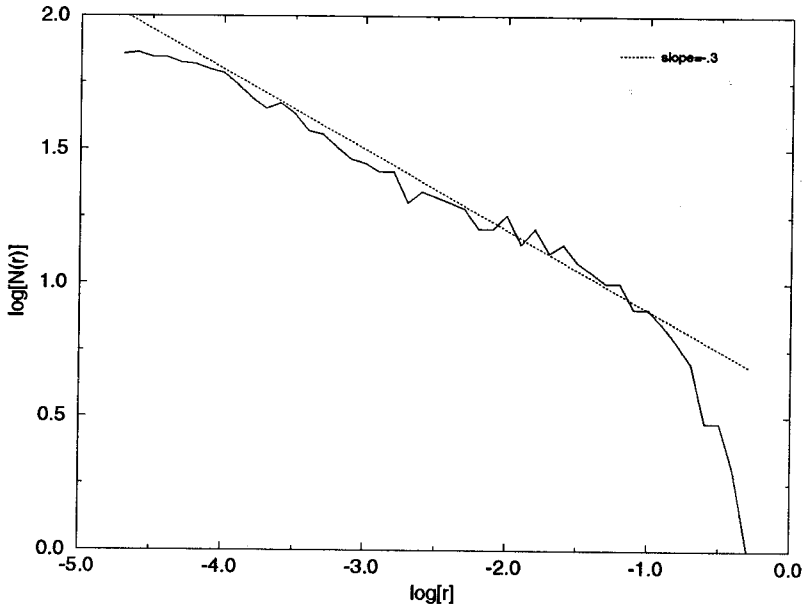

Figure 4.27: Box counting for one-dimensional fractal set, with $D = .3$, $\log N(r)$ vs $\log(r)$

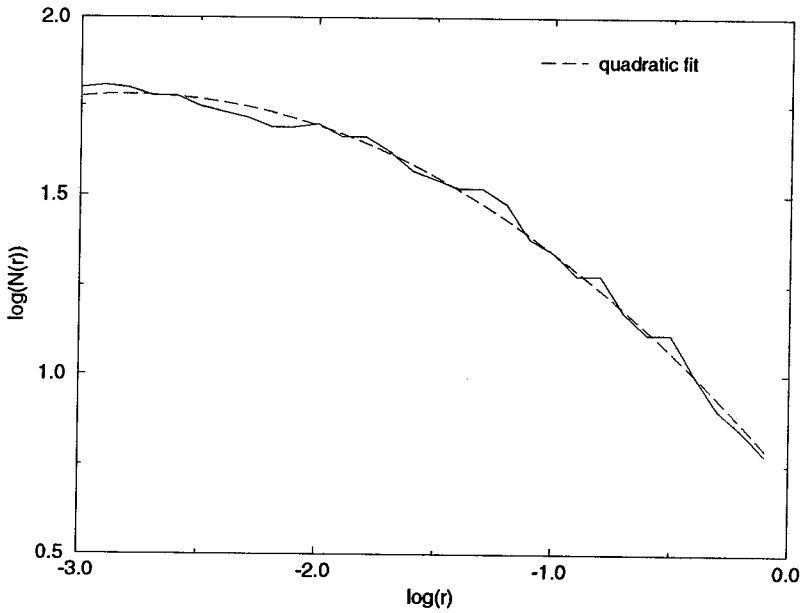

Figure 4.28: Box counting for one-dimensional cut of line from $N = 3, \delta = 1.0$ N-vortex simulation, $\log N(r)$ vs $\log(r)$

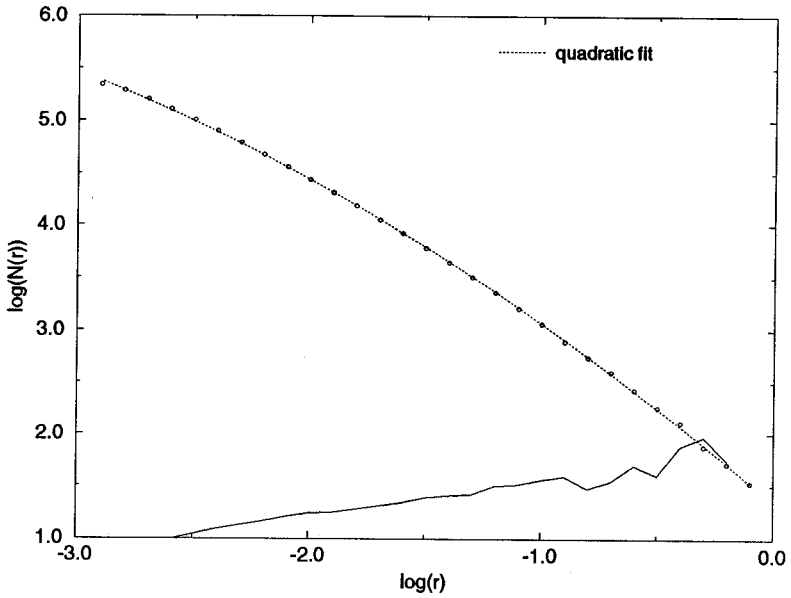

Figure 4.29: Two-dimensional box counting for line from $N = 3$, $\delta = 1.0$ N-vortex simulation, $\log N(r)$ and $\frac{d[\log N(r)]}{d[\log(r)]}$ vs $\log(r)$

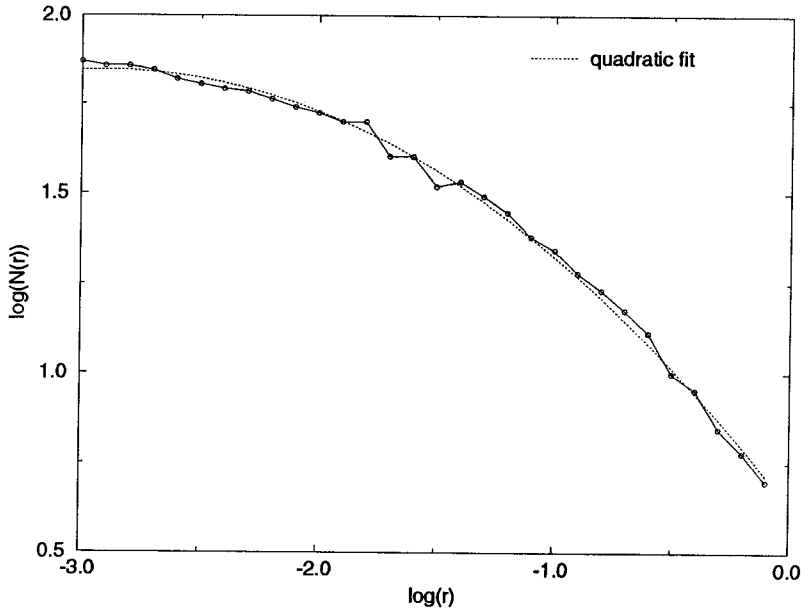

Figure 4.30: Box counting for one-dimensional cut of line from $N = 150, \delta = .5$ N-vortex simulation, $\log N(r)$ vs $\log(r)$

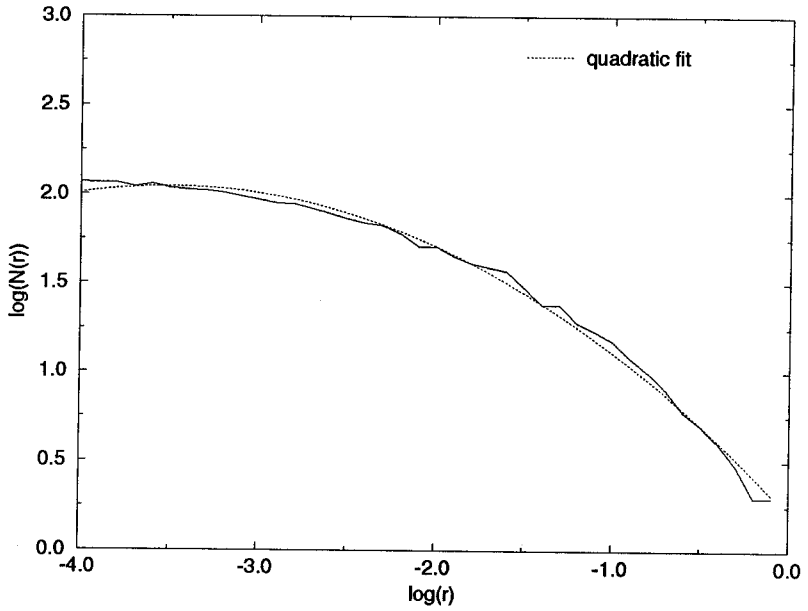

Figure 4.31: Box counting for one-dimensional cut of line from $N = 150, \delta = .1$ N-vortex simulation, $\log N(r)$ vs $\log(r)$

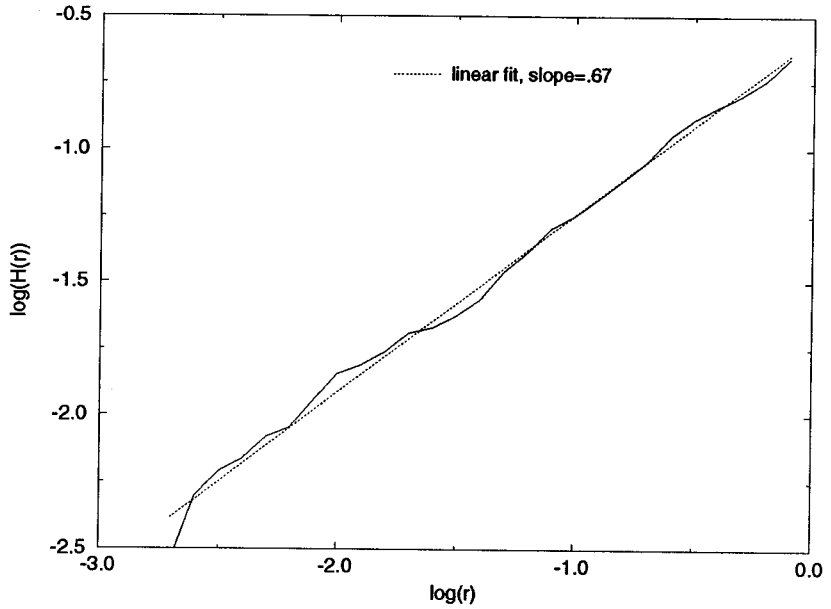

Figure 4.32: Correlation dimension for one-dimensional cut of line from $N = 3, \delta = 1.0$ N-vortex simulation, $\log H(r)$ vs $\log(r)$

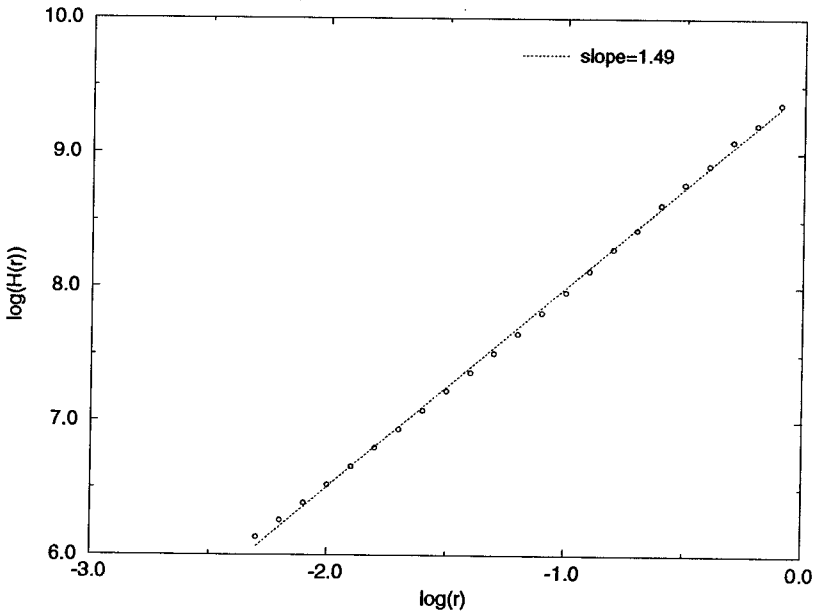

Figure 4.33: Correlation dimension from Two-dimensional box counting for line from $N = 3, \delta = 1.0$ N-vortex simulation, $\log H(r)$ vs $\log(r)$

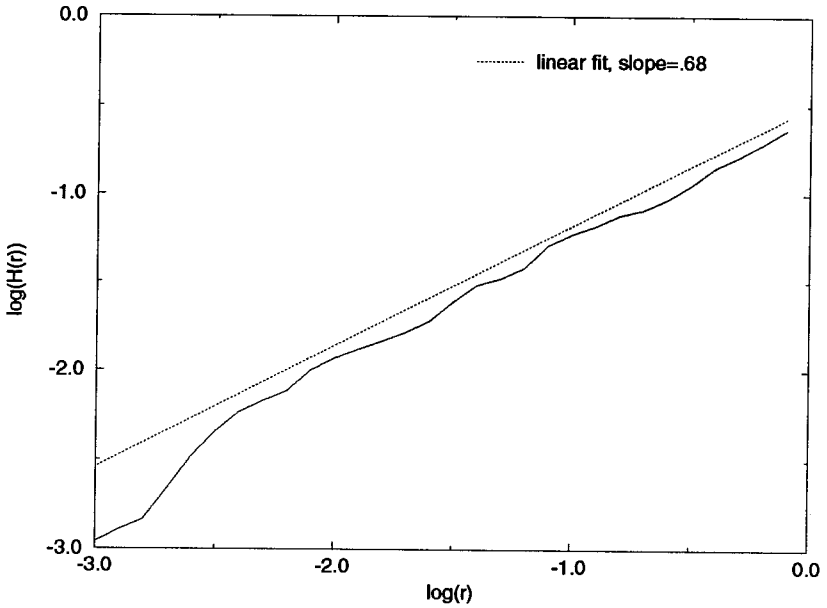

Figure 4.34: Correlation dimension for one-dimensional cut of line from $N = 150, \delta = .5$ N-vortex simulation, $\log H(r)$ vs $\log(r)$

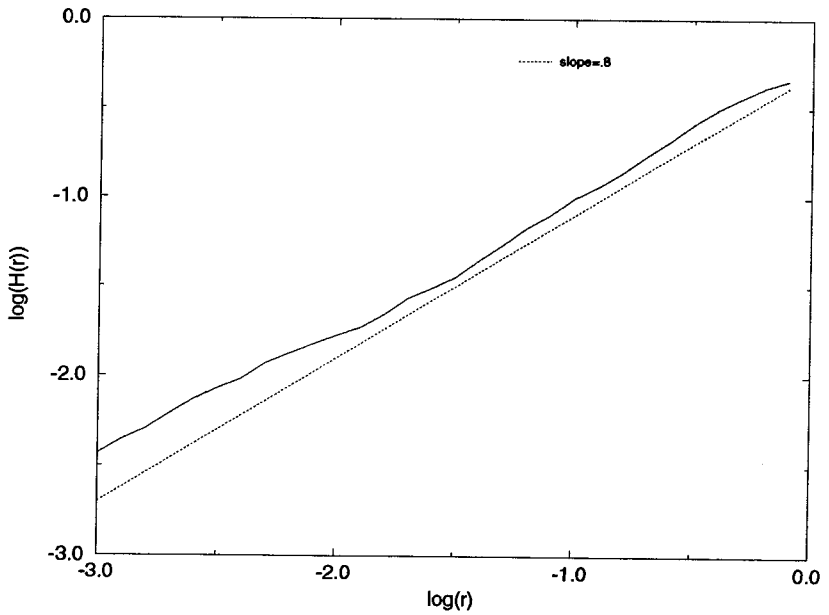

Figure 4.35: Correlation dimension for one-dimensional cut of line from $N = 150, \delta = .1$ N-vortex simulation, $\log H(r)$ vs $\log(r)$

Chapter 5

Two-Dimensional Mixing due to Rollup and Pairing of Vortex Structures in Shear Layers

5.1 Introduction

The planar shear layer has been the subject of extensive research in recent years, due in large part to the discovery of large scale organized vortices [20, 117]. The use of laser induced fluorescence in highlighting the scalar mixing has also brought about increased understanding of the transport and mixing process that are involved [61, 60]. The geometry of the entrainment, and subsequent stirring and mixing of the high speed and low speed fluid in the shear layer have been discussed in several papers (see [30, 45] for example).

Traditionally, the onset of turbulence is associated with an increase of the small scales, three dimensionality, and the existence of an inertial subrange. The role that the pairing of vortex structures plays in this development in the shear layer has been

well studied [47, 84, 85, 72, 28]. This development of fully developed turbulence has also been associated with the mixing transition, in which the molecular mixedness of two fluids initially separated by a splitter plate is found to increase drastically within some range of Reynolds numbers [62, 103]. The Reynolds number is defined as $Re = \Delta u \delta / \nu$, where δ is the width of the layer (which grows linearly with x) and Δu is the velocity difference across the splitter plate.

The role of pairing (merging) in mixing the fluid has been identified and tested by Huang and Ho [47] in experiments in the mixing layer where the existence of small scale turbulence and the accompanying -5/3 law region were correlated with the location of the mergings. The merging locations were varied with the use of external forcing to support this hypothesis. Other recent experiments have also served to highlight the development and evolution of the three-dimensional streamwise vortices and small scale flow field with novel flow visualization and data collection techniques [67, 88]. Numerically, Ashurst and Meiberg [8] have used three-dimensional vortex dynamics to simulate a shear layer to study the onset of streamwise vortices (no pairing though). Corcos and Lin [28], and more recently, Moser and Rogers [84],[85] among others have used numerical simulation to further study the three-dimensional evolution of the time developing shear layer, especially in regard to the role of vortex pairing in the development of the three-dimensionality and the mixing transition. The emphasis is on the breakdown of the organized three-dimensional (streamwise ribs and spanwise rollers) structures; i.e., on the dynamical evolution of vorticity and the creation of the small scales.

In this study we emphasize *scalar* mixing and show that it can reach significant levels even in the absence of small scale dynamics or three dimensionality. That is, mixing of the fluid can occur in the absence of what is traditionally thought of as full turbulence, and we demonstrate here the mechanism by which this happens.

It is particularly useful to study this as applied to the mixing transition, because it is precisely at about the transition Reynolds numbers that the large

scale two-dimensional vortical motions are dominant, before the advent of three-dimensionality. However, we do not make the claim that this is a viable alternative explanation for the mixing transition observed in experiments.

In this study we examine more closely the kinematic consequences of the mechanism of rollup and pairing of vortex structures on scalar mixing in two dimensions. The absence of three dimensionality allows us to gauge at least the minimum amount of mixing that can take place during pairing. Although previous studies have examined line stretching in chaotic flows (see Fung and Vassilicos [43, for example]), we propose to show its role in the scalar *mixing* as it applies to the physical problem of the shear layer by taking diffusion and diffusion layer overlap into consideration.

In his review of the mixing transition in shear layers, Roshko [103] has suggested chaotic advection as a possible route to the mixing transition process. In the sense that the eventual rapid increase of the interface is due to the vortex dynamics of a few relatively large structures (what we would call a low-dimensional dynamical system if we relate the number of vortex structures to the dimension of the system as discussed in section 1.2.2 of chapter 1), we find this to be likely. A part of the problem is that in the shear layer, we have to deal with a system that is dynamically changing — i.e., the Reynolds number continuously increases with time (in the Lagrangian frame, or distance in the Eulerian frame). The significance of the increasing Reynolds number being that the "dimensionality" of the problem changes with the Reynolds number, because the vorticity distribution is becoming more complex due to continuing vortex interactions. This makes connection to previous studies of chaotic advection at least semantically difficult.

Two models are used to illustrate the role of large scale two-dimensional structures in bringing about scalar mixing: the vortex sheet in a laterally periodic domain, and a new kinematical map that models the type of vortex interaction observed in a space developing shear layer. Using these models, the stretching and diffusion of the interfacial line dividing two fluids is tracked. Although initial interfacial line stretch-

ing is linear, we show exponential line stretching eventually occurs for more than two mergings, and that this can result in significant contribution to the evolution of the scalar mixing in the shear layer. In fact, the rapid increase of the computational difficulty associated with tracking the problem as the number of mergings increases should give us a hint as to the line stretching (interfacial area creation) properties of these two-dimensional large scale motion. Despite the exponential line stretching, good mixing requires a good spatial distribution of the interfacial line, otherwise concentration of the interface in a restricted region will leave other areas unmixed. This aspect of mixing, also known as mixing efficiency is also addressed.

5.2 The periodic vortex sheet

The equation of motion for the discretized periodic vortex sheet is as follows (see [66] and references therein for example)

$$\frac{dx_i}{dt} = \frac{-1}{2N} \sum_{j \neq i}^{N} \frac{\sinh 2\pi(y_i - y_j)}{\cosh 2\pi(y_i - y_j) - \cos 2\pi(x_i - x_j) + \delta^2} \tag{5.1}$$

$$\frac{dy_i}{dt} = \frac{1}{2N} \sum_{j \neq i}^{N} \frac{\sin 2\pi(y_i - y_j)}{\cosh 2\pi(y_i - y_j) - \cos 2\pi(x_i - x_j) + \delta^2} \tag{5.2}$$

where δ is the de-singularizing vortex core parameter. The distances between the points (x_i, y_i) are 'small' to simulate a continuous sheet. These equations are solved using the Lagrangian vortex method. The evolution of the above equations depends on the initial positions (x_i, y_i) and δ. The initial conditions are set with a sinusoidal perturbation and as many of its subharmonics as the number of mergings. These perturbations amplify, rollup, and then eventually merge. A drawback of this model is that the problem is ill-posed without the de-singularizing factor δ, and there is no clear correspondence between the results of this model and the solutions of the Euler or Navier-Stokes equations. Therefore it should be understood that this method is

used as model, and not as a dynamically accurate solution of the fluid dynamics. The type of systematic study by Tryggvason et al. [110] in relating the de-singularizing parameter δ with the initial thickness of the layer and the Reynolds number for a Navier-Stokes solution is useful in the modeling regard, although establishing a rigorous connection appears hopeless, since δ dimensionally and dynamically does not behave like viscosity. We chose this Lagrangian method because the vortex sheet coincides with the material interface, and no separate computation is required for the evolution of the interface between the two fluids.

The periodic vortex sheet has recently been extensively studied numerically by Krasny [66] using the vortex method. Other numerical studies have been made of this problem, many of them in three dimensions, including those by Sherman and Corcos [27], Jacobs and Pullin [52], Riley and Metcalf [101], Lesieur et al. [72] and Moser and Rogers [84][85]. It is popular as a model for the space developing shear layer because of its simplified boundary conditions. Pairing between adjacent vortex 'structures' were observed in these simulations and related to similar occurrences in the space developing case. With the current numerical experiments, we track the increase of the two-dimensional interfacial length when the only significant dynamic event occurring in the flow is the two-dimensional rollup and the merge process. This is done up to three pairings which is sufficient to provide large increases in the material interface. Thus we isolate the mechanism that is central to the two-dimensional, large scale evolution of the shear layer.

For computational accuracy (and efficiency), vortex particles are inserted during the simulation on an as-needed basis — that is, when the separation between neighboring particles becomes greater than the parameter δs_{max}, a new particle is inserted, with the appropriate sharing of the circulation strength and history of stretching, etc. The parameters L and ΔU are used to to normalize the length and the time (by $L/\Delta U$) scales in this computation. As mentioned above, the vortex sheet computation using Lagrangian vortex blob method does not solve the Navier-

Stokes equation, but can be used as a model to match the NS solutions using the appropriate value of δ [110]. This requires a rather artificial matching of the Re to the simulation, but can be managed by comparing vortex structure merging locations (times). The non-dimensionalized diffusivity D and stretch exponent λ are scaled as $D^* = D/(\Delta UL)$ and $\lambda^* = \lambda L/\Delta U$, but we drop the asterisk henceforth for convenience.

5.2.1 Measuring mixing

Since the flow carries fluids $\mathcal{A}$ and $\mathcal{B}$ on either side of the interface, the mixing between the two fluids can be characterized by the spatial distribution of the interfacial layer across which molecular diffusion takes place. Assuming no overlap of the diffusion layers, mixing can be quantified roughly by the fraction

$$\frac{A_m}{A} = \frac{\sum_{i=1}^{N} L_i(t) d_i(t)}{A(t)} \tag{5.3}$$

where the interfacial line has been divided into N segments, with L_i the length of the ith segment and d_i the thickness of its diffusion zone. We make use of a decomposition and transformation often used in the past to compute $d_i(t)$ — see Ottino [91], Marble [77], Karagozian and Marble [56], Leonard et al. [71], Dimotakis [31], and references therein. This method consists of approximating the two-dimensional convection-diffusion equation by a one-dimensional, local, Lagrangian equation, and then using a time-dependent transformation to arrive at a one-dimensional, local, Lagrangian diffusion equation that depends on the local value of the strain and strain history. The full two-dimensional convection-diffusion equation for the transport of a scalar ξ is

$$\frac{\partial \xi}{\partial t} + \mathbf{u} \cdot \nabla \xi = D \nabla^2 \xi. \tag{5.4}$$

This equation can be locally decomposed into x and y components, which are the directions tangent to, and normal to the interfacial line respectively. Assuming that

the local gradients are negligible in the tangential direction, we are left with a one-dimensional approximation in the normal direction. This assumption breaks down in regions of high curvature (the numerical data on the curvature of the vortex sheet is presented in section 5.2.2). In this normal direction which is defined locally for a material segment that is in a translating and rotating frame of reference, v can be approximated by $-\epsilon y$ (by keeping the first term of the Taylor series expansion), where ϵ is the time dependent local strain $\partial v/\partial y$,

$$\frac{\partial \xi}{\partial t} - \epsilon y \frac{\partial \xi}{\partial y} = D \frac{\partial^2 \xi}{\partial y^2} \ . \tag{5.5}$$

Using the following strain and time-dependent transformation (see references mentioned above),

$$\bar{y} = Sy \tag{5.6}$$

$$\tau = \int_0^t S^2(t')dt' \tag{5.7}$$

$$S(t) = \frac{\delta L(t)}{\delta L(0)} = e^{\int_0^t \epsilon(t')dt'} \ , \tag{5.8}$$

we have the diffusion equation

$$\frac{\partial \xi}{\partial \tau} = D \frac{\partial^2 \xi}{\partial \bar{y}^2} \tag{5.9}$$

with the well-known solution

$$\xi(y,t) = \frac{1}{2}\left[1 + \mathrm{erf}\left(\frac{Sy}{\sqrt{4D\tau}}\right)\right] \ . \tag{5.10}$$

If we assume that a value of $\xi = .9$ constitutes sufficient mixedness of the interfacial zone (or the product zone if we consider the reaction between fluids $\mathcal{A}$ and $\mathcal{B}$), then d, the thickness of this zone can be expressed as

$$d(t) = \frac{\sqrt{4D\tau}\mathrm{erf}^{-1}(.8)}{S} \approx \frac{\sqrt{4D\tau}}{S} \tag{5.11}$$

for each individual segment.

As a check on the model, we can perform a rough estimate of the expected thickness of the interfacial layer in the following way. If we assume that the straining experienced by a Lagrangian point is constant, ($\epsilon \approx$ constant)

$$S(t) \approx e^{\epsilon t} \tag{5.12}$$

$$\tau(t) \approx \int_0^t e^{2\epsilon t'} dt' = \frac{e^{2\epsilon t} - 1}{2\epsilon} \tag{5.13}$$

$$d(t;\epsilon) \approx e^{-\epsilon t} \sqrt{\frac{4D(e^{2\epsilon t} - 1)}{2\epsilon}} \tag{5.14}$$

expanding about $t = 0$,

$$d(t;\epsilon) \approx d(t) = \sqrt{4Dt} \tag{5.15}$$

for small t, and

$$d(t;\epsilon) \approx d_\infty(\epsilon) = \sqrt{\frac{2D}{\epsilon}} \tag{5.16}$$

for large t as expected [31],[53]. Note that for large t, the value of $d = d_\infty(\epsilon)$ is independent of time and depends just on the strain ϵ and the diffusivity D. So without the overlap of diffusion layers, the mixed area fraction is given by $L(t)d_\infty(\epsilon)/A(t)$. A rough numerical example is illustrative. Starting with an interfacial line of length $L(0) = 1$, and assuming no overlap, $A_m(t) \approx \sqrt{2D/\epsilon}e^{\epsilon t}$. Then we assume $\epsilon \approx 2$ (based on numerical experiments to be discussed below), and if $D = 10^{-6}$, then $A_m(t) = 10^{-3}e^{2t}$. So at $t \approx 3.5$, $A_m = A = 1$. This increase in mixed area is kept in check by two factors — the overlap of mixed layers and the continual entrainment of fresh fluid (A then grows with t), and hence the plateau or saturation of the mixed fraction seen in Figure 2 of Roshko [103] beyond the mixing transition.

Accounting for the diffusion zone overlap is numerically more difficult in the Lagrangian scheme. Beigie et al. [13] have considered a problem of this sort to propose the idea of mixing efficiency, in which the idea that apart from the stretch rates, the *spatial distribution* of the stretching is also important in measuring mixing. This is particularly important in the problem of the shear layer at hand, where large

amounts of fresh fluid is continuously entrained, squeezing the rest of the mixed fluid together, until they too are brought together by even newer entrained fluid. Computationally, the fraction of the mixed fluid may be measured by constructing an Eulerian mesh on top of the Lagrangian interfacial layer, and counting the occupied cells. The calculation of the fraction $A_m(t)/A(t)$ must also take into consideration the fact that $A(t)$ also grows with time. In the space developing shear layer $A(t)$ is related to the 'vertical' and 'lateral' extent of the layer that grows linearly with x. In our computations we take $A(t) \sim |y_{max}(t)|^2$, where $|y_{max}(t)|$ is the maximum width of the vortex structure at t.

5.2.2 Numerical results

We first demonstrate the numerical algorithm on a single rollup of the vortex sheet. The state of the interfacial vortex sheet at $t = 3.0$ is shown in Figure 5.1. Figure 5.2 shows the diffusion layer for $D = 10^{-5}$. The stretch rate for the entire sheet is shown in Figure 5.3. Note the eventual linear growth of the line length. Figure 5.4 shows different stages of the evolution of the vortex sheet with one subharmonic which results in one pairing. Similarly, Figure 5.5 shows a vortex sheet undergoing two pairings, and Figure 5.6 three pairings. Figure 5.7 shows the vorticity sheet evolution for three pairings with different initial perturbations. A visual comparison of the state of the diffusive interface of experimental flow images from high Schmidt number shear layers [60, 61] with Figures 5.6 and 5.13) hint at underlying similarities in the generating mechanism. The relative vortex sheet lengths are compared in Figure 5.8 for different pairings. The amount of rollup between pairings is controlled by the amplitudes of the initial subharmonic perturbations, and the de-singularizing parameter δ. It is clear that with more roll up the line stretching will increase, and this is reflected in Figure 5.9 in which the line length of two runs with different initial subharmonic perturbations (Figures 5.6 and 5.7) are plotted. If we express

the exponential line length growth as

$$L(t) \sim e^{\beta t} , \tag{5.17}$$

then the line length exponent (β) for Figure 5.9 is around 1. When non-dimensionalized, this translates to $\beta\delta/\Delta U$, although it is not certain whether the quantity β is easily measurable in the laboratory. One obvious consequence of exponential line growth is the increasing computational cost of maintaining the resolution. For example, for a line length $L = 20$, maintaining an inter-vortex distance on the vortex sheet of 0.01 requires 2000 vortex elements, which is a sizeable computational challenge in itself, but the situation rapidly becomes more difficult. If we assume $\beta = 1.0$, then the number of vortices doubles after every $\Delta t = .7$, and considering the N^2 algorithm we use, the simulation cannot be performed for very long. Thus we have compromised the fine scale resolution of the vortex sheet evolution in our simulations in order to run to longer times and observe the exponential line stretching. The details of the dynamics may suffer, and the stretching will be undercounted somewhat, but we believe the overall behavior of the system has been captured. In addition, the presence of diffusion ensures mixing of the smallest scales so that the resolution of the vortex sheet for purposes of measuring mixing are not critical. The computational problem is not quite as severe in the interfacial line simulation of chapter 4 because the line elements are passive. This is one of the reasons that has lead us to the developmen of the kinematic model described in the next section.

As mentioned before, the mixedness is estimated by the area covered by the interfacial layer, and to avoid double-counting when these layers overlap, the covered area is calculated from an Eulerian grid. This saturation is demonstrated in Figure 5.10 which plots the mixed area measured from a Lagrangian viewpoint without regard to overlap (by summing the length times the thickness of each line segment), and from an Eulerian viewpoint (by summing the boxes that are covered). The mix-

ing transition in shear layers is viewed by plotting the mixed area fraction (δ_m/δ) against the Reynolds number (see Figure 2 of Roshko [103]). A comparable version of that plot for the current problem is shown in Figures 5.11 and 5.12 where we plot the mixed area fraction as a function of time instead of the Reynolds number . (The evolution in time for our problem is similar to the downstream movement of the vortex structures which results in approximately linear increase of the Reynolds number). The mixed area at any time is normalized by the area of the local shear layer at that time to calculate the mixed fraction. In the physical problem, we assume this local area to be roughly determined by the maximum width ($\delta_w(x)$) of the shear layer.

Figure 5.12 is included to show that the 'sudden' increase in mixedness is a relative thing due to the fact that on a log-linear plot, the x-axis can be compressed quite a bit. In fact the transition Reynolds number ranges from around 3,000 - 10,000 during which the width of the shear layer can triple, from the beginning of the transition to the end of the transition. However, as pointed out by Dimotakis [35], our numerical simulation, and those by others involve looking at mixing for a single vortex structure, while experimental measurements are performed over an ensemble average of many vortex structures. This leads to a smoothing of the range over which the transition appears to take place. Experimental observations show that the mixing transition for *individual* vortices are quite sudden (due to three-dimensionality and small scales).

Figure 5.13 shows the diffusive layer that defines the mixedness for Figures 5.11 and 5.12. Since each segment of the interfacial line undergoes different strain rates, each segment ends up with a different diffusive layer thickness $d(i)$. This is shown in Figure 5.14 where the thickness (d_i) distribution is plotted at two different times during the sheet evolution (we have ignored thicknesses in the extremely high curvature regions, since the one-dimensional model breaks down, and the thicknesses are not accurately represented). For comparison, the dotted horizontal lines represent-

ing the thickness that a sheet would achieve in the absence of strain ($d = \sqrt{4Dt}$) is also plotted at each time. A similar plot of the distribution of the stretch exponent values ($\lambda_i = \frac{1}{t}\log(L_i/L_i(0))$) associated with each segment of the sheet is plotted in Figure 5.15. These are just the finite time Lyapunov exponents for the particles on the interfacial sheet, and the fact that they are mostly positive is an indicator of the chaotic nature of the flow. The probability density function (PDF) for the distribution of stretching is computed and plotted in Figure 5.16 along with a Gaussian function. Although not directly germane to the issues raised in this chapter, this information may be of interest in that some recent studies have tried to determine whether the tails of the PDF of stretchings in turbulent and non-turbulent chaotic flows are Gaussian or not. It is interesting to note that the shape of the PDF is similar to that seen in chapter 3.

The curvature of a line at any point is defined to be

$$\kappa = \frac{|d^2y/dx^2|}{[1 + (dy/dx)^2]^{3/2}} \,. \tag{5.18}$$

This quantity is evaluated along the vortex sheet shown in Figure 5.6(f). Figure 5.17 shows κ plotted as a function of the index i. Note that there are only a few points at which κ exceeds the value of 100. This is better illustrated in Figure 5.18 which shows the probability density function of the curvature distribution. The radius of curvature $\rho = 1/\kappa$ then gives us a length scale that we can compare to the diffusion layer thickness of Figure 5.14, or the striation thickness between neighboring vortex sheet lines.

5.3 The rollup-merge map

We introduce the rollup-merge (RM) map which exemplifies the type of large scale two-dimensional behavior that occurs in the shear layer (namely the rollup - rep-

resented by a twist map, and merging - represented by a shift map). These two dynamic events form the main two-dimensional dynamics on the scalar interface, and thus on mixing. In this regard, this model is similar to previously proposed kinematic models such as the tendril-whorl flow or the blinking vortex map (see Ottino [92] or Aref [3] for description). In dealing with fluid mixing by separating the action of the large scale stirring and small scale diffusion, our model is also similar in spirit to the work of Kerstein [57, 58] whose linear-eddy modeling of turbulent transport was developed as a means of addressing flows where a wide range of scales must be resolved. In this scheme, the spatial development of the flow (convection) is represented by a stochastic simulation of a one-dimensional line element (random rearrangement), and local molecular mixing by Fickian diffusion. In our model, the large scale stirring is provided by the the rollup-merge mechanism rather than random rearrangement.

The RM map consists of two mappings, one the (integrable) twist mapping

$$r_{n+1} = r_n \tag{5.19}$$

$$\theta_{n+1} = \theta_n + a r_n \tag{5.20}$$

and a shift mapping

$$x'_{n+1} = x_{n+1} \tag{5.21}$$

$$y'_{n+1} = y_{n+1} \pm s_{n+1} \ . \tag{5.22}$$

The two parameters are the twist parameter a, and the shift parameter s which varies with n in order to follow the spatial growth found in the space developing shear layer. A necessary condition that the time scale also grow linearly with the spatial scale is also imposed. This is so that the dynamics remain consistent and self similar, as found approximately in the physical flow.

Figure 5.19 shows the sequence of effects that each step of the mapping has on a

line of passive markers. Also included is a shear mapping ($x_{n+1} = x_n + b; y_{n+1} = y_n$) that makes the modeling closer to that of a shear layer, but otherwise is not dynamically significant. The twist map stretches the line out into the θ direction, and if the parameter a is large enough, turns it into a spiral (see Figure 5.19(b)). Then the shear mapping skews it (Figure 5.19(c)), and in order to model the merging process, the line is shifted up (Figure 5.19(d)). This is because during vortex mergings, it is found that the center of rotation is shifted from the center of a single vortex to the common point between the two vortices. There is a further action of duplicating the existing structure and placing it shifted down as the 'neighboring vortex structure' is merged together (Figure 5.19(e)). The whole process is then repeated, the first step of which is shown in Figure 5.19(f).

The generation of the interfacial line, diffusion layer, and measurements of mixing are done in a manner similar to the periodic vortex model discussed in this chapter. Since the current model is a kinematical mapping, the computational costs are far lower and we have isolated the essential components of the vortical motion to its simplest form. The map introduced in this study is quite similar to the many predecessors such as the tendril-whorl map [92], the blinking vortex map [92, 3], etc., and it is to be expected that the trajectory of a particle in this mapping is also chaotic (for the proper parameters). This can be shown by the existence of positive Lyapunov exponents, or by construction of a horseshoe generating sequence. Another new aspect here is that the time scale is not constant. This is a requirement levied by the geometry of the physical problem of the shear layer we are trying to model.

5.3.1 Numerical results

Figure 5.20 shows the sequence of time evolution of an interfacial line through the RM mapping for the parameter $a = 15$. The duplication step has been left out to illustrate the evolution of a single line segment. Figure 5.21 shows an interface

produced with the duplication step. Physically, the duplication is needed because a pairing involves two similar structures. The generation of fine scaled striations is evident in these pictures. Figure 5.22 shows the line length increase as a function of n. Note that the n steps are not linear, but double every step. In a manner similar to the vortex sheet example, we also keep track of the stretch rates experienced by individual line segments and use that to determine the diffusive layer thickness to estimate mixing. An example of this is shown in Figure 5.23 for $D = 10^{-5}$. Figure 5.24 shows the mixed area and Figures 5.25 and 5.26 show the mixed area fraction. The mixed area fraction plots should be compared to the mixing transition plot (Figure 2 of [103]). Figures 5.27,5.28, and 5.29 show the results of computations for a much large value of $D = 10^{-3}$.

5.4 Discussion

5.4.1 Mixing transition and chaotic advection

Several models that produce chaotic particle motion [3][92][12] have been studied in the past , and the connection to mixing of fluids has been made. The question of the relationship between shear layer mixing and chaotic advection has also previously been brought up by Broadwell and Mungal [19]. They point to the similarities in the increased mixedness associated with non-integrable (chaotic) flows and in the shear layer, and speculate that mixing transition occurs where the Taylor layers overlap. (The Taylor layer refers to diffusive scalar thickness around the interface that must scale as $\sim \delta/(ReSc)^{1/2}$). In this study we wish to clarify the connection between chaotic advection and the physical problem of mixing in the shear layer. Because of the continuous increase of the Reynolds number and the associated increase in the small scale and three-dimensional activity in the developing region of the shear layer, the assignment of a single 'cause' of mixing has been difficult. We will isolate

and point out the role that chaotic advection plays through the two-dimensional large scale motion described in previous sections.

Mixing is related to chaotic particle trajectories through the exponential stretching of interfacial lines. As discussed in section 2.3, the stretching exponent λ for each line segment is the finite time Lyapunov exponent. The variation seen in the distribution of these values for line segments is reflective of different stretching that each segment is subjected to. These values nonetheless are mostly positive for the models under consideration, and indicate exponential separation of particles that are close together. This is of course reflected in the nearly exponential line stretching observed in Figures 5.8 and 5.9 The important role that exponential line stretching plays in fluid mixing has already been made, so we will proceed to examine the mechanism behind it.

The exponential stretching of the interfacial lines are produced only with the presence of both the merging *and* the rollup. The rollup motion by itself cannot sustain large stretching without realignment of the lines. That is, the rate of stretching in a purely rollup motion is linear. The reason why exponential stretching occurs for the combination of the rollup and merge process can be illustrated by first examining the rollup process. Rollup occurs when $u_\theta \approx u_\theta(r)$ (except for solid body rotation), and $u_r \approx 0$. Although there is rapid initial separation of particles that have different r, this difference is not increased with time and so the stretching of lines is soon linear. The role of the merging process is to shift the lines' position with respect to the center of rotation, so that there is effectively a reorientation of the relative positions of the particles. This continual reorientation allows two nearby particles to always experience a velocity difference, causing continual line growth. This also highlights the fact that line length can grow exponentially even in a flow that is not extentional (real eigenvalues for the velocity gradient tensor). Shear dominated flows with sufficient perturbation provides ample means for exponential line stretching. This is the key mechanism that occurs in the large scale for the

shear layer (and more generally in other turbulent flows such as the round jet).

The realignment mechanisms in other chaotic models have been varied. They include external perturbation (oscillating vortex-pair) and blinking (turning vortices on and off) among others. The observation we make is that the *natural* motion of vortices involves rotation about some common central point, and that there is sufficient fluctuation of the flow field induced by the motion of these vortices such that there is constant realignment. We propose that the distribution of vorticity in the transition regime of the shear layer is such that it falls under this type of stretching mechanism.

The exponential stretching of material lines resulting from the existence of chaotic advection is quite clear. The mostly rotational behavior of vortical structures is easily observed, and the interaction of like-signed vortices resulting in rotation about their common center is also evident. The effect of three-dimensional and small scale motion within the large scale vortex structures would, of course greatly affect the mixing situation so as to overtake the effect of the large scale motion. This is why the role of the large scales in mixing is being discussed in the context of the low Reynolds number regime where the three-dimensional, streamwise vortical structures have not yet been fully developed. Indeed, it is likely that the large scale motion under current discussion may have a lot to do with the *creation* of the small scales and three-dimensionality.

5.4.2 Comparison to experiments

As the Reynolds number increases downstream in experiments, turbulence is further developed in the form of greater three-dimensional and small scale effects. At the same time, two-dimensional mixing is also advancing in the form of rollup and pairing of the spanwise large scale structures. So in a sense, it is a competitive process between the different mechanisms. It is however, a competition that the large

scale, two-dimensional mechanism will very likely lose, because small scale, three dimensional mixing is far more rapid, and the large scale motion is at least partly responsible for the development of the small scales and the three-dimensionality. However, in considering the problem of mixing of two fluids, it must be remembered that the large scale motion plays the crucial role of transporting the interface around, and bringing fresh fluid together. Without this, the small scales will cause lots of mixing amongst fluid of the same kind, without necessarily promoting mixing *between* the two fluids.

Therefore, associating the two-dimensional, large scale motion with chaotic advection, mixing transition can be thought of as being brought about by, or helped along by chaotic advection. However, chaotic advection is usually associated with a low order dynamical system that does not change its dimension. The shear layer is far more complex, moving from low Reynolds number to turbulent regimes with very high Reynolds number, so that the dimensionality (in the sense of n-dimensional dynamical system) of the problem changes with time. Even in the pre-transition regime (perhaps especially in this regime), the dynamical system is changing, so while it is the canonical stretch and fold chaos producing mechanism that may be responsible for bringing about the mixing transition (and indeed the turbulent transition), it is the rather more general transition from a low dimensional system to a higher one that we see here.

In regards to whether it is possible to have the mixing transition occur in a purely two-dimensional shear flow, taking into account the fact that mixing transition is quite loosely defined, it certainly appears possible, as indicated in Figure 5.12. In the non-ideal three-dimensional experiment though, mixing will develop faster with the participation of the three dimensionality, and thus display a different character in terms of the route to a mixed state. We note that Dimotakis [35] has conducted an experimental investigation of a two-dimensional soap film shear layer, where a rapid increase in the mixing was observed at some point in the evolution. One important

aspect of the dynamics that is missing in our current studies is the mixing mechanism due to the interaction of vortices of different signs. In addition to the rollup and pairing, there can also be a translational movement that enhances transport in a different way from that discussed in this thesis.

At about the transitional Reynolds numbers, the emergence of the small scales and the three dimensionality coincide with the increasing mixing capabilities due to the two-dimensional vorticity distribution becoming more complex. In the shear layer, it is not possible to hold the flow at a fixed transition Reynolds number because the Reynolds number grows continuously with x. However, if we envision a situation (such as in a round jet, or a plane wake) where the Reynolds number can be held fixed, we would be able to tell if full mixing can be achieved by turbulence that is not fully developed. The flow in a round jet however, is more three-dimensional than the shear layer to begin with, so the role of two-dimensional, large scale mixing is even harder to detect.

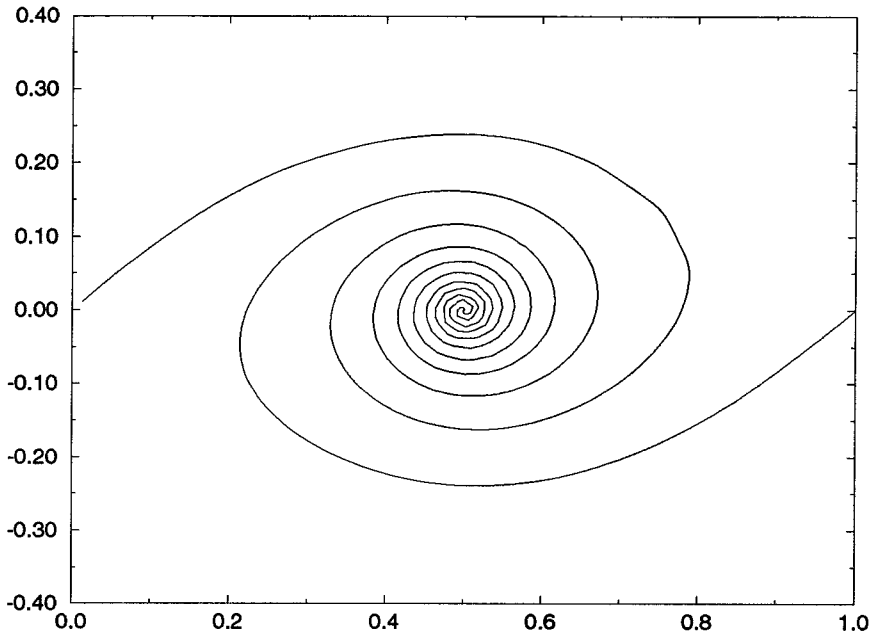

Figure 5.1: Periodic vortex sheet evolution for $\delta = .2$, at $t = 3$

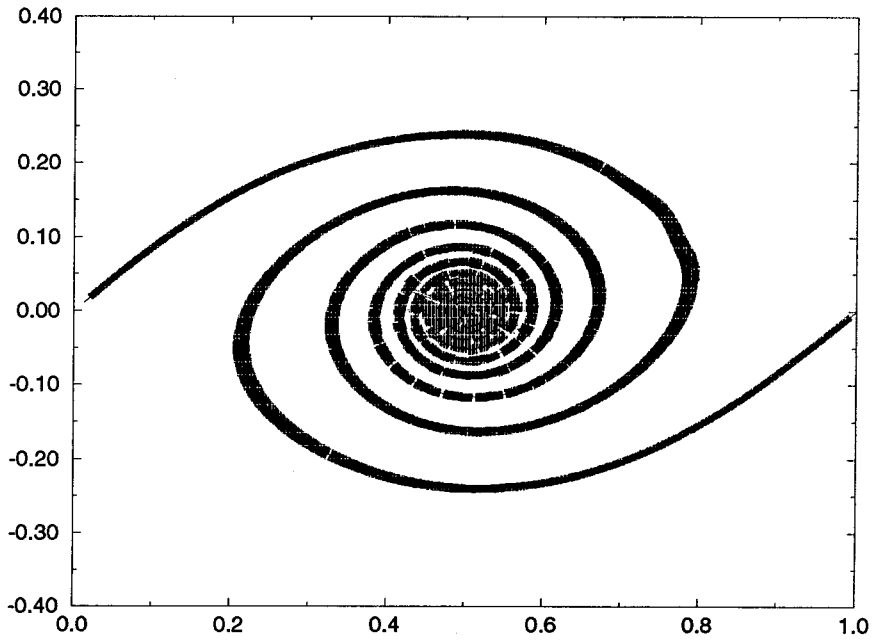

Figure 5.2: Periodic vortex sheet evolution with diffusion layer for $\delta = .2, D = 10^{-5}$

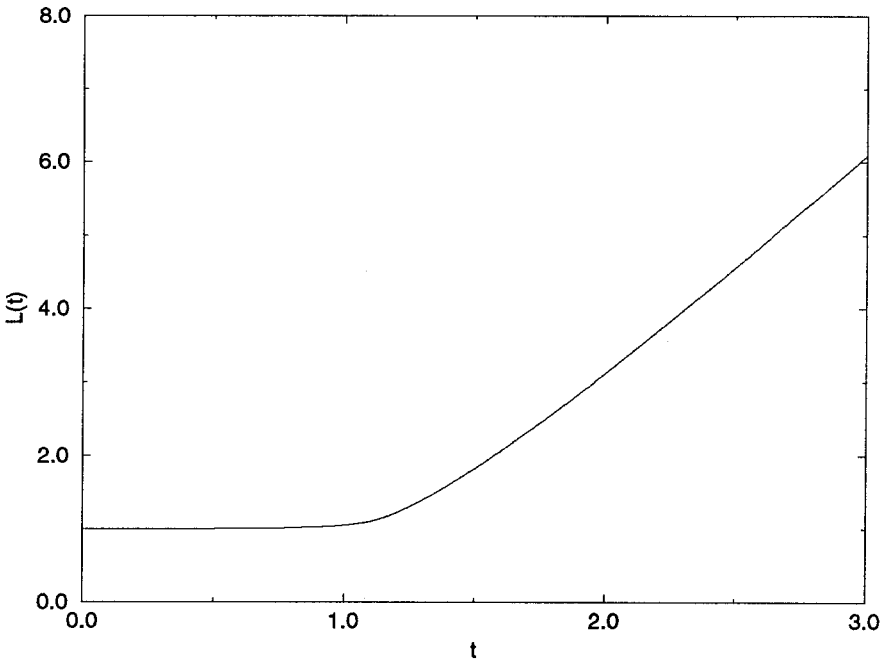

Figure 5.3: Vortex sheet length for single rollup, $L(t)$ vs t

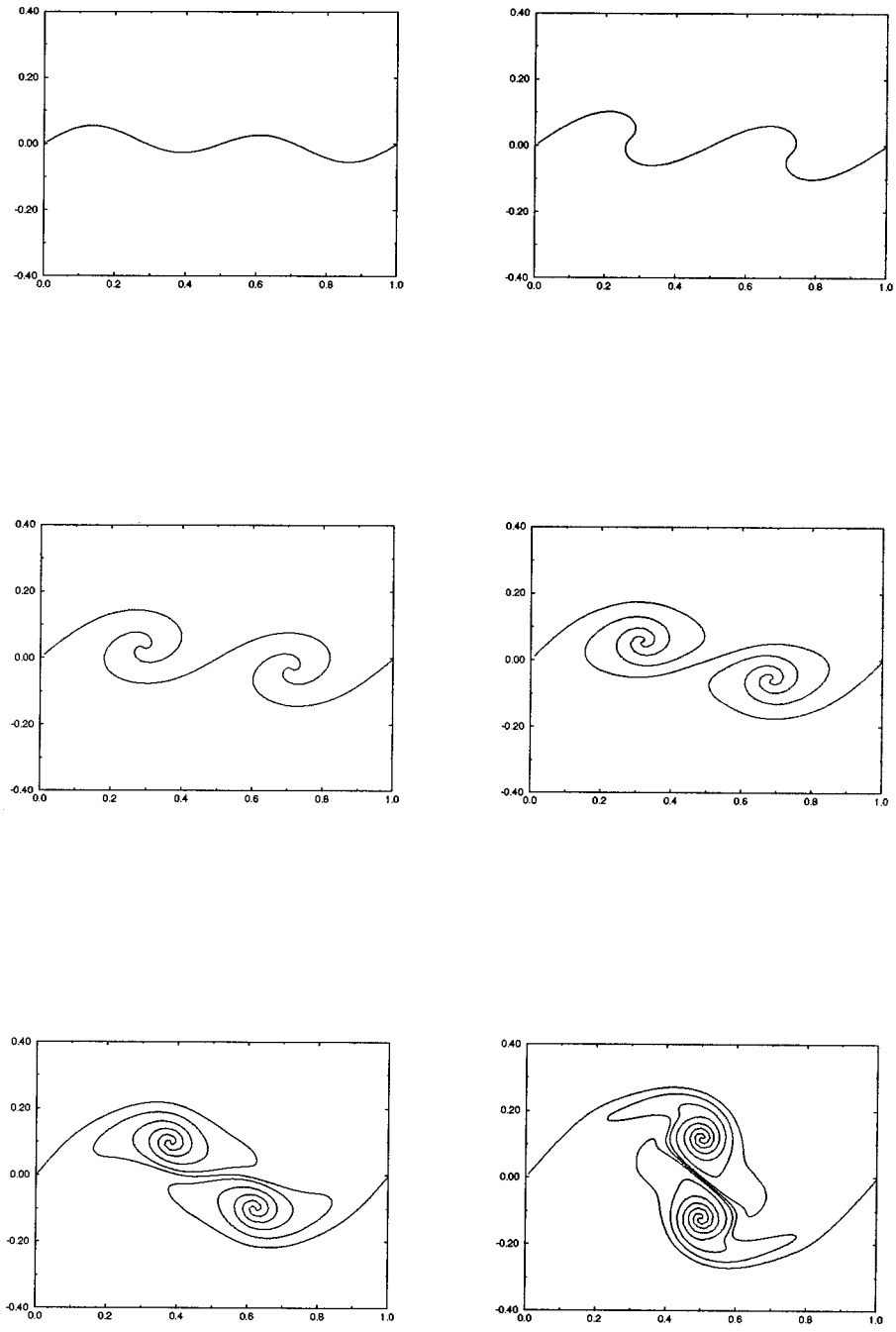

Figure 5.4: Periodic vortex sheet evolution at $t = 0,\ .4,\ .8,\ 1.2,\ 1.6$, and 2.0 (a),(b),(c),(d) left to right from top $\delta = .2,\ dt = .01,$ initial amplitudes $A_1 = .02, A_2 = .04$

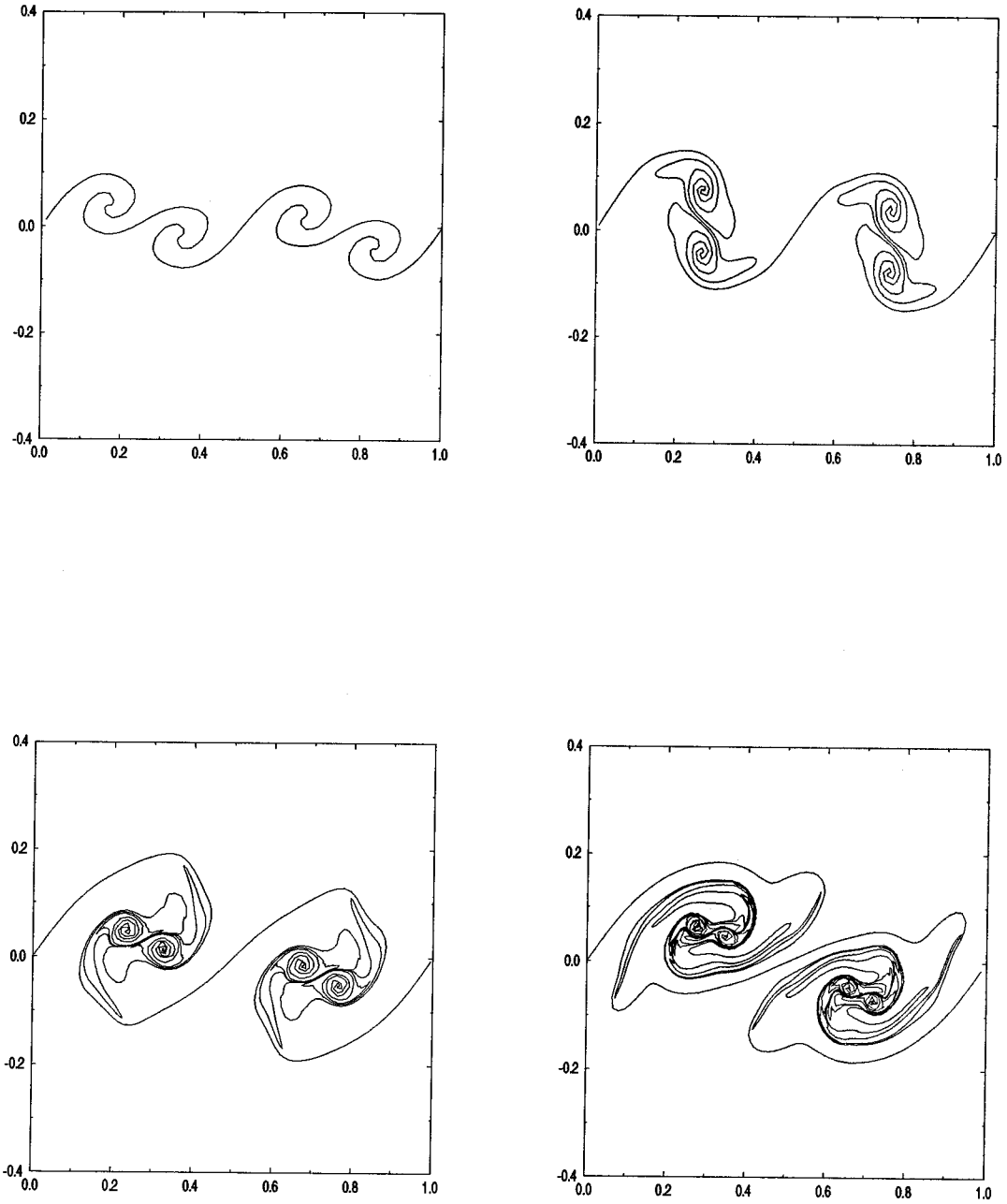

Figure 5.5: Periodic vortex sheet evolution at $t = .4, .8, 1.2, 1.6$ (a),(b),(c),(d),(e),(f) left to right from top $\delta = .1$, $dt = .01$, $A_1 = .01, A_2 = .02, A_3 = .03$

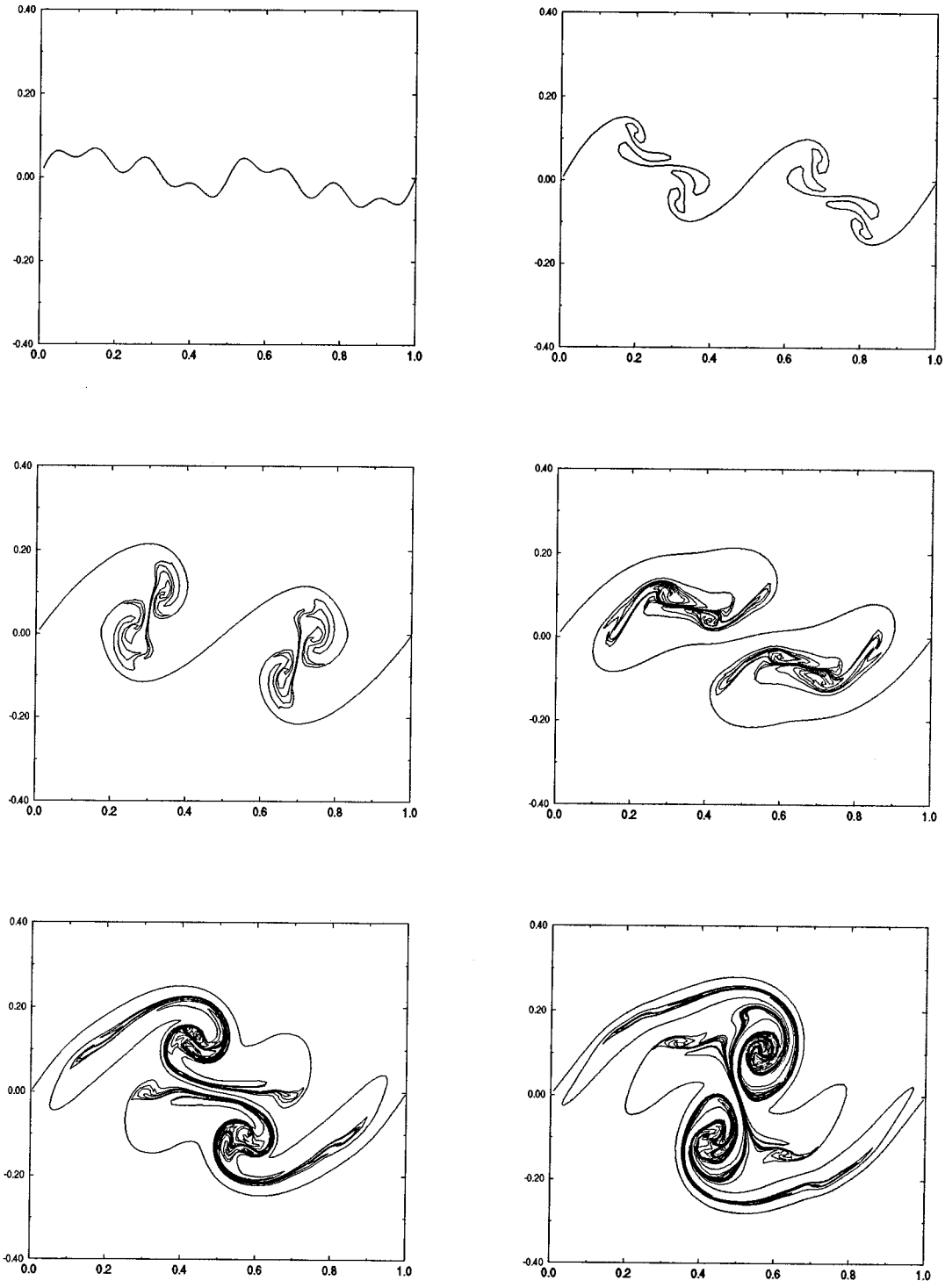

Figure 5.6: Periodic vortex sheet evolution at $t = 0,\ .4,\ .8,\ 1.2,\ 1.6$ and 1.96 (a),(b),(c),(d),(e),(f) left to right from top $\delta = .1,\ dt = .01,\ A_1 = .04, A_2 = .03, A_3 = .03, A_4 = .03$

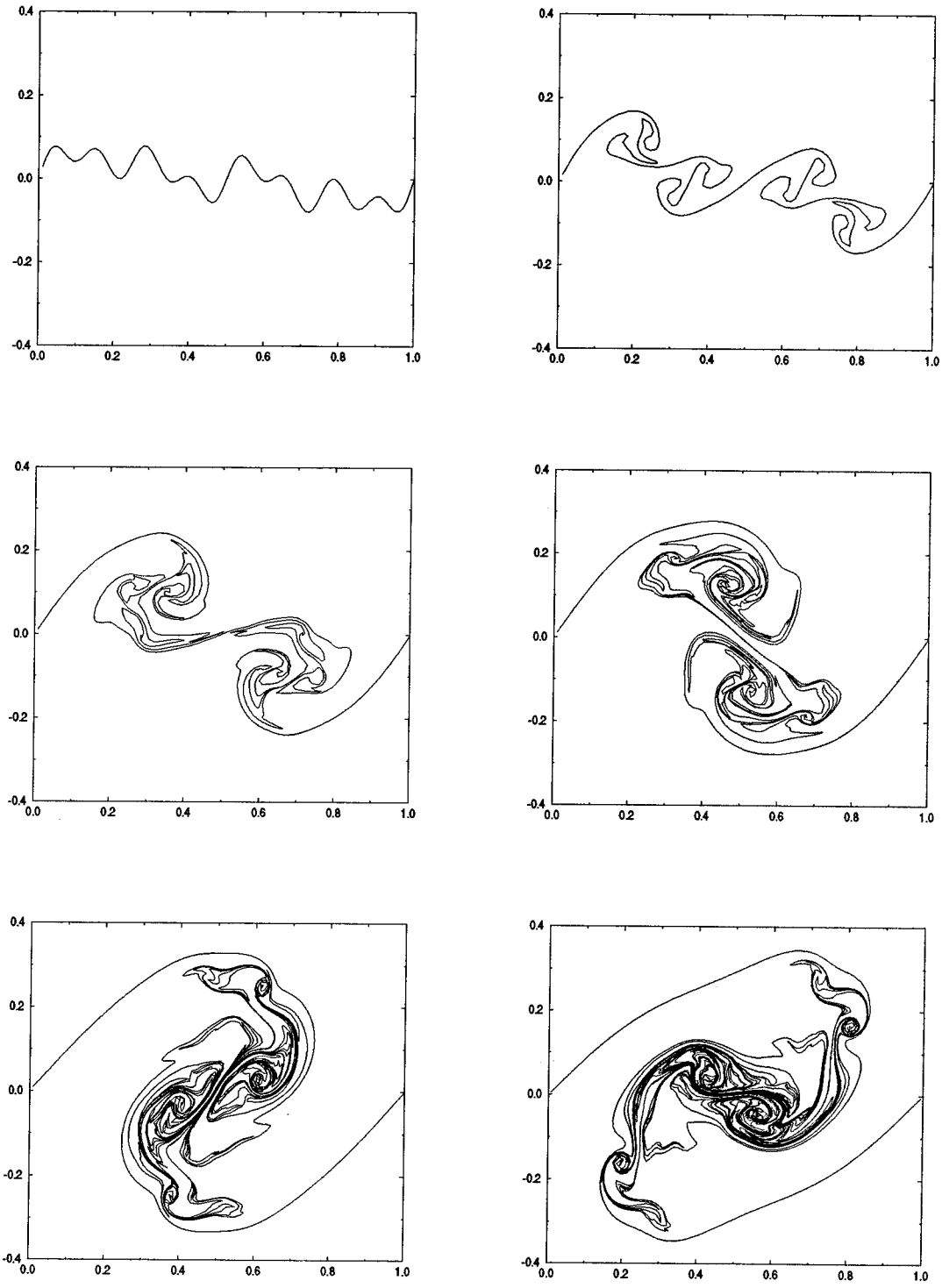

Figure 5.7: Periodic vortex sheet evolution at $t = 0, .5, 1.0, 1.5, 2.0$ and 2.43, (a),(b),(c),(d),(e),(f) left to right from top $\delta = .1$, $dt = .01$, $A_1 = .03, A_2 = .04, A_3 = .02, A_4 = .02$

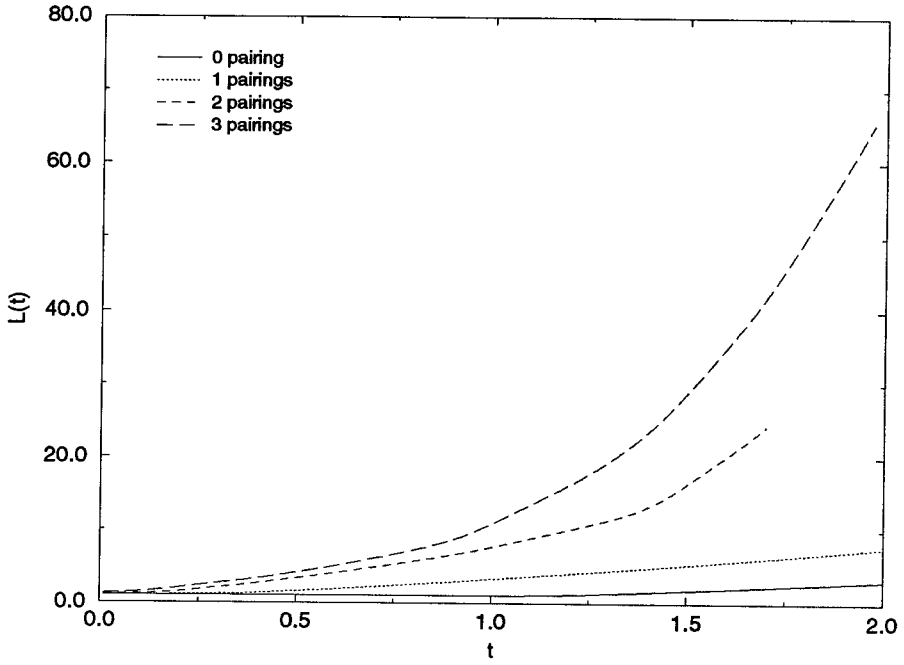

Figure 5.8: Comparison of line lengths for various runs

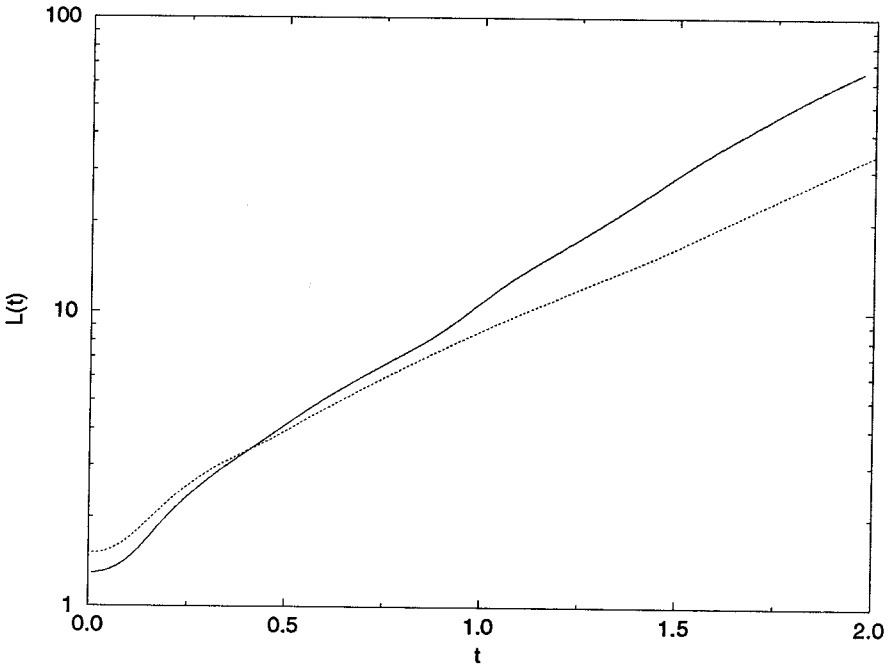

Figure 5.9: Comparison of line lengths for two runs with different initial subharmonic perturbations (three pairings)

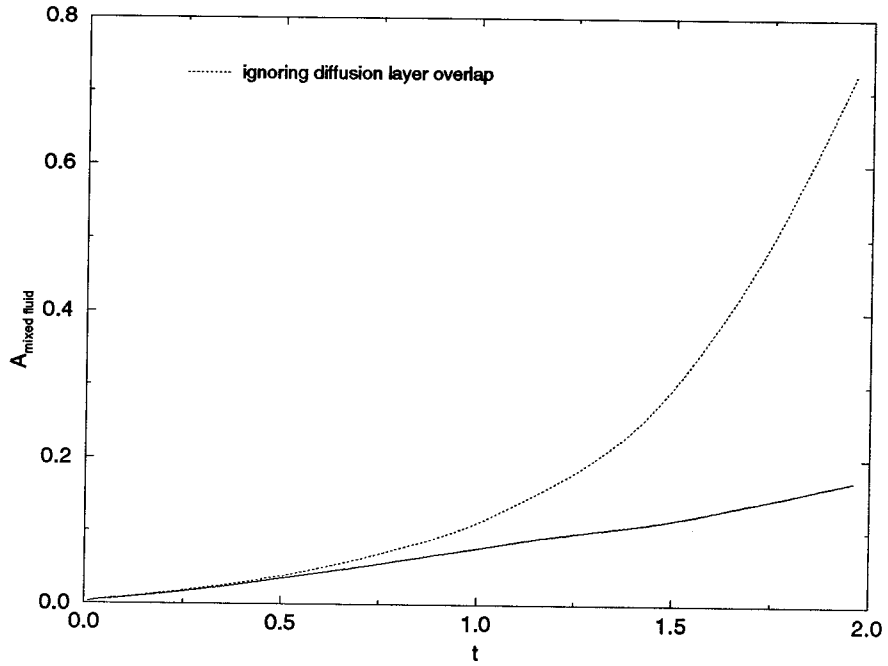

Figure 5.10: Mixed fluid area $A_m(t)$ for vortex sheet with three pairings

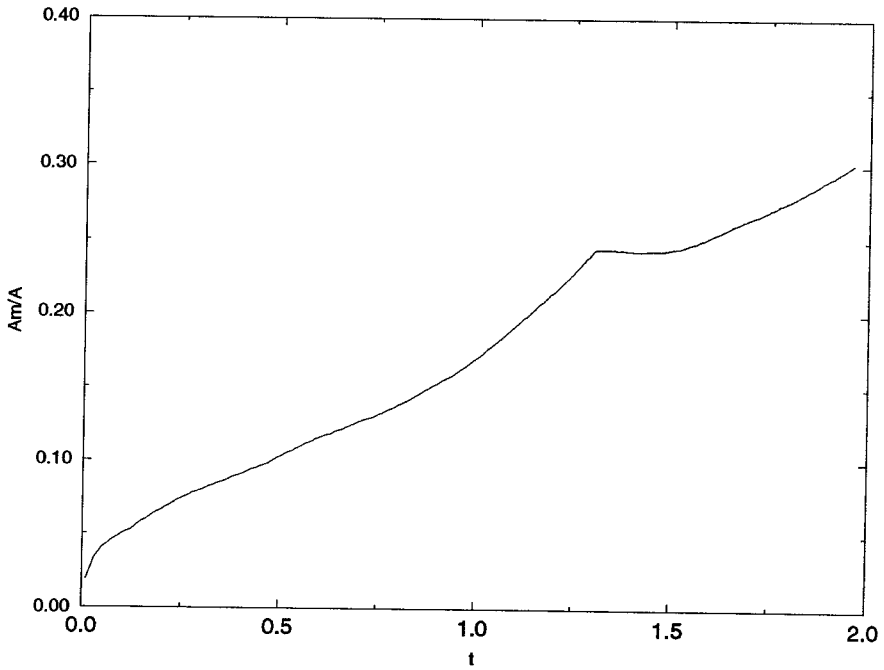

Figure 5.11: Mixed fluid fraction $\frac{A_m(t)}{A(t)}$ for vortex sheet with three pairings

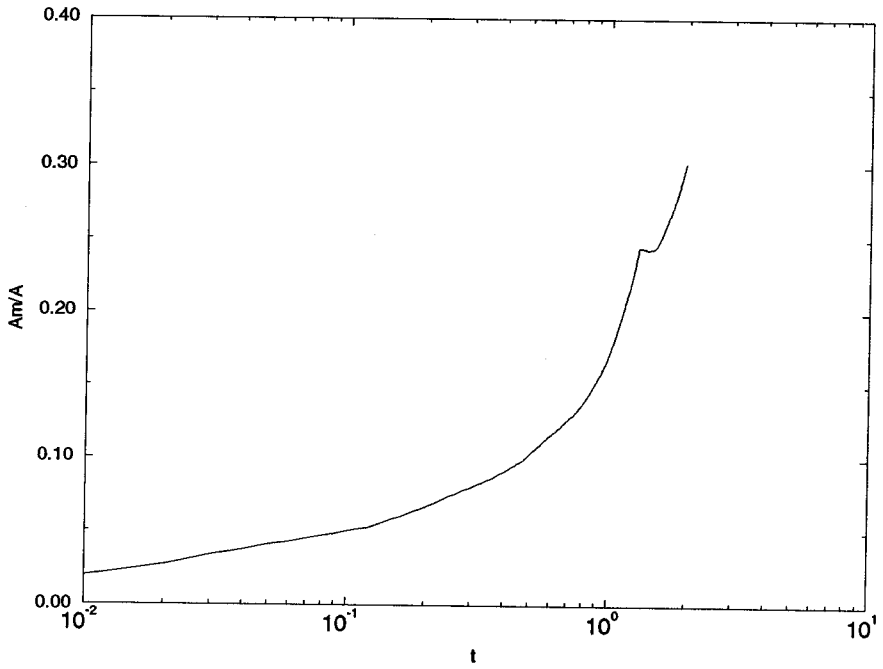

Figure 5.12: Mixed fluid fraction $\frac{A_m(t)}{A(t)}$ for vortex sheet with three pairings (log-linear plot)

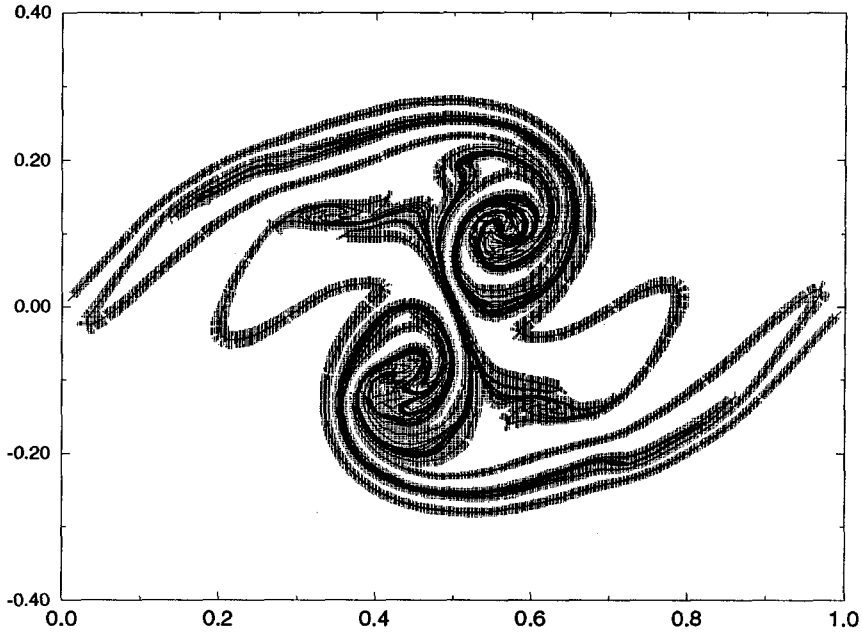

Figure 5.13: Diffusion (mixed) layer for three pairings

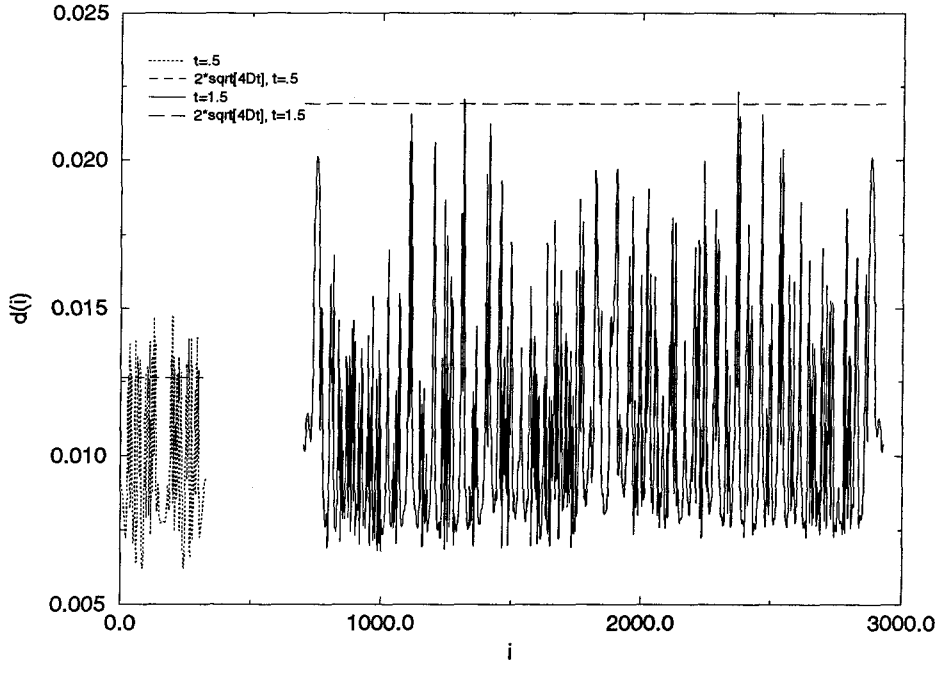

Figure 5.14: Distribution of diffusion layer thickness $d(i)$ for three pairings at $t = .5$ and $t = 1.5$

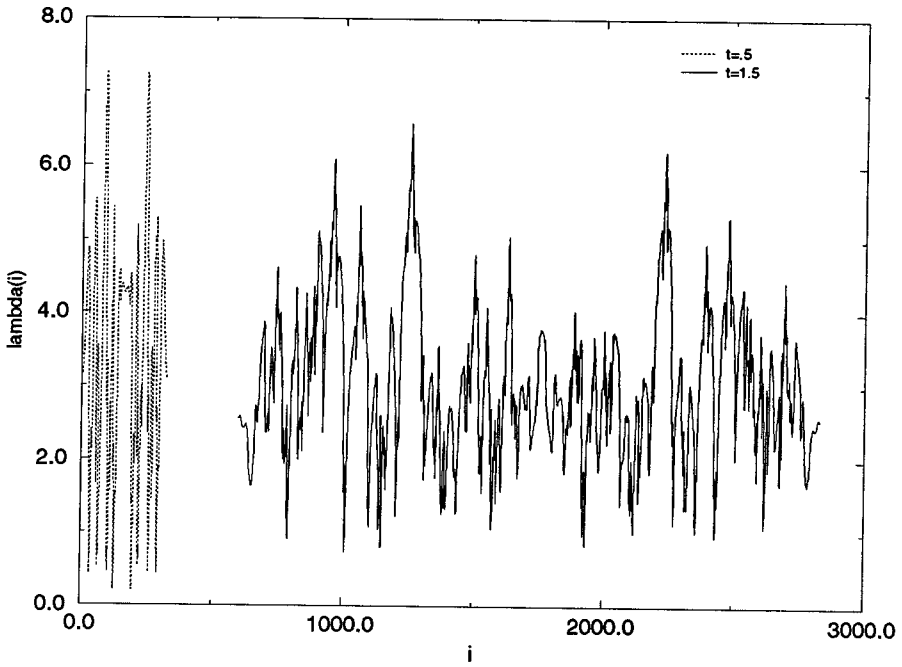

Figure 5.15: Distribution of stretch exponent $\lambda(i)$ for three pairings at $t = .5$ and $t = 1.5$

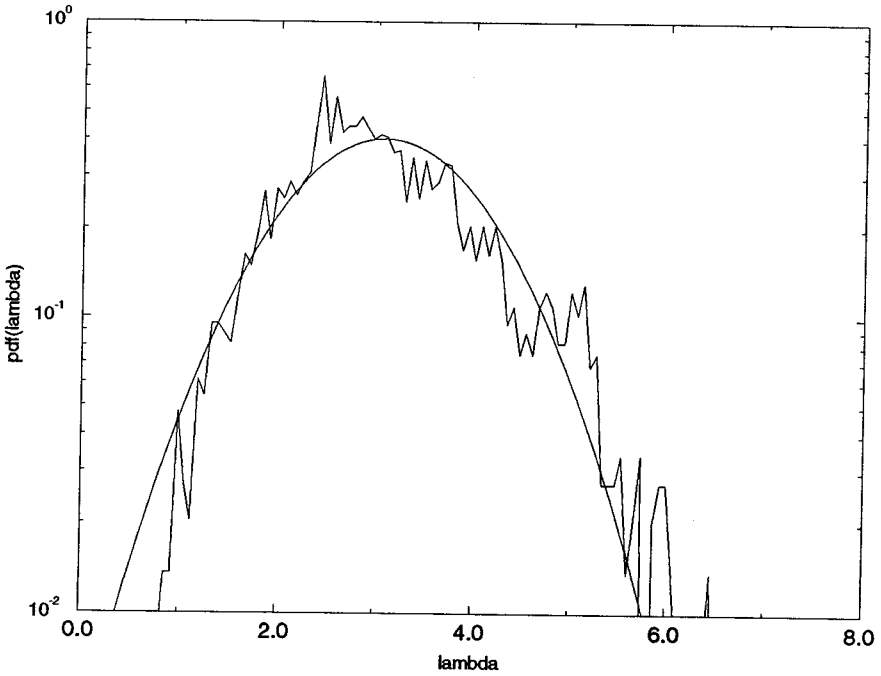

Figure 5.16: Stretch PDF $p(\lambda)$ vs λ for three pairings

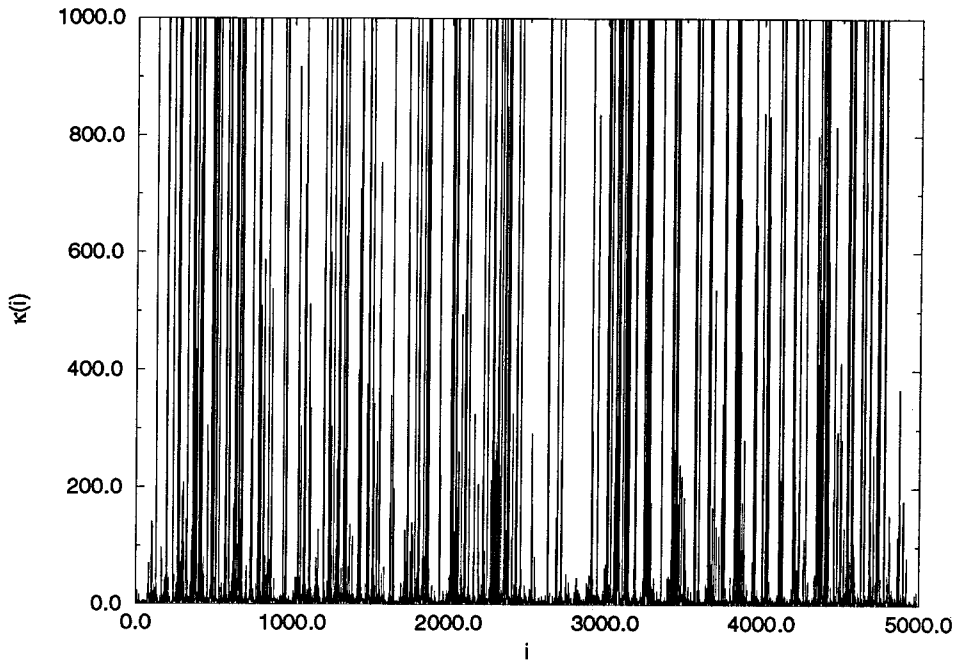

Figure 5.17: Curvature $\kappa(i)$ vs i for points along the vortex sheet with three pairings

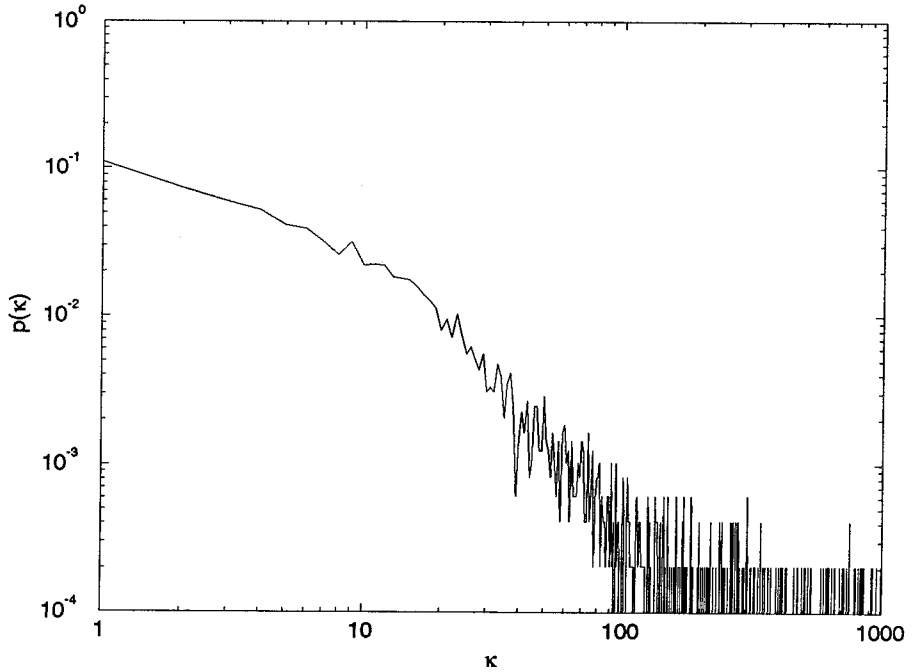

Figure 5.18: PDF $p(\kappa)$ of the curvature $\kappa(i)$ for points along the vortex sheet with three pairings

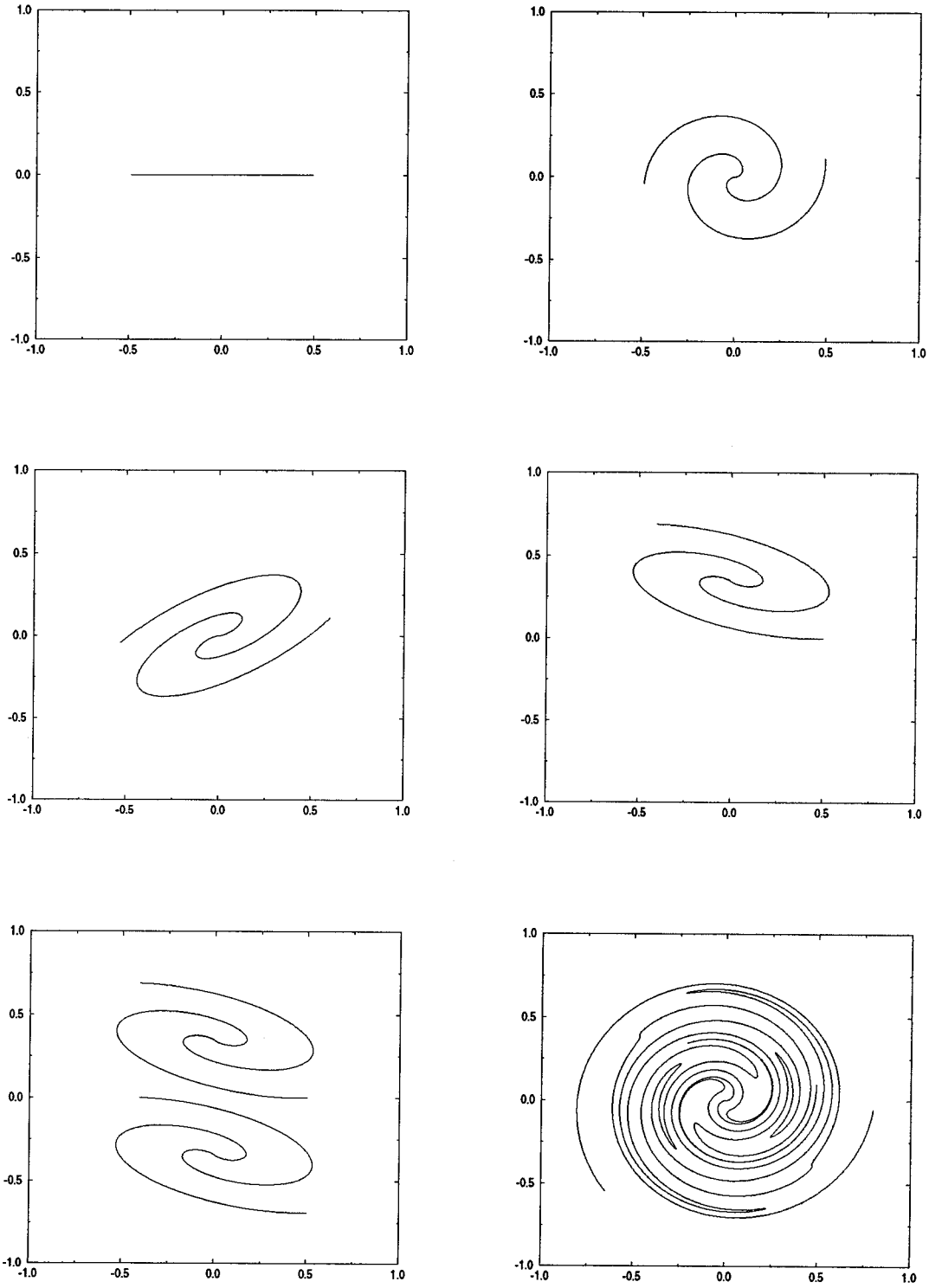

Figure 5.19: RM mapping evolution sequence (a),(b),(c),(d),(e),(f) left to right from top

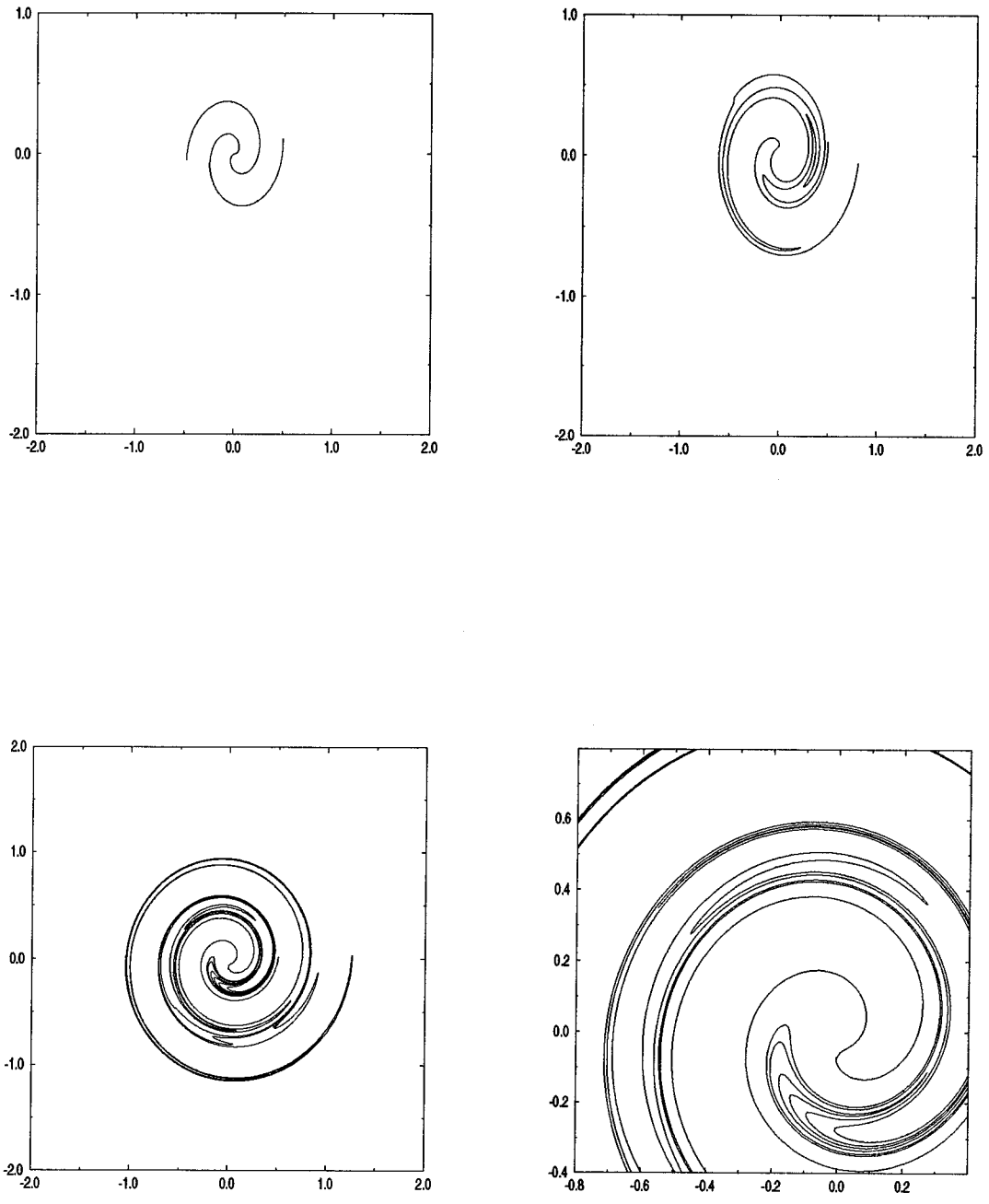

Figure 5.20: Line segment evolution due to RM mapping for $a = 15$, for $n = 1, 2, 3$ (a),(b),(c),(d) left to right from top, ((f) is a blow up of $n = 3$)

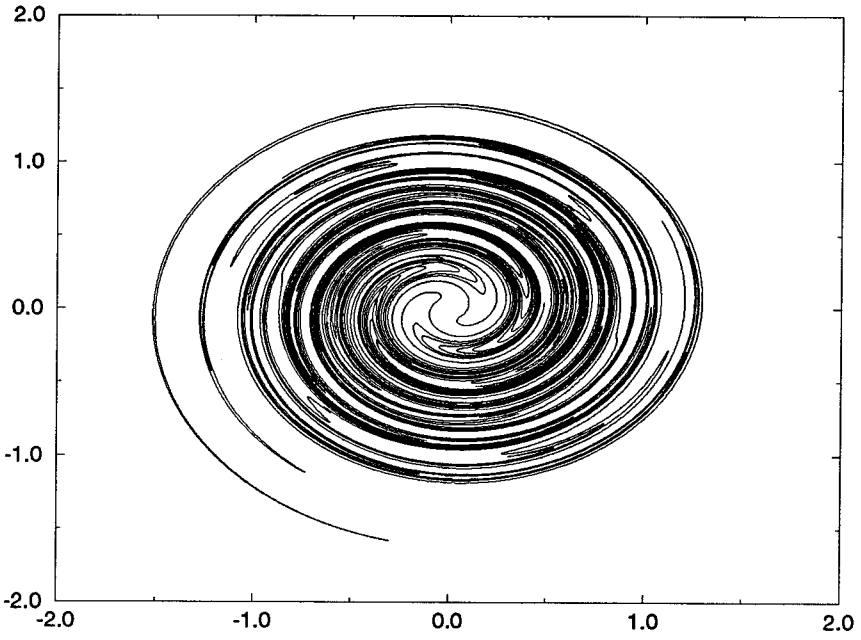

Figure 5.21: Line segment at $n = 3$ by RM mapping for $a = 13$ (includes duplication)

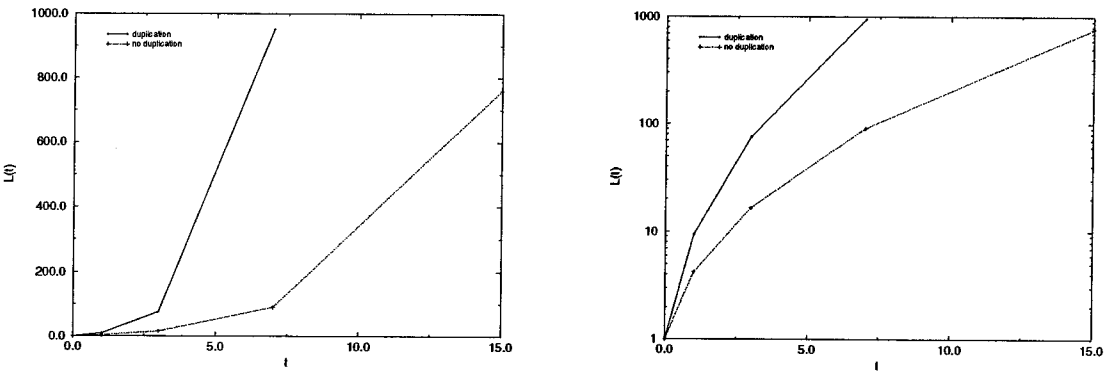

Figure 5.22: Line length evolution with t, with and with out duplication

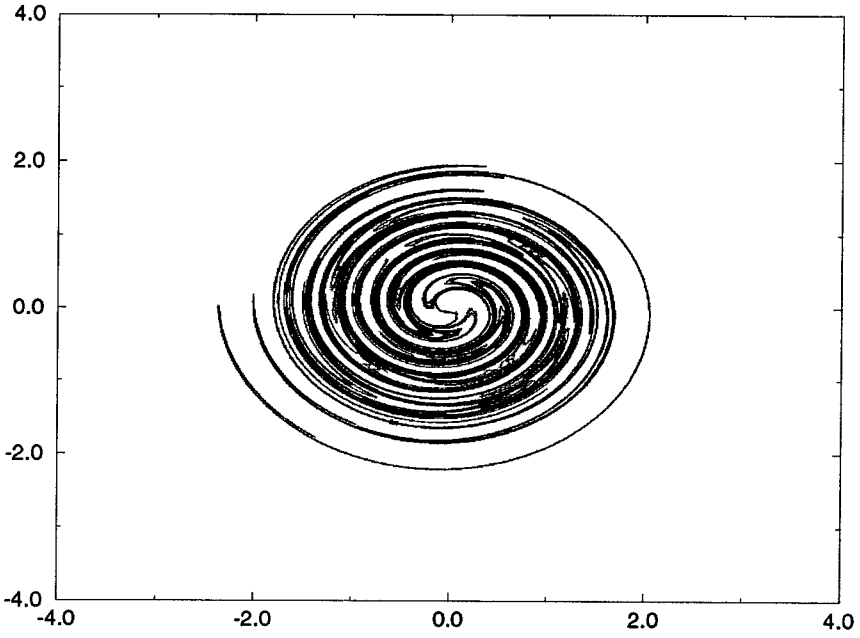

Figure 5.23: RM with diffusive layer, $D = 10^{-5}, a = -9,\ n = 4$

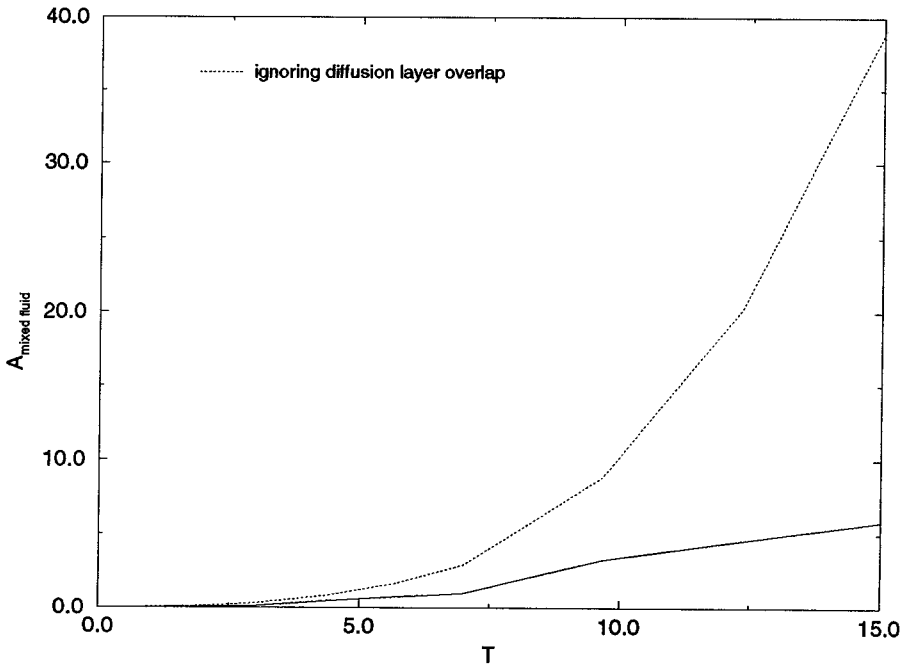

Figure 5.24: Mixed area for RM with diffusive layer, $D = 10^{-5}, a = -9,\ n = 4$

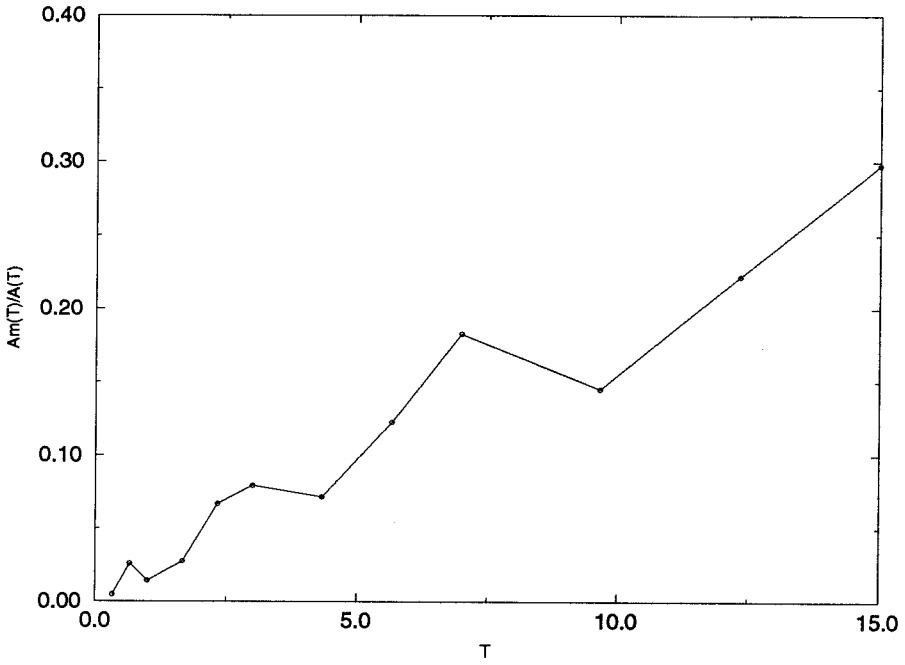

Figure 5.25: Mixed area fraction for RM with diffusive layer, $D = 10^{-5}, a = -9,\ n = 4$

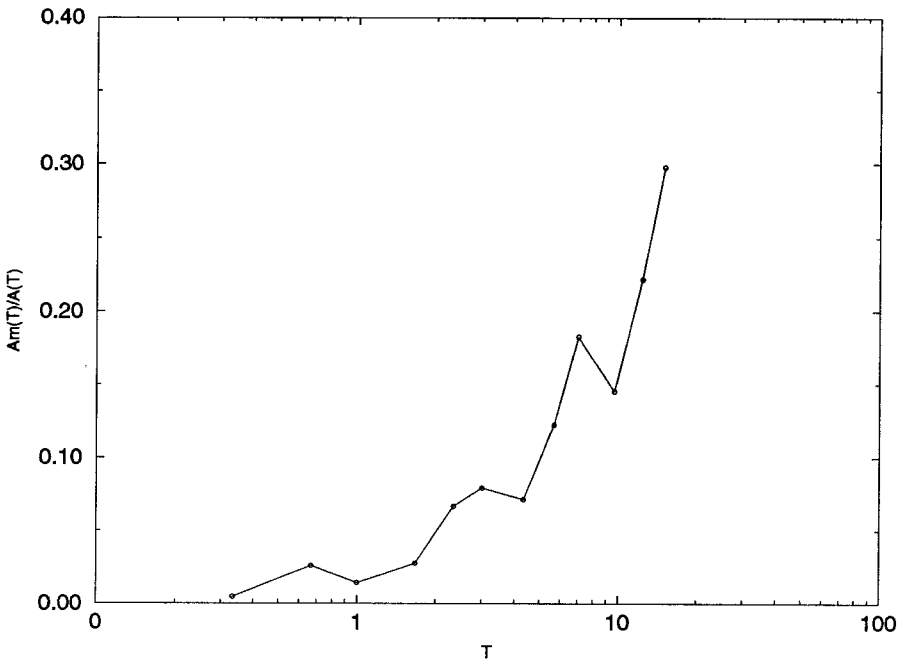

Figure 5.26: Mixed area fraction for RM with diffusive layer, $D = 10^{-5}, a = -9,\ n = 4$ (linear-log plot)

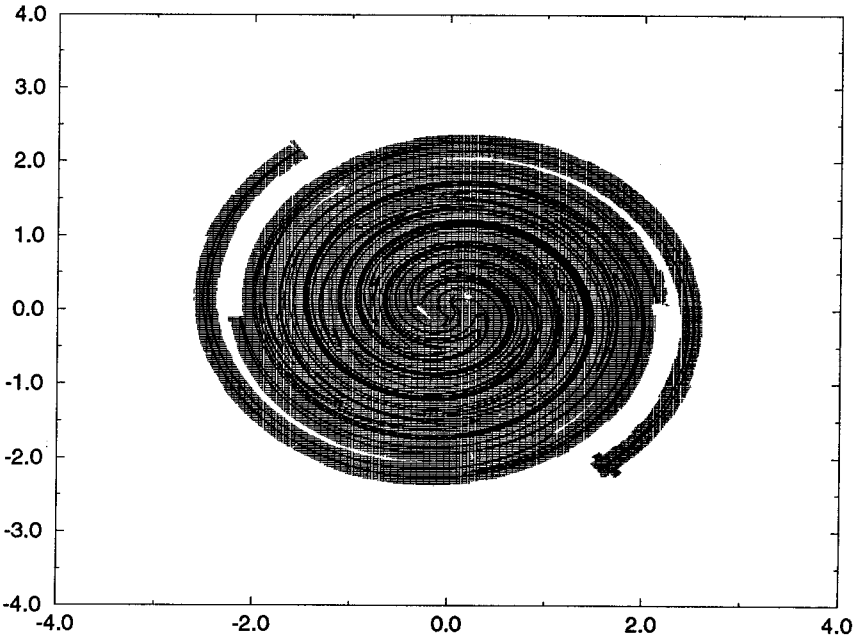

Figure 5.27: RM with diffusive layer, $D = 10^{-3}, a = -6,\ n = 4$

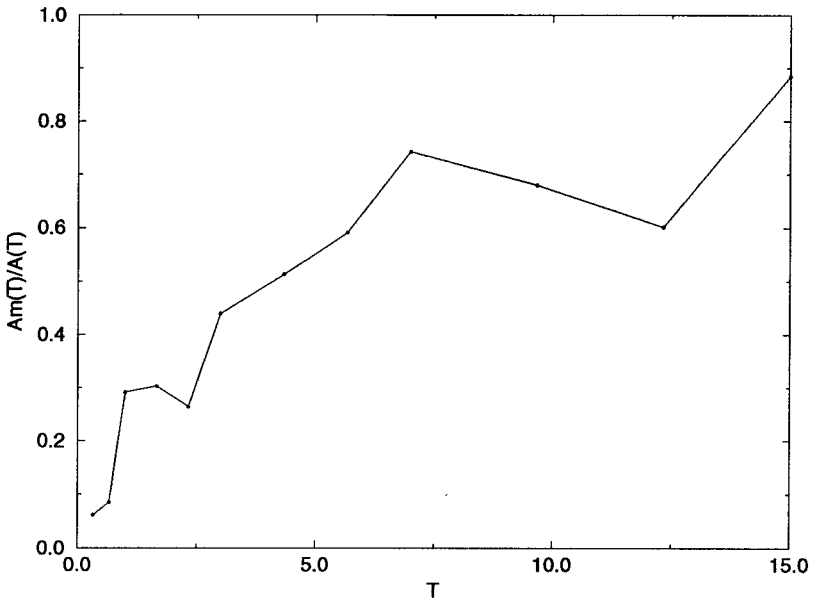

Figure 5.28: Mixed area fraction for RM with diffusive layer, $D = 10^{-3}, a = -6,\ n = 4$

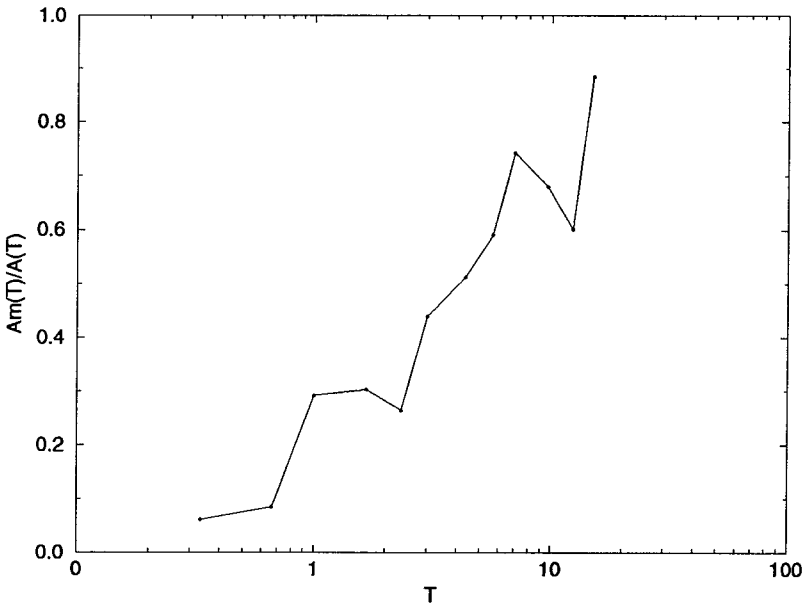

Figure 5.29: Mixed area fraction for RM with diffusive layer, $D = 10^{-3}, a = -6,\ n = 4$ (linear-log plot)

Chapter 6

Summary

6.1 Summary

The major points of this thesis can be summarized as follows:

In Chapter 2 we reported a simple consequence of the Biot-Savart law for the velocity induced by a vortex in N-vortex problems — that the probability density of velocity in the two-dimensional case has an inverse power law tail of the form u^{-3}. By decomposing the Eulerian velocity at a fixed point into a sum of N individual components whose contributions are supplied by the velocity induced by a single vortex, we made use of the limit distribution theorems to describe the velocity at the fixed point, based on the spatial distribution of vorticity. For the problem of N vortices of the same sign and strength we showed that in cases where the vortex core is non-singular, the probability distribution for the velocity is Gaussian. For the singular core case, the power-law tail distribution tends towards a Lévy stable distribution. The distribution of the velocity *difference* was found to tend towards non-Gaussian even for non-singular cores. The statistical implications of the physical shape and form of the vorticity was made clear by varying N and the de-

singularization parameter δ. Possible consequences for vortex methods simulations and insights into the character of large scale coherent structures were discussed. The Lagrangian velocity statistics were also predicted based on the Eulerian statistics and compared with numerical computations.

The problem of non-diffusive stirring of incompressible fluid by N like-signed, equal-strength vortices was considered. This flow is non-isotropic and non-homogeneous in contrast to many studies of line stretching in turbulence. We believe the vortex interaction feature also captures some of the key properties of real vortical fluid flow that is often absent from simple, near-integrable dynamical systems. The stretching of interfacial lines and the finite time Lyapunov (stretch) exponents of a set of points was computed in chapter 3. The probability density function (PDF) of the stretch exponents was found to range from Gaussian to strongly non-Gaussian depending on the parameter values. For the distribution of Lyapunov exponents over the whole domain, the central part of the PDF becomes Gaussian with time (due to central limit theorem type behavior), but we emphasize that for stretch statistics on the *interfacial line*, the non-Gaussian high stretch tails dominate the PDF distributions. The different types of stretching achieved for various values of the parameters N and δ were illustrated and explained in terms of the passive particle transport and a multinomial multiplicative process model.

The spatial distribution of a non-diffusive scalar $\xi(x)$ was computed in a Lagrangian calculation of an interface that has the scalar value $\xi = 1$ on one side and $\xi = 0$ on the other. This interface was advected by the flow produced by N vortices in two-dimensional space. The spectra of the spatial distribution of the scalar ξ was then measured for a one-dimensional cut. Several measurements were made, and they showed an approximately power-law $k^{-\gamma}$ form ($1 < \gamma < 2$). We examined the fluid dynamics that lead to the particular interface distribution and discussed some models that produce the power-law spectra. These models include random telegraph, fractal and activated random processes. We have also characterized the

geometry of the lines by evaluating the functions $N(r)$ and $H(r)$ using box counting techniques.

The mixing of passive fluid by pairing (merging) of vortex structures was then studied. The purpose was to specifically examine the role of the large scale two-dimensional motion in bringing about mixing in the pre-turbulent shear layer. The degree of mixedness brought on by this pre-turbulent motion was examined especially in the context of the idea of mixing transition that is observed in shear layers. One purpose of this analysis was to quantify the relative contributions from the effects of the large scale, two-dimensional mixing (chaotic advection) in contrast to the turbulent mixing caused by three-dimensionality and small scales. Two models were used: the periodic vortex sheet that undergoes up to three pairings and a new kinematical map that models the behavior of the space developing mixing layer. It was found from these that a mixing mechanism in the form of stretching and folding of the interfacial line exists for the two-dimensional motion, and this can advance rapidly due to the pairing, and can contribute significantly to the achievement of a mixed state. The fluid mixing is quantified by keeping track of the interfacial line stretch, the diffusion across this interface, as well as the overlap of the diffusion layers. Although this mixing mechanism is overtaken in the shear layer by the mixing caused by the small scale, three-dimensional vorticity (which are themselves created by this motion), it is suggested that good mixing can occur without the development of what is traditionally viewed as fully developed turbulence, and that perhaps *mixing* transition and *turbulence* transition are not necessarily coincident. We also highlighted the difference in the mechanism between turbulent mixing and what might be termed chaotic advection type mixing and how they compete with each other in this physical setting. The general applicability of this type of mixing mechanism present in two-dimensional vortical flows that are not fully turbulent was emphasized.

6.2 Future work

There are several avenues for follow-up work; for the most part it consists of extending the present models and simulations in three areas:

1. three-dimensional flows
2. viscosity and diffusivity effects on vorticity and scalars
3. allow different scales of vorticity

More specific work can be listed as follows (in no particular order):

For the velocity statistics work, we plan to follow-up with the study of structure functions for various local distributions of vorticity in three-dimensions.

Perform analysis of spectra on problems that include diffusion as we have dealt with non-diffusive interfaces in chapter 4 (although we have included diffusion in the mixing studies of chapter 5).

In two-dimensional flows, the next level of complexity is to allow different signs for the vortices. The major problem brought on by this is that the boundary conditions will have to changed to ensure a statistically stationary situation. A doubly periodic boundary condition could be acceptable, but unlike the single periodic boundary case, we know of no derivation that formulates the problem in a calculable way.

Explore stretching and spatial distribution of passive lines and surfaces by three-dimensional vortices. Apart from the increased computational requirements, an issue is establishing a stationary configuration.

Although we have briefly touched on the Lagrangian transport properties in the N-vortex flow, other studies are currently underway, that have not been reported in this thesis, such as the difference between the transport properties of passive particles

versus discrete vortices, the dispersion properties for various vortex distributions, etc.

Bibliography

[1] T.M. Antonsen,Jr. and E. Ott, Phys. Rev. A **44**(2), 851-857, (1991).

[2] Aref, Ann. Rev. Fluid Mech. **15**, 345-389, (1983).

[3] H. Aref, J. Fluid Mech. **143**, 1-21, (1984).

[4] H. Aref, Theor. and Appl. Mech. F.I. Niordson and N. Olhoff (ed.) Elsevier Science pub. B.V. (North-Holland), IUTAM, (1985).

[5] H. Aref, J.B. Kadtke, I. Zawaadzki, Physica D**37**, 423-440, (1989).

[6] H. Aref, Phil. Trans. R. Soc. Lond. A **333**, 273-288, (1990).

[7] H. Aref, Phys. Fluids A**3**(5), 1009-1016, (1991).

[8] W.T. Ashurst and E. Meiberg, J. Fluid Mech. **189**, 87-116, (1988).

[9] A. Babiano, C. Basdevant, B. Legras, R. Sadourny, J. Fluid Mech. **183**, 379-397, (1987).

[10] A. Babiano, G. Boffetta, A. Provenzale, A. Vulpiani, Phys. Fluids **6**(7) 2465, (1994).

[11] G.K. Batchelor, Proc. Roy. Soc. (London) A**213**, 349-366, (1952).

[12] D. Beigie, Ph.D. thesis, California Institute of Technology, (1992).

[13] D. Beigie, A. Leonard and S. Wiggins, Phys. Fluids A**3**(5),1039 (1991).

[14] D. Beigie, A. Leonard, S. Wiggins, Physical Review Lett. **70**, 275-278, (1993).

[15] D. Beigie, A. Leonard, S. Wiggins, Chaos, Solitons and Fractals **4**(6), 749-868, (1994).

[16] R. Benzi, S. Patarnello, and P. Satangelo, J. Phys. A: Math. Gen. **21**, 1221-1237, (1988).

[17] M.V. Berry, J.L. Balazc, M. Tabor, A. Voros, Ann. Phys. **122**, 26-66, (1979).

[18] M.E. Brachet, M. Meneguzzi, and P.L. Sulem, Phys. Rev. Lett. **57**(6), 683-686, (1986).

[19] J.E. Broadwell and M.G. Mungal, Phys. Fluids A**3**(5), 1193-1206, (1991).

[20] G. Brown and A. Roshko, J. Fluid Mech. **78** 535-560, (1976).

[21] H. Catrakis, Personal Communications, (1994).

[22] S. Chandrasekhar, Rev. of Modern Physics, **15**(1) 1-87, (1943).

[23] W.J. Cocke, Phys. Fluids **12**(12), 2488-2492, (1969).

[24] W.J. Cocke, Phys. Fluids **14**(8), 1624-1628, (1971).

[25] P. Comte, M. Lesieur and E. Lamballais, Phys. Fluids A**4**(12), 2761-2778 (1992).

[26] A. Crisanti, M Falcioni, G. Paladin and A. Vulpiani, Physica A**166**, 305-324, (1990).

[27] G.M. Corcos and F.S. Sherman, J. Fluid Mech. **139** 29-65, (1984).

[28] G.M. Corcos and S.J. Lin, J. Fluid Mech. **139**, 67-95, (1984).

[29] W.J.A. Dahm, K.B. Southerland, K.A. Buch, Phys. Fluids A**3**(5), 1115-1127, (1991).

[30] P.E. Dimotakis, in *High-Speed Flight Propulsion Systems*, S.N.B. Murthy and E.T. Curran (eds.), Vol 137 of Progress in Astronautics and Aeronautics, AIAA, pages 265-340, (1991).

[31] P.E. Dimotakis, in *Lecture Notes in Engineering***40** R. Borghi and S.N.B. Murthy (eds.), 417-485, Springer-Verlag, (1989).

[32] P.E. Dimotakis, R.C. Miake-Lye, D.A. Papantoniou, Phys. Fluids **26**, 3185-3192, (1983).

[33] P.E. Dimotakis and P. L. Miller, Phys. Fluids A**2**(11), 1919-1920, (1990).

[34] P.E. Dimotakis, Nonlinear Science Today, **1** (2),1, (1991).

[35] P.E. Dimotakis, personal communications.

[36] P.E. Dimotakis, 'Some issues on turbulent mixing and turbulence', GALCIT report FM93-1, (1993).

[37] E. Dresselhaus and M. Tabor, J. Fluid Mech. **236**, 415-444, (1991).

[38] P. Dutta and P. M. Horn, Rev. of Modern Physics **53**(3), 497-516, (1981).

[39] J.D. Farmer, E. Ott, J.A. Yorke, Physica D**7**, 153-180, (1983).

[40] J. Feder, *Fractals*, Plenum Press, (1988).

[41] W. Feller, *An Introduction to Probability Theory and its Applications*, vol II, John Wiley and Sons, (1971).

[42] Franjione and J. Ottino, Phys.Fluids **30**, 3641-3643, (1987).

[43] J. Fung and J. Vassilicos, Phys. Fluids A**3**(11),2725 (1991).

[44] A. D. Gilbert, J. Fluid Mech. **193**, 475-497, (1988).

[45] C.-M. Ho and P. Huerre, Ann. Rev. Fluid Mech. **16**, 365-424, (1984).

[46] M. Holzer and E.D. Siggia, Phys. Fluids **6**(5), 1820-1837, (1994).

[47] L.-S. Huang and C.-M. Ho, J. Fluid Mech. **210**, 475 (1990).

[48] J.P. Gollub, J. Clark, M. Gharib, B. Lane, and O.N. Mesquita, Phys. Rev. Lett. **67**(25), 3507-3510, (1991).

[49] P. Grassberger, Phys. Lett. **97 A**, 227, (1983).

[50] P. Grassberger and I. Procaccia, Phys. Rev. Lett. **50**(5), 346-349, (1983).

[51] H.G.E. Hentshel and I. Procaccia, Physica D **8**, 435-444, (1983).

[52] P. Jacobs and D. Pullin, J. Fluid Mech. **199** 89 (1989).

[53] J. Jiménez and C. Martel, Phys. Fluids A**3**(5), 1261 (1991).

[54] K. Kaneko, Physica D**55**, 368-384, (1992).

[55] T.J. Kaper and S. Wiggins, J. Fluid Mech. **253**, 211-243, (1993).

[56] A.R. Karagozian and F.E. Marble, Combust. Sci. Tech. **45** 65-84, (1984).

[57] A.R. Kerstein, Combust. Sci. Tech. **60**, 391, (1988).

[58] A.R. Kerstein, Combustion and Flame **75**, 397-413, (1989).

[59] A.R. Kerstein, Phys. Fluids A**3**(5), 1110-1114, (1991).

[60] M.M. Koochesfahani, Ph.D. thesis, California Institute of Technology (1985).

[61] M.M. Koochesfahani and P.E. Dimotakis, J. Fluid Mech. **170**, 83, (1986).

[62] J. Konrad, Ph.D. thesis, California Institute of Technology (1977).

[63] P. Koumoutsakos, Ph.D. thesis, California Institute of Technology, (1993).

[64] R. Kraichnan, Phys. Fluids **10**(7), 1417-1423, (1967).

[65] R. Kraichnan and D. Montgomery, Rep. Prog. Phys. **43**, 547-619, (1980)..

[66] R. Krasny, J. Comp. Phys. **65**(2), 292 (1986).

[67] J. C. Lasheras and H. Choi, J. Fluid Mech. **189**, 53-86, (1988).

[68] A. Leonard, J. Comput. Physics **37**(3) 289, (1980).

[69] A. Leonard, Annual Rev. Fluid Mech. **17**, 523-559, (1985).

[70] A. Leonard, K. Chua, Physica D**37**, 490-496, (1989).

[71] A. Leonard, V. Rom-Kedar, and S. Wiggins, Nucl. Phys. B (Proc. Suppl.) **2**, 179 (1987).

[72] M. Lesieur, C. Staquet, P. Le Roy and P. Comte, J. Fluid Mech **192**, 511-534 (1988).

[73] M. Lesieur, *Turbulence in Fluids*, Martinus Nijhoff Pub., (1987).

[74] A.J. Lichtenberg and M.A. Lieberman, *Regular and chaotic dynamics, 2nd ed.*, Springer-Verlag, (1992).

[75] T.S. Lundgren and Y.B. Pointin, J. Stat. Physics, **17**(5) 323-355, (1977).

[76] B.B. Mandelbrot, *The Fractal Geometry of Nature*, W. H. Freeman, (1983).

[77] F.E. Marble, Recent Advances in Aerospace Sciences, 395, (1985).

[78] J.C. McWilliams, J. Fluid Mech. **146**, 21-43, (1984).

[79] M.V. Melander, J.C. McWilliams, and N.J. Zabusky, J. Fluid Mech. **178**, 137-159, (1987).

[80] P. Miller and P.E. Dimotakis, Phys. Fluids A**3**(1), 168-177,(1991).

[81] P. Miller and P.E. Dimotakis, GALCIT Report FM92-3, (1992).

[82] D. Montgomery and G. Joyce, Phys. Fluids **17**, 1139, (1974).

[83] E.W. Montroll and M. F. Shlesinger, J. Stat. Physics **32** (2), 209-230, (1983).

[84] R. Moser and M. Rogers, Phys. Fluids A**3**(5), 1128 (1991).

[85] R. Moser and M. Rogers, J. Fluid Mech. **247**, 275-320 (1993).

[86] F.J. Muzzio, P.D. Swanson, and J.M. Ottino, Physics of Fluids A**3**(5) 822-834, (1991).

[87] E.A. Novikov and Yu. B. Sedov, Sov. Phys. JETP **48**(3), (1978).

[88] K.J. Nygaard and A. Glezer, J. Fluid Mech. **231**, 257-301, (1991).

[89] S.A. Orszag, Phys. Fluids, **13**, 2203-2204, (1970).

[90] E.O. Ott and T.M. Antonsen, Jr., Phys. Rev. A**39**(7), 3660-3671, (1989).

[91] J.M. Ottino J. Fluid Mech. **114**, 83-103, (1982).

[92] J.M. Ottino, *The kinematics of mixing: stretching, chaos, and transport*, Cambridge University Press, (1989).

[93] J.M. Ottino, Annual Rev. Fluid Mech. **22**, 207-254, (1991).

[94] A. Papoulis, Probability, Random Variables, and Stochastic Processes, McGraw-Hill, (1965).

[95] R.T. Pierrehumbert, Physics of Fluids A**3**(5) 1250-1260, (1991).

[96] R. T. Pierrehumbert, Nonlinear Phenomena in Atmospheric and Oceanic Sciences, Ed. G.F. Carnevale and R. T. Pierrehumbert, 27-46, (1992).

[97] R.T. Pierrehumbert and H. Yang, J. Atmos. Sci. **50**(15), 2462-2480, (1993).

[98] D.I. Pullin and P.G. Saffman, Proc. R. Soc. Lond. A**432**, 481-494, (1991).

[99] A. Pumir, B. Shraiman, E.D. Siggia, Phys. Rev. Lett. **66**(23), 2984-2987, (1991).

[100] S.O. Rice, in *Selected papers on Noise and Stochastic Processes*, N. Wax (ed.), Dover, (1954).

[101] J.J. Riley, R.W. Metcalf, and S.A. Orszag, Phys. Fluids **29**(2), 406-422, (1986).

[102] V. Rom-Kedar, A. Leonard, and S. Wiggins, J. of Fluid Mech. **214**, 347-394 (1990).

[103] A. Roshko, in *The Global Geometry of Turbulence*, J. Jiménez (ed.), (1991).

[104] P.G. Saffman, Stud. App. Math. **50** 377-383, (1971).

[105] R.A. Smith, Phys. Rev. A **43** (2), 1126, (1991).

[106] K.R. Sreenivasan, Ann. Rev. Fluid Mech. **23**, 539-600, (1991).

[107] M. Tabor, in *Topological Aspects of the Dynamics of Fluids and Plasmas*, H.K. Moffatt et al. (eds.) 83-110, (1992).

[108] H. Takayasu, Prog. Theor. Phys. **72** (3), 471-479 (1984).

[109] Tennekes and Lumley, *A first course in turbulence*, MIT press (1972).

[110] G. Tryggvason, W. Dahm and K. Sbeih, J. Fluids Engr. **113**, 31 (1991).

[111] F. Varosi, T.M. Antonsen, Jr., and E. Ott, Physics of Fluids A **3**(5) 1017-1028, 1991.

[112] J. C. Vassilicos and J. C. R. Hunt, Proc. R. Soc. Lond. A **435**, 505-534, (1991).

[113] A. Vincent and M. Meneguzzi, J. Fluid Mech. **225**, 1-20, (1991).

[114] A. Vulpiani, Physica D**38**, 372-376, (1989).

[115] S. Wiggins, *Introduction to Applied Nonlinear Dynamical Systems and Chaos*, Springer-Verlag, (1990).

[116] S. Wiggins, *Chaotic Transport in Dynamical Systems*, Springer-Verlag, (1992).

[117] C.D. Winant and F.K. Browand, J. Fluid Mech **63** 237-255, (1974).